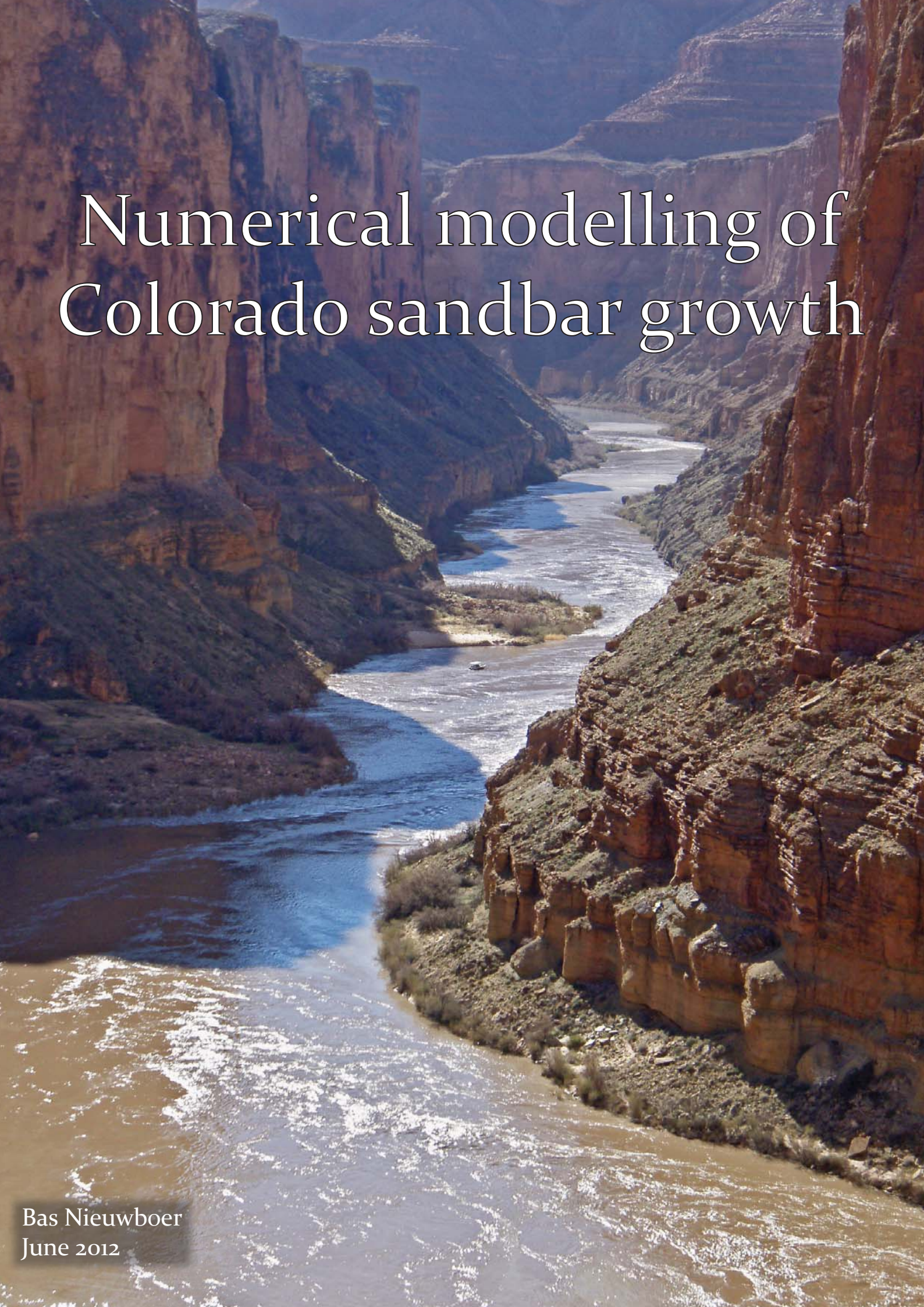

Numerical modelling of Colorado sandbar growth

Bas Nieuwboer
June 2012

Cover photo: Kees Sloff
View of the Eminence pool in the front followed by the Willy Taylor pool

Numerical modelling of Colorado sandbar growth

An improved formulation of sediment transport and underwater slope slumping.

Master Thesis of the study Civil Engineering at Delft University of technology

Bas Nieuwboer
Delft, June 2012
Student number: 1258877

Graduation committee:

Prof.dr.ir.	W.S.J. Uijttewaal
Dr.ir.	C.J. Sloff
Dr.ir.	E. Mosselman
Ir.	D.R. Mastbergen

Acknowledgements

First of all I would like to thank the members of my graduation committee for guiding me through the graduation process. Especially, Kees Sloff, my direct supervisor has helped me a lot to understand the problems in the previous models.

Also, I would like to thank the company Deltares for facilitating the office for me to work on my Master thesis. At Deltares I have had the possibility for asking assistance in solving the problems I faced during my master graduation. I would like to thank all the colleagues that provided help, still two of them in particular. Bert Jagers and Adri Mourits have guided me through the complex source-code of Delft3D. Bert was always able to help me find the right variables in the source-code. Adri has assisted me, when the code could not be compiled or Delft3D produced an error when I was executing the model.

Bram van Prooijen of the TU Delft has helped me a lot. He took interest in my study and showed me the right direction, when I was lost in the physics.

Off course my parents Jan en Tineke supported me by taking an interest in the subject as well as the process of graduation.

Last of all, I would like to thank my friends and student colleagues. With the latter I've had nice brainstorms about our theses, and also nice dinners and drinks.

Abstract

In the Colorado River the Glen Canyon dam is located. The Glen Canyon dam is constructed in the Colorado river for the production of electricity. Due to the dam, nowadays only a fifth of the pre-dam sediment volume flows into the Colorado River through the Glen Canyon dam and the two major tributaries, the Paria River and the Little Colorado River. Due to the lack of sediment the sandbars present in the Colorado River started eroding.

An attempt to solve this problem was by mimicking the pre-dam seasonal variation in discharge. High flood experiments (HFE) were conducted in 1996, 2004 and 2008. These HFE's were partly successful; some sandbars grew, while other eroded during the HFE. A Delft3D model of two pools and sandbars was created for a better understanding of deposition of sediment on the sand bar. The resulting modelled topography showed 5 major differences with the measured bed levels. The banks in the model were higher than in reality. The main stream width became smaller as opposed to reality. The sandbar height was over-predicted and the sandbars were growing too much into the pool. The last difference is that the model did not show an erosion hole in the main stream as was visible in the measurements.
To improve the shortcomings of the model two adjustments are implemented in the model. Turbulent velocities appear to be important because surface boils were seen during the HFE. In this thesis a sediment transport formula is created, which includes the turbulent velocity fluctuations on the sediment entrainment. The second adjustment is an avalanching and slumping formulation to overcome the shortcoming related to the narrowing of the main stream and to include the slope slumps as seen at the site.

These near-bed velocities are described using a probability density function, which includes the turbulent velocity fluctuations. The near-bed concentrations are calculated using the probability of occurrence of an instantaneous velocity. This probability is multiplied with the concentration corresponding to that velocity. For every instantaneous velocity in the probability density function a concentration contribution is calculated. The sum of these contributions describes the concentration including the turbulent fluctuations.
The avalanching is included by stating that no deposition can take place on slopes steeper than the angle of repose (32 degrees). Two methods are described: one where the sediment that cannot be deposited is re-suspended and one where it is transported as bed load. A third method simulates a large slope slump at a location where the bed slope was larger than the angle of repose. The slope is then changed to an equilibrium slope of 25 degrees. The sediment is transported as bed-load to the lower lying computational cells.

With the inclusion of the two new formulations in the model that is applied to the Eminence pool, both formulations show to have an effect on the computed topography. When the near-bed turbulent velocities are included in the sediment transport the sandbar extends more into the pool, where the measurements show a shorter sandbar. The slope slumping method severely changed the computed topography; the Delft3D model became unstable. Both avalanching formulations showed a same influence on the final computed topography. The model results show reduced slope angles and an increase of the width of the stream. However, this is not to the extent that was measured.

Nomenclature

Roman symbols

Symbol	Description	Unit
a	Reference level used for defining the concentration	[m]
A	Rouse number	[-]
A	Exposed sediment area	[m^2]
A_{grid}	Area of the grid cell	[m^2]
A_{sh}	Bed slope parameter	[-]
A_T	The area of the triangle defined by three bed level points	[m^2]
B	Channel width	[m]
B_{sh}	Bed slope parameter	[-]
c	Concentration	[kg m^{-3}]
c_{kmx}	Concentration at the middle of the kmx-layer	[kg m^{-3}]
$c_{kmx(bot)}$	Concentration at the bottom of the kmx-layer	[kg m^{-3}]
c_{ref}	Concentration at reference level a	[kg m^{-3}]
$\overline{c}_{ref}$	Time averaged concentration at reference level a	[kg m^{-3}]
$c_{ref}\left(u_i\right)$	Concentration due to the instantaneous velocity at reference level a	[kg m^{-3}]
c'	Perturbation of the time-averaged concentration	[kg m^{-3}]
C_D	Drag coefficient	[-]
C_L	Lift coefficient	[-]
C	Chézy coefficient	[$m^{1/2}$ s^{-1}]
C'	Chézy coefficient of $3\,D_{90}$	[$m^{1/2}$ s^{-1}]
D	Deposition term	[kg m^{-2} s^{-1}]
D_{50}	Median grain diameter	[m]
D_*	Van Rijn dimensionless grain parameter	[-]
E	Pick-up rate or erosion term	[kg m^{-2} s^{-1}]
f	Darcy-Weisbach friction factor	[-]
f_C	Darcy-Weisbach friction factor of the Chézy coefficient	[-]
$f_{C'}$	Darcy-Weisbach friction factor the Chézy coefficient of $3\,D_{90}$	[-]
F_D	Drag force on a particle	[N]
F_L	Lift force on a particle	[N]
g	Gravitational constant (9.8)	[m s^{-2}]
h	Water height	[m]
h_i	Height of a slice i of the slip circle	[m]
i	Hydraulic spatial pressure gradient	[-]
I	impulse on a particle	[N s]
k	Turbulent kinetic energy	[m^2 s^{-2}]
k_l	Permeability of sediment after dilatation	[m s^{-1}]
k_s	Nikuradse roughness	[m]
L_i	Length of the arc at the bottom of slice i	[m]

m	Mass of the particle	[kg]
M	Momentum of the particle	[kg m s^{-1}]
M_D	Driving moment of a slide plane	[N m]
M_R	Resisting moment of a slide plane	[N m]
n	Bed porosity	[-]
n_0	Bed porosity prior to dilatation	[-]
n_l	Bed porosity after dilatation is equal to the maximum porosity	[-]
p	Pressure	[N m^{-2}]
p_i	Pressure of the hydraulic gradient over the bed	[N m^{-2}]
P	Fraction of the time a sediment particle can be picked up by the flow. This is the probability that the Lift force exceeds the weight of a particle.	[-]
$P(u_i)$	Probability density function of a instantaneous velocity u_i	[s m^{-1}]
$P(\tau_i)$	Probability density function of a instantaneous shear stress τ_i	[m^2 N^{-1}]
$P(F_D)$	Probability density function of the drag force on a particle	[N^{-1}]
Q	Flow discharge	[m^3 s]
Q_s	Mass sediment transport	[kg s^{-1}]
R	Radius of a slip circle	[m]
$S_{slump,u}$	Bed load in x-direction due to slumping before update for bed-slope effect	[kg m^{-1} s^{-1}]
$S_{slump,v}$	Bed load in y-direction due to slumping before update for bed-slope effect	[kg m^{-1} s^{-1}]
$S(\tau_i)$	Instantaneous volume sediment transport	[m^3 m^{-1} s^{-1}]
S	Volume sediment transport	[m^3 m^{-1} s^{-1}]
S'	Volume of under-supplied sediment transport	[m^3 m^{-1} s^{-1}]
$\overline{S}$	Time-averaged volume sediment transport	[m^3 m^{-1} s^{-1}]
$t_{impulse}$	Timescale of the impulse on the particle	[s]
T	Van Rijn transport parameter	[-]
T_b	Dimensionless near-bed velocity squared	[-]
u	Velocity in x-direction	[m s^{-1}]
u_b	Near-bed velocity	[m s^{-1}]
$\overline{u}_b$	Time averaged near-bed flow velocity	[m s^{-1}]
u'_{cr} ucr'	Corrected critical velocity for entrainment	[m s^{-1}]
u_{da}	Depth average velocity in x-direction	[m s^{-1}]
u_{kmax}	Velocity in the lowest computational layer	[m s^{-1}]
$u_{p,ini}$	Initial velocity when particle is dislodged	[m s^{-1}]
u_*	Shear velocity	[m s^{-1}]
$u_{*,cr}$	Critical shear velocity	[m s^{-1}]
u'	Perturbation of the time-averaged velocity in x-direction	[m s^{-1}]
v	Velocity in y-direction	[m s^{-1}]
v'	Perturbation of the time-averaged velocity in y-direction	[m s^{-1}]
V_{end}	The volume under the three depth points after a slump	[m^3]
V_{ini}	The initial volume under the three depth points before a slump	[m^3]

V_{slump}	The volume that has to be transported due to a slump	[m^3]
w	Velocity in z-direction	[m s^{-1}]
w'	Perturbation of the time-averaged velocity in z-direction	[m s^{-1}]
w_s	Sediment settling velocity	[m s^{-1}]
x	Horizontal coordinate	[m]
y	Horizontal coordinate	[m]
z	Vertical coordinate	[m]
$z_{\min}$	The minimal height of three depth points in a triangle	[m]
z_{mid}	The median height of three depth points in a triangle	[m]
$z_{\max}$	The maximal height of three depth points in a triangle	[m]
z_0	Roughness height	[m]
$\frac{\partial z_b}{\partial x}$	Bed slope in x direction	[-]
$\frac{\partial z_b}{\partial y}$	Bed slope in y-direction	[-]
$\|\mathbf{u}\|$	Total velocity magnitude	[m s^{-1}]
Δx	Grid size in x direction	[m]
Δx_i	Width of a slice i of the slip circle	[m]
Δy	Grid size in y direction	[m]
Δz	Height difference between the reference concentration level and the middle of the kmx-layer	[m]

Greek symbols

Symbol	Description	Unit
α_1	Ratio of c_{kmx} and $c_{kmx(bot)}$	[-]
α_2	Calibration term in the erosion formula to account for the difference between the discretized and continuous concentration profile	[-]
α_D	proportionality factor between the drag force / shear stress and the near bed velocity squared	[-]
α_E	Calibration coefficient for the Einstein sediment formula	[-]
α_u	An-isotropy parameter for the turbulent kinetic energy	[-]
β_1	correction factor of Van Prooijen and Winterwerp to fit the $\tau_b'/\overline{\tau}_b$ ratio of the measurements	[-]
β_2	correction factor of Van Prooijen and Winterwerp to fit the $\overline{\tau}_b$ value of the measurements	[-]
δ	Reciprocal of the relative near-bed turbulent intensity	[-]
δ	Depth of sediment available at the bed	[m]
δ_a	user-defined erosion threshold	[m]
Δ	Specific density	[-]
Δ_r	Bed form height	[m]
ε_s	Sediment diffusion coefficient	[m^2 s^{-1}]
γ	Angle between the u-velocity and the v-velocity	[-]
γ_i	Weight of the soil of slice i	[N m^{-3}]

η	Bed level	[m]
κ	Von Karman coefficient	[-]
μ_c	Ripple factor	[-]
ν	Kinematic viscosity	[m^2 s^{-1}]
θ	Shields parameter	[-]
θ_{cr}	Critical shields parameter	[-]
ρ_s	Density of the sediment	[kg m^{-3}]
ρ_w	Density of water	[kg m^{-3}]
σ_u	standard deviation of the flow velocity	[m s^{-1}]
τ_b	Bed shear stress	[N m^{-2}]
τ_b'	Reduced bed shear stress with current efficiency factor	[N m^{-2}]
τ_i	Instantaneous bed shear stress	[N m^{-2}]
$\tau_{S,i}$	Shear stress at the bottom of the slice of the slip circle	[N m^{-2}]
ω	Dimensionless near-bed velocity	[-]
ξ_i	Hiding and exposure coefficient for sediment fracture i	[-]

Abbreviations

Symbol	Description
TKE	Turbulent kinetic energy
HFE	High flood experiment
Van Rijn i.t.	Van Rijn including turbulence. The Van Rijn formulation derived in this thesis

Table of contents

1 Introduction

The Colorado River is located in the southwest of the USA. This river springs at the Rocky Mountains and leads to the Gulf of California. The total length of the river is 2330 km. In the state of Arizona the river has been dammed by the Glen Canyon dam in 1963. This dam created Lake Powell, the reservoir upstream of the dam.

Years earlier in 1936, the Hoover dam was built, which created Lake Mead. This is around 560 kilometres downstream of the Glen Canyon dam. These two dams still have a major impact on the Colorado River. They form the outer boundaries of this study. The discharge downstream of the Glen Canyon dam is nowadays more constant than before the construction of the dam.

Between the two dams the Paria River and the Little Colorado confluence with the Colorado River. These rivers provide nowadays the main source of sediment in the system. Figure 1 shows the two dams and rivers.

The coordinate system used in this thesis is the North American datum 1983 (NAD 83). The vertical datum used, is the National Geodetic Vertical Datum 1988 (NGVD 88).

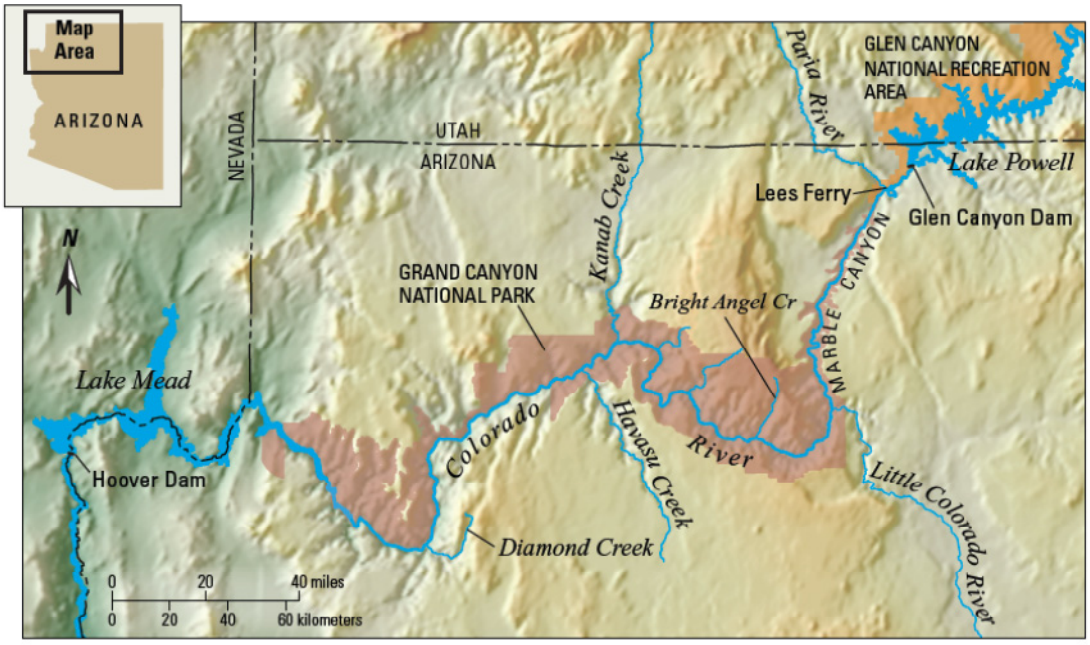

Figure 1.1: Map of the Colorado river between the Glen Canyon dam (east) and the Hoover dam (west) (Melis, 2010)

1.1 Problem: erosion of sandbars

Due to the Glen Canyon dam the sediment gets trapped in Lake Powell and the inflow of sediment to the Colorado River has nearly stopped. Before the closure 22.8 million metric ton of sand a year flowed into the system at Lees Ferry. Now only 0.5% of the original sediment supply is added to the river. The river has two main tributaries, the Paria River and the Little Colorado. The Paria River provides approximately 1.5 million tons of sand per year and the Little Colorado 3 million tons. The

total inflow of sediment including that from the tributaries is now only a fifth of the pre-dam conditions (Topping et al., 2000).

Before the Glen Canyon dam was constructed, the river had to discharge a large amount of melt water in the spring (see black line in Figure 1.2). This caused a flood wave, travelling through the Colorado River. After the construction, the melt water is captured in Lake Powell and discharged over the whole year. Therefore, there are no natural high floods anymore downstream of the dam. These flood waves caused the sediment, which was deposed on the bottom of the river, to be stirred up (see Figure 1.3). Once the sediment was in suspension, it got deposited on the sandbars, by the mechanism described in the next section.

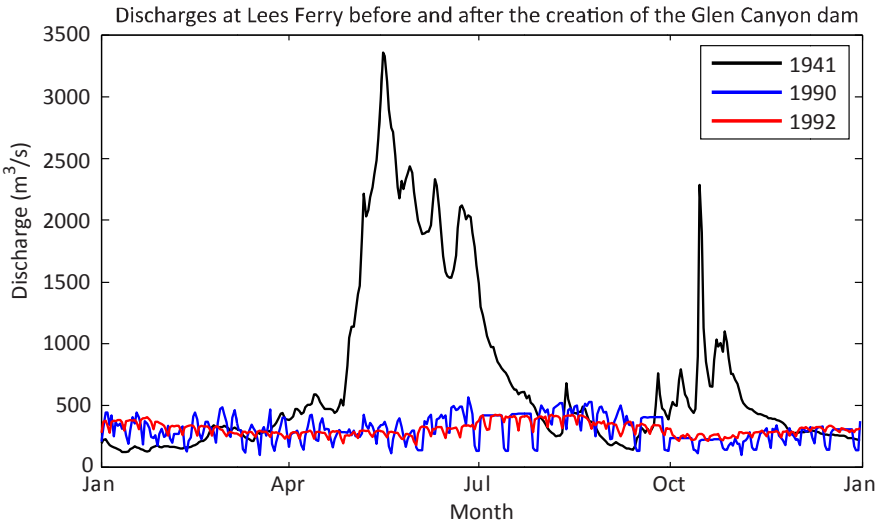

Figure 1.2: Discharge in the Colorado River at Lees Ferry, station number: 09380000. Data retrieved from (USGS, 2011)

Since the closure of the Glen Canyon dam the sandbars and -banks are eroding, due to the limited sediment supply. O'Brien and Pederson showed that 19 percent of the sandbars are seriously or severely eroded (O'Brien and Pederson, 2008). These sandbars are important for the ecosystem of the Colorado River. At the riparian zone, vegetation attracts different kinds of fauna. The stagnant water near the sandbars forms a habitat for native fish, such as the endangered humpback chub (Rubin et al., 2002).

The sandbars have also recreational purposes: many tourists use the sandbars as a campsite, while they raft along the Colorado River. The third function of the sandbars is to protect archaeological sites. For these reasons, many different studies are ongoing about how the sandbars in the Colorado River can be maintained.

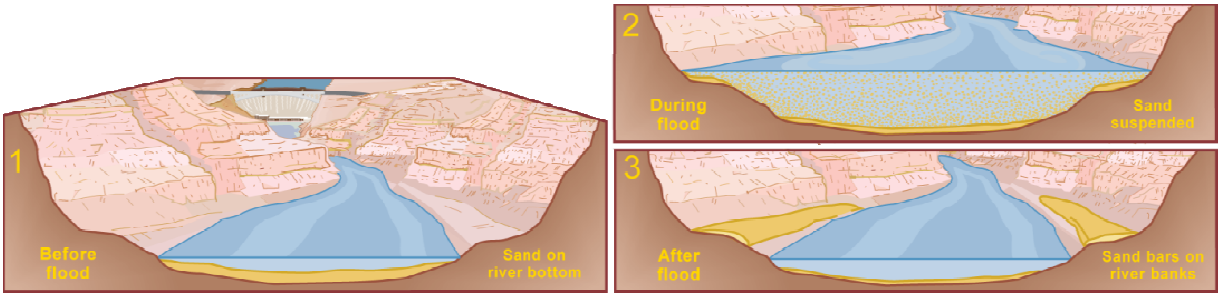

Figure 1.3: Sand on the bottom of the Colorado river will be deposited on the sand banks, after (Anderson et al., 1996)

In the period from 1963 to 1991 the dam operations were primarily aimed at maximizing the power supply from the dam. At night there is less demand for power than at day time, and thus the discharge through the dam was less at night. In this period the volumetric flow would fluctuate from 850m^3/s at day to 142m^3/s at night. This corresponded with a water level variation of 2 to 4 metres per day. This is shown by the blue line in Figure 1.2. After 1991 the variations have been limited (see the red line in Figure 1.2) to improve the safety of fishing and boating on the river (U.S. Department of the Interior, 1988).

1.2 Attempted solution: High Flow Experiments

To mimic the natural seasonal discharges High Flow Experiments (HFE) were conducted. These high flows should deposit sediment on top of the sandbars. In 1996, 2004 and 2008 high flood were released. An HFE can be divided into three parts. The first part is the rising period, which lies left of the green line in Figure 1.4. After this the peak flow follows. In this period a constant, high discharge is released. The last period is the falling period, where the discharge drops again to a normal flow condition.

When an HFE is conducted it is important that there is enough sediment in the river to be deposited at the sand banks. In the late summer or early fall the large tributaries can provide the sediment. (Rubin et al., 2002). The results of the 1996 HFE showed that eddies are the main driving mechanism behind the sedimentation of the sand bars. The sand on the bed had less influence on the sedimentation (Schmidt et al., 1999).

The HFE in 2004 lasted only 2.5 days, instead of the 7 days in 1996 (see Figure 1.4). (Schmidt et al., 1999) showed that the sedimentation occurred in the first two days of the 1996 HFE; therefore the HFE in 2004 was shortened. This experiment was more successful; in the upper part of the Marble Canyon the sandbars increased. However, more downstream the eddies transported sand away from the sandbars. For a total increase in sandbar area more sediment is required (Topping et al., 2006).

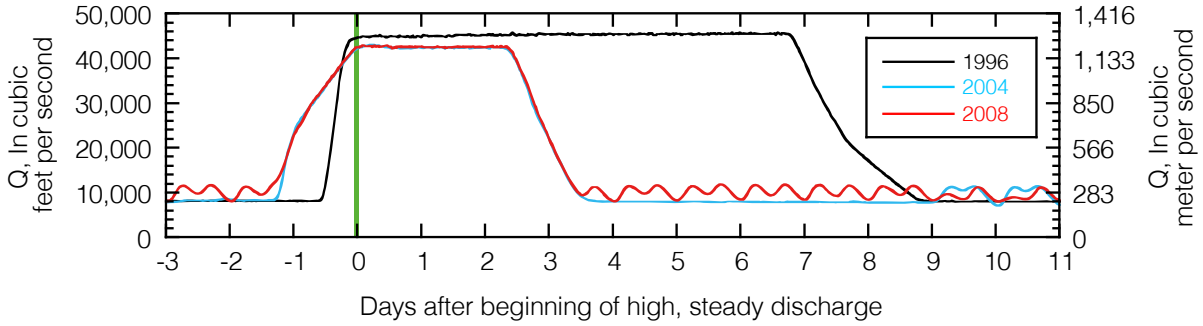

Figure 1.4: Comparison of the flood hydrographs of the 1996, 2004, and 2008 HFEs at the Colorado River at Lees Ferry from (Topping, 2010)

Before the 2008 HFE, the amount of sediment entering via the Paria River was significantly larger than before the 2004 and 1996 flood (Topping, 2009). Figure 1.4 shows that in 2008 daily variations in discharge were present before and after the HFE. These variations are also present during normal operations. The goal of these variations was to observe the influence on the sand bar stability. (Hazel Jr et al., 2010). Kemp modelled the stability of these sand bars during the HFE using the finite element package PLAXIS. Kemp concluded that the stability of the sandbars is improved when the HFE has a longer falling period. No overpressures in the sandbars occur, due to slower draining (Kemp, 2010).

Sandbars are often located downstream of a rapid (Figure 1.5). This rapid is mostly generated due to a clogging of the main channel with sediment from debris flows from tributaries. Downstream of the rapid, when the river widens, an eddy is formed. Near the separation point and near the reattachment point, the flow velocities are low. At these points, sand gets deposed and a sandbar is formed.

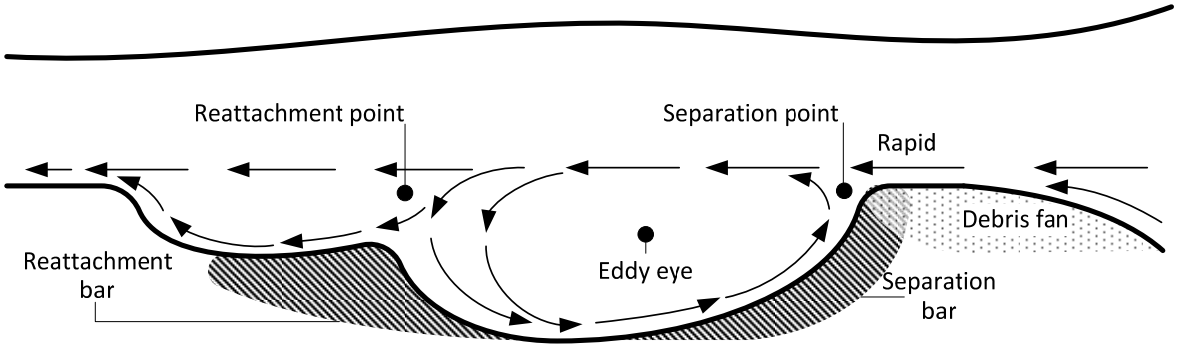

Figure 1.5: Top view of an eddy fan complex, based upon (Hazel Jr et al., 2010)

1.3 Previous model studies

Morphologic model studies of the HFE have been conducted to see how to maximize the sand deposition on top of the sandbars in the whole Colorado River between the Glen Canyon dam and the Hoover dam. During the 2008 flood, two pools were extensively monitored. These two pools lie about 70 km (45 miles) downstream of the Glen Canyon dam (Figure 1.6). Figure 1.7 shows a detailed aerial photograph of the two pools: the Eminence pool followed downstream by the Willy Taylor pool. Figure 1.8 shows the measured topography of the Eminence pool after the 2008 HFE.

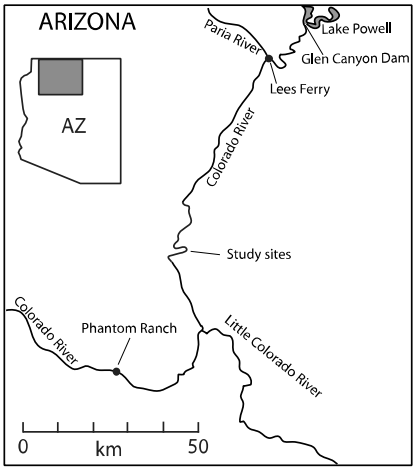

Figure 1.6: Map showing the location of the study site (Wright and Kaplinski, 2011)

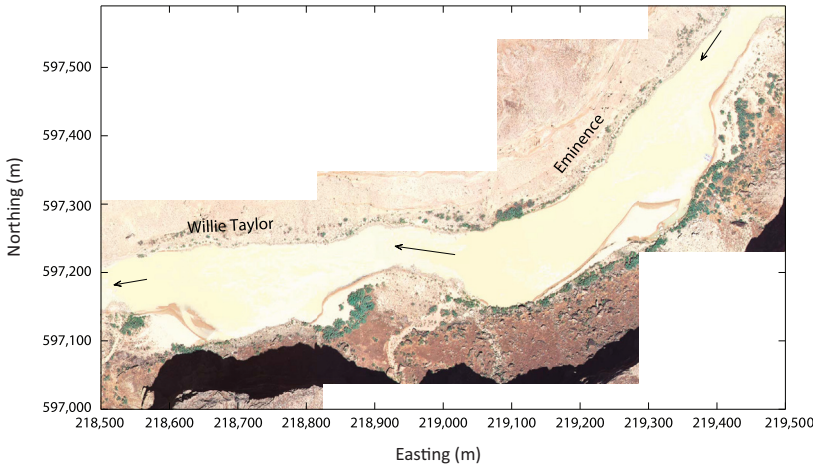

Figure 1.7: Aerial photograph of the two pools modelled by Kemp (Wright and Kaplinski, 2011)

The processes in the pools have been modelled by (Sloff et al., 2009), (Kemp, 2010) and (Logan et al., 2010). Sloff made a 3D model in the modelling package Delft3D (Sloff et al., 2009). The flow on the boundary of the eddy and the main stream has a helical flow pattern. This cannot be modelled in a 2D model; therefore a 3D model is more suitable. Another advantage of a 3D model is the computed velocity and sediment profile over the vertical. A 2D model assumes a logarithmic velocity profile and a Rouse profile to describe the sediment concentration. In a steady flow this approximation will hold.

However, during the HFE the flow velocities will increase very fast, therefore the vertical velocity profile will differ from the logarithmic profile.

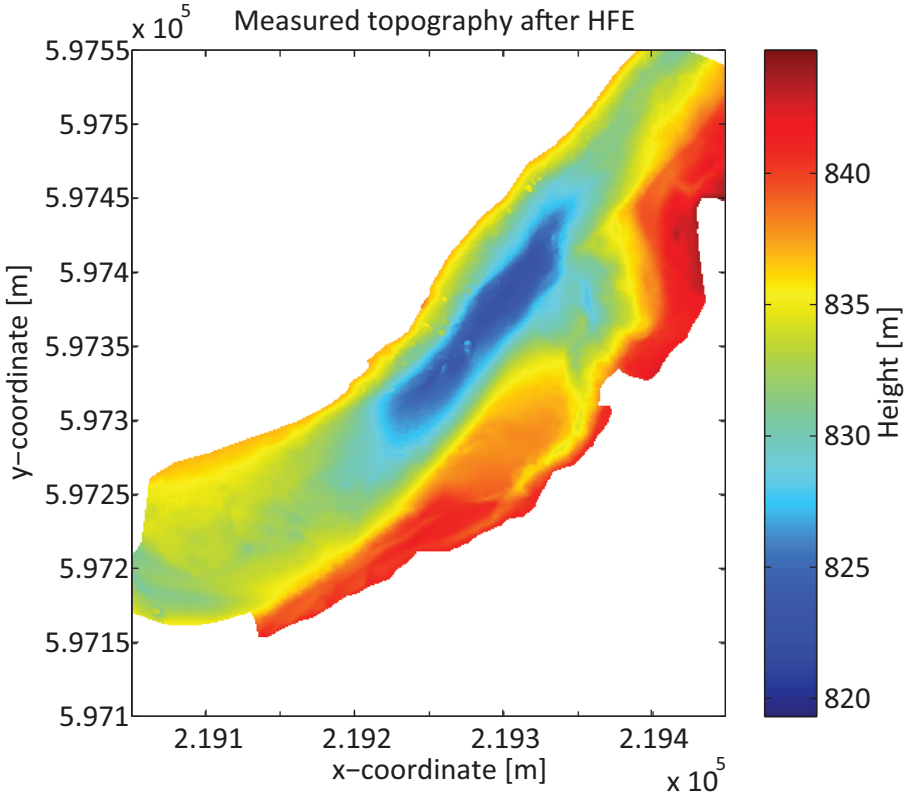

Figure 1.8: Measured topography of the Eminence pool after the 2008 HFE

Liz Kemp studied different shapes of the HFE for optimal sand deposition (Kemp, 2010). Kemp concluded that most sediment is deposited in the first 19 hours after the start of the peak flow. When the HFE has a very short peak flow, it may dampen too much when it travels through the river. Such a flood, with a long rising and falling period and with a low peak flow, will not deposit sand on the sand bars downstream. Moreover, when the peak of the HFE lasts too long, all the sediment gets flushed through the system.

The sedimentation of the Willy Taylor bar was modelled well, however the reattachment bar of the Eminence pool was extended more into the pool in the model than in reality. Figure 1.9 shows the computed bed level after the 2008 HFE. Figure 1.10 shows the difference between Kemps computed bed level for the Eminence pool and the measured topography.

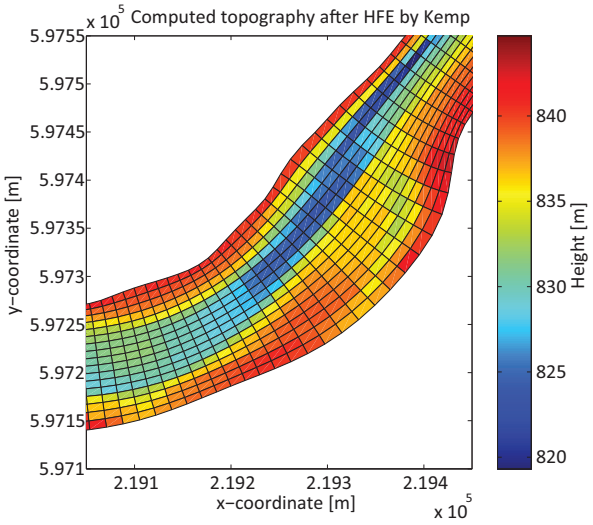

Figure 1.9: Computed bed level after 2008 HFE by Kemp

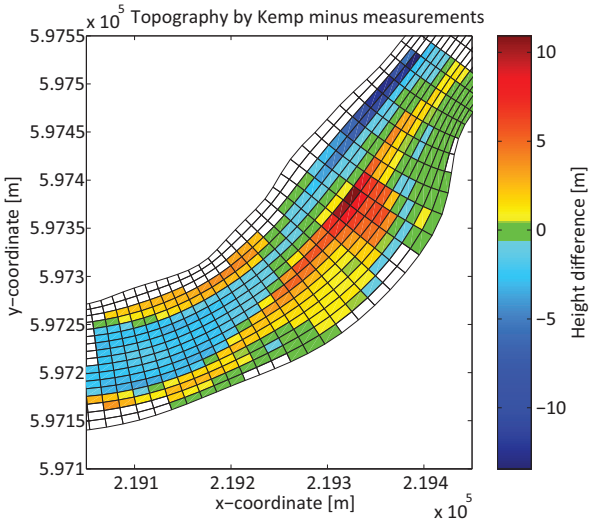

Figure 1.10: Computed topography by Kemp minus measured topography of the Eminence pool

Brandy Logan adopted the model of Kemp, but left out the downstream Willy Taylor pool, because the topography between the pools had not been measured before and during the 2008 HFE (Logan et al., 2010). Because the topography was not known, the computed water levels in the model differed much from the measured water levels. The computed topography of the Eminence pool is shown in Figure 1.11. In Figure 1.12 the difference between the measured and computed bed level after the high flood experiment is visualised.

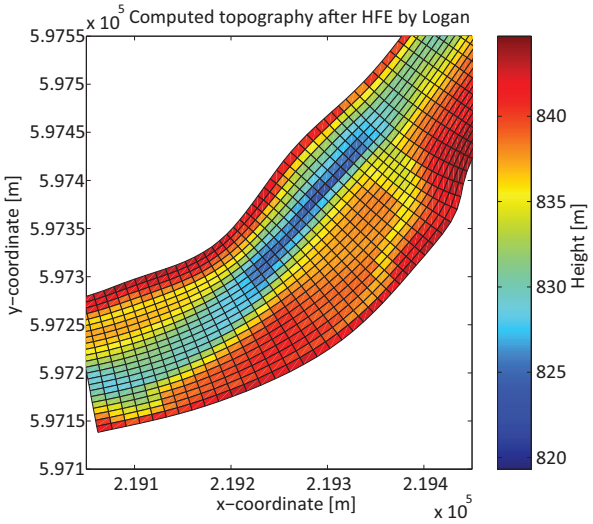

Figure 1.11: Computed bed level after 2008 HFE by Logan

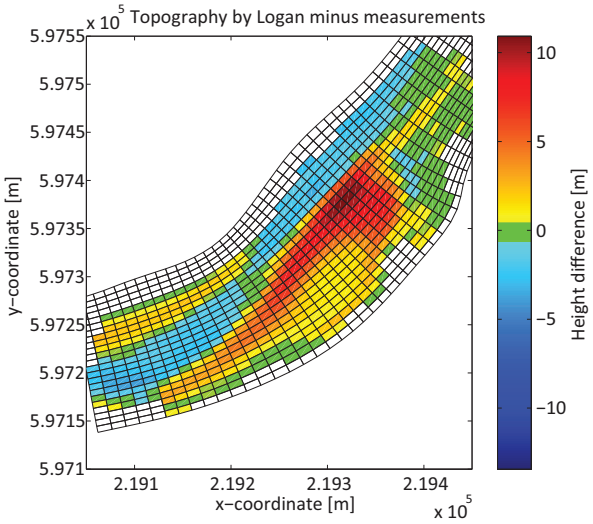

Figure 1.12: Computed topography by Logan minus measured topography of the Eminence pool

The computed bed levels of Kemp and Logan (respectively Figure 1.10 and Figure 1.11) show similar results. The model of Logan has a higher resolution and shows a more distinct topography. Both models predict sedimentation on the separation bar well (green area in Figure 1.10 and Figure 1.12). The models show sedimentation on the reattachment bar. The sedimentation on the right bank (in downstream direction) is slightly a bit over-predicted.

At the left bank a return channel is visible in the measurements (Figure 1.8). This return channel is also visible in the computed topographies of Kemp and Logan.

However, both models show also large deviations with the measurements. There is more deposition on the sandbar and it extents more into the Eminence pool. The main stream is smaller in the computations than in reality. The computations show a growth of reattachment-bar in lateral direction, while this is not shown in the measured topography. The Eminence pool was eroded after the 2008 HFE. Yet, both the computations show an extension of the Eminence reattachment bar at this location. Also the computed slopes of the bank of the reattachment bar were 40 degrees, which is significantly higher than the angle of repose.

1.4 Problem analysis

The deficits of the computed topography are due to two deficits in the model. The first deficit of the model is that the sediment transport only accounts for the mean flow velocities. Sloff stated that during the 2008 HFE surface boils had been present (Sloff et al., 2009). These indicate a spot of increased turbulence. At the same location a scour hole was created. In the model results increased turbulence has been present on the bank slopes. The turbulent velocities may also be a factor that widens the main channel as erosion on the bank is enhanced by increased turbulent velocity fluctuations.

The second deficit in the model is that the slopes in the model can grow steeper than the angle of repose. There is no slope slumping or avalanching mechanism in Delft3D. Avalanching will prevent the slopes in Delft3D from becoming too steep, while a slumping method will simulate a large-scale geo-technical instability. When such formulation would be included the steep slopes at the bank would be avalanching, therefore the modelled channel would not become smaller during the simulation of the 2008 HFE. At the rising part of the hydrograph large slope slumps occur. These influence the topography of the river to a great extent.

1.5 Thesis objectives

The goal of this thesis is to investigate the deficits of the Eminence pool model. The two research questions follow from this objective:

1. How can the observed sedimentation and erosion processes be better reproduced with a probabilistic approach for near-bed sediment transport in a continuum model like Delft3D?

2. How can the failure of steep sub-aquatic slopes be simulated and incorporated in a continuum flow and morphology model like the Delft3D model?

1.6 Thesis outline

The next two chapters describe respectively the probabilistic approach for the near-bed sediment transport and the failure of sub-aquatic slope failures. Both chapters have the same structure. First, the state of the art is discussed. Thereafter, the methodology used in this thesis is mentioned. The last section of both chapters include simple Delft3D test models to see whether the behaviour of the methods match with reality.

Chapter four starts with describing the previous attempts to model the Eminence pool. Then the model which is used in this thesis is described. The last section describes the results of that model. Chapter five gives the conclusions of this thesis and the final chapter gives recommendations on the

erosion of the sandbars and on further research into probabilistic approaches for sediment transport and slope slumping.

2 Development of a probabilistic transport function

2.1 State of the art

2.1.1 Hydrodynamic and morphodynamic behaviour at the bed

The flow in a river is forced by its topography and the discharge. It is subjected to pressure differences, the advection of momentum, the diffusion of momentum and the dissipation of energy. Changes in topography can be a forcing for large-scale eddies. These eddies have length scales equal to the width of the river and are also visible at the Eminence pool. The main flow of the river is in downstream direction. Due to the eddies the flow can locally be in the reverse direction. The local flow is not steady in time or in space. These fluctuations are called turbulence. This turbulence is also present at the bed and can cause a local velocity to be higher than the average velocity.

The flow including turbulent velocity fluctuations induces a force on the particles lying on the bed. In Figure 2.1 the forces on the particles are illustrated. Due to horizontal pressure difference, a pressure force acts on them. When a particle is exposed the water has to flow around it. This induces a vertical flow and a corresponding decrease in pressure. This decrease in pressure acts as a lift force on the sand particle.

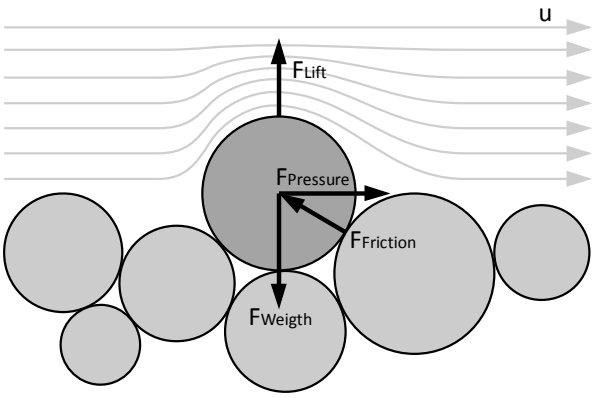

Figure 2.1: Flow induced forces on particles lying on the bed

The lift force can be explained using the stationary Euler equations governing inviscid flow for an incompressible fluid in 2D. These equations describe a frictionless situation. This holds for a flow were no momentum is transported due to diffusion. The equations are:

$$\rho\left(u\frac{\partial u}{\partial x}+w\frac{\partial u}{\partial z}\right)=-\frac{\partial p}{\partial x} \tag{2.1}$$

$$\rho\left(u\frac{\partial w}{\partial x}+w\frac{\partial w}{\partial z}\right)=-\frac{\partial p}{\partial z}+\rho g \tag{2.2}$$

When equation (2.2) is integrated with respect to z equation (2.3) is obtained

$$\int\frac{\partial p}{\partial z}dz=\int\left(\rho g-\rho w\frac{\partial w}{\partial z}-\rho u\frac{\partial w}{\partial x}\right)dz \tag{2.3}$$

The solution of the integral is presented in equation (2.4)

$$p = \rho g z - \tfrac{1}{2}\rho w^2 - C \tag{2.4}$$

The pressure consists of three parts: first, the hydrostatic pressure, then the dynamic pressure and last the integration constant from the integration.
The vertical flow velocity beneath the exposed particle is practically zero. The pressure is therefore equal to the hydrostatic pressure. Above the particle the pressure is reduced with the dynamic pressure, therefore the total pressure will be upward, thus creating a lift force.

Sediment transport and bed level change

When the forcing on the particles becomes larger than the weight of the particle and the friction forces between the particles, the particles start to be entrained. The entrained particles can be transported as bed load or as suspended load. When sediment is transported as bed load the grains roll and jump along the bed. The particles touch the bottom every few metres. In the case of suspended load the sediment is picked up higher into the water column and is transported by the local flow.

The bed load transport can be described using the amount of particles that has been entrained multiplied with the near-bed velocity. The suspended load over the vertical in a steady flow can be described using the Rouse profile of equation (2.5). A parabolic vertical eddy viscosity is assumed for deriving the Rouse profile. The flow velocities over the vertical are then described with a logarithmic function. The Rouse profile is in this form only valid for small concentrations ($c < c_{ref} < 2$ kg m^{-3}). In fluids with a higher concentration, the particles movements interfere with each other. This leads to a hindered settling velocity. Instead of the particle fall velocity, the hindered fall velocity should be used in the Rouse number.

$$c(z) = c_{ref}\left(\frac{a(h-z)}{z(h-a)}\right)^{A} \tag{2.5}$$

Where:

$c(z)$	Concentration as a function of depth [kg m^{-3}]
c_{ref}	Reference concentration set at level a [kg m^{-3}]
a	Reference level [m]
h	Water height [m]
z	Height from the bottom [m]
A	Rouse number $w_s/\kappa u_*$ [-]

The transport of suspended sediment is calculated by multiplying the local concentration with the local velocity. Both can be decomposed in a mean and a fluctuating part with Reynolds decomposition. For the concentration the mean quantity is the sediment that is entrained due to the mean velocity. The fluctuating concentration is the sediment for which the fluctuating velocity is responsible for the entrainment (equation (2.6)).

$$Q_s = B\,h\overline{\left[c + c'\right] \cdot \left[u + u'\right]} \tag{2.6}$$

When the terms are multiplied and the Reynolds averaging is applied equation (2.7) is obtained.

$$Q_s = B\,h\left(\overline{c\,u} + \overline{c\,u'} + \overline{c'\,u} + \overline{c'\,u'}\right) \tag{2.7}$$

The second and third term involve an averaged and a fluctuating quantity. The average of the fluctuating quantity is zero; therefore these two terms are zero. The average of the forth term is non-zero, because the fluctuating velocity and concentration are not fully correlated. Equation (2.8) shows the final result.

$$Q_s = B\,h\left(\overline{c\,u} + \overline{c'\,u'}\right) \tag{2.8}$$

where:

Q_s	Mass sediment transport [kg s^{-1}]
h	Water height [m]
B	Channel width [m]
c	Average concentration [kg m^{-3}]
c'	Perturbation of the time-averaged concentration [kg m^{-3}]
u	Average velocity [m s^{-1}]
u'	Perturbation of the time-averaged velocity [m s^{-1}]

In a highly turbulent flow the second term of equation (2.8) becomes more dominant for the sediment transport.

The bed level change as a function of the sediment transport can be described using the Exner equation if there is no change in lateral direction:

$$B\,\rho_s \frac{\partial \eta}{\partial t} = -\frac{1}{\left(1-n\right)} \frac{\partial Q_s}{\partial x} \tag{2.9}$$

Where

ρ_s	Density of the sediment [kg m^{-3}]
$\frac{\partial \eta}{\partial t}$	Bed level change over time [m s^{-1}]
n	Porosity [-]
$\frac{\partial q_s}{\partial x}$	Spatial sediment transport gradient [kg m^{-2} s^{-1}]

An increase in sediment transport over a distance leads to a decrease in bed level. This is understandable because the sediment for the increase in transport has to come from the bed.

Dilatant behaviour of sand

When a shear stress is applied over a bed of dense packed sand grains (left part of Figure 2.2), the grains start to roll over each other. This results in a less dense packing of the sand. Dilatant behaviour occurs when grains are more densely packed than the critical density. This is the case when it is

densely packed sand. This hinders the erosion. When it is loosely packed sand its behaviour is contractant. The dilatant behaviour acts as a counterforce on the sediment entrainment.

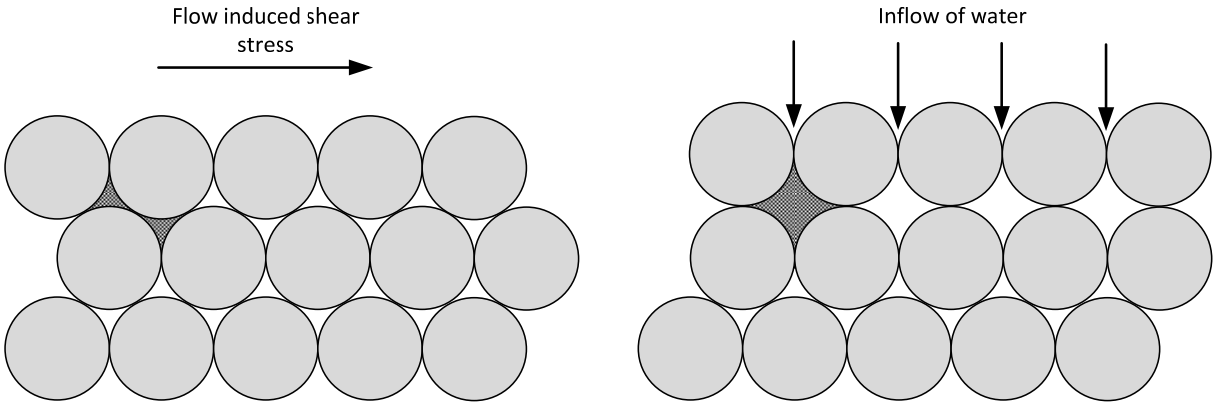

Figure 2.2: The effect of dilatancy. Left: dense packed grains before dilatating, Right: loose packed sand after dilatating, with the inflow of water.

The hydraulic gradient over the bed is (Mastbergen and Van Den Berg, 2003):

$$i = \frac{v_e}{k_l} \cdot \frac{n_l - n_0}{1 - n_l} \tag{2.10}$$

The corresponding pressure is (Van Rhee, 2010, Bisschop et al., 2011):

$$p_i = \rho_w \, g \, i \tag{2.11}$$

where:

i Hydraulic spatial pressure gradient [-]

k_l Permeability of sediment bed after dilatation [m/s]

v_e Erosion velocity [m/s]

n_0 Bed porosity prior to erosion [-]

n_l Bed porosity after dilatation, estimated as the maximum porosity [-]

p_i Pressure of the hydraulic gradient over the bed [N m^{-2}]

The pressure on the bed induced by the dilatation reduces the erosion velocity (v_e).

To include this feature accurately into Delft3D, the volume of the sediment should be described using different porosities for every grid-cell. When sediment is recently deposited a different porosity should be used than for sediment that has been on the bed for a longer time. A shear stress lower than the critical shear stress would contract the particles with a high porosity, but does not entrain them. This leads to a lower porosity. This contracting behaviour and the use of a porosity-value for every grid-cell should be implemented first, before the dilating behaviour can be implemented.

2.1.2 Morphodynamic behaviour implemented in Delft3D

Alluvial bed

The flow in the river induces ripples and dunes on an alluvial bed. These ripples introduce a roughness at the bottom and therefore lower the flow velocities. The computational grid size is too large to include these ripples and dunes. The computational grid size is of the order metres to tens of metres and the ripples have a length scale of centimetres to decimetres. To include these ripples, a ripple factor (μ_c) is introduced. This factor is smaller than 1. It is based on the Darcy-Weisbach coefficient of the Nikuradse roughness (C) compared to that of the Chézy coefficient of $3 \cdot D_{90}$ (C'). First the Nikuradse roughness is related as a Chézy coefficient (equation (2.12))

$$C = 18 \log\left(\frac{12h}{k_s}\right) \tag{2.12}$$

The bed shear stress can be defined using the Chézy coefficient or the Darcy-Weisbach friction factor. In equation (2.13) the Darcy friction factor is related to the Chézy coefficient.

$$\left.\begin{aligned} \tau_b &= \rho g \frac{u_{da}^2}{C^2} \\ \tau_b &= \tfrac{1}{8} f \rho u_{da}^2 \end{aligned}\right\} \tfrac{1}{8} f = \frac{g}{C^2} \rightarrow f = \frac{8g}{C^2} \tag{2.13}$$

When equation (2.12) is substituted in equation (2.13), equation (2.14) is obtained.

$$f_C = 8g \cdot \left(18 \log\left(\frac{12h}{k_s}\right)\right)^{-2} \approx 0.24 \left(\log\left(\frac{12h}{k_s}\right)\right)^{-2} \tag{2.14}$$

The same substitution can be done for the Chézy coefficient of $3 \cdot D_{90}$:

$$f_{C'} = 0.24 \left(\log\left(\frac{12h}{3D_{90}}\right)\right)^{-2} \tag{2.15}$$

The ripple factor is obtained by dividing equation (2.15) by equation (2.14):

$$\mu_c = \frac{f_{C'}}{f_C} \tag{2.16}$$

The reduced bed shear stress is:

$$\tau_b' = \mu_c \cdot \tau_b \tag{2.17}$$

Effect of non-alluvial layers on sediment transport

Another important phenomenon is the absence of sediment on the bottom. On the rocky bed of the Colorado River, not everywhere sediment is available to be suspended. Struiksma defined a supply limited suspended sediment load based on the ratio of the alluvial depth and the maximum thickness of alluvium (Figure 2.3). This imposes an external forcing on the system and modifies the free morphological behaviour. (Struiksma, 1999)

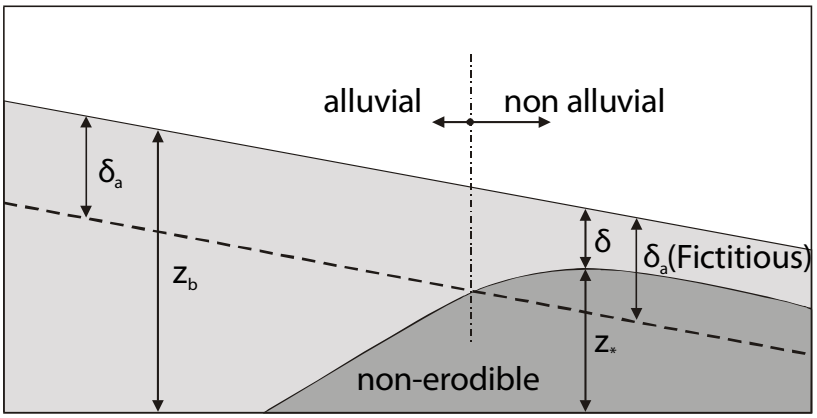

Figure 2.3: description of erodible and non-erodible layers (Struiksma, 1999)

The Delft3D model incorporates the under-supply of sediment according to a linear factor (equation (2.18)). This factor is used for the bed-load transport and for the suspended sediment transport. (Deltares, 2010)

$$S' = \frac{\delta}{\delta_a} S \tag{2.18}$$

Where:

S	Volume sediment transport before fixed layer effects and correction for bed slope effects [$m^3\ m^{-1}\ s^{-1}$]
S'	Volume of under-supplied sediment transport [$m^3\ m^{-1}\ s^{-1}$]
δ/δ_a	Upwind fixed layer proximity factor, limited from 0 to 1
δ	Depth of sediment available at the bed [m]
δ_a	User-defined erosion threshold [m]

In Logan's model of the Eminence pool and the Willy Taylor pool, the erosion threshold value is set to 0.01 m. Thus, when a sediment layer of more than a centimetre is available, the sediment transport is not hindered by the fixed bottom. This is the same as the threshold value in the model of (Struiksma, 1999).

Bed slope effects

On flat beds the direction of the bed load transport is the same direction as the bed shear stress. When beds have an angle, sediment particles experience a gravity force down the slope. This will cause the direction of the bed load transport to differ from the bed shear stress direction. The Koch and Flokstra formula for this effect reads: (Koch et al., 1980).

$$\tan\alpha = \frac{\sin\gamma - \frac{1}{f_s(\theta)}\frac{\partial z_b}{\partial y}}{\cos\gamma - \frac{1}{f_s(\theta)}\frac{\partial z_b}{\partial x}} \tag{2.19}$$

$$\gamma = \arctan\left(\frac{v_b}{u_b}\right) \tag{2.20}$$

$$f_s(\theta) = A_{sh}\theta^{B_{sh}} \tag{2.21}$$

In equation (2.19) the angle of the bed load transport is based on the angle of the flow velocity minus the gravity forces. The two constants in equation (2.21) are calibration factors.

Transport formulation of Van Rijn

In the model of the Eminence pool the reference concentration for the suspended sediment is calculated with the Van Rijn 1993 formula (Van Rijn, 1993). The bed-load is calculated with using a formation provided by Van Rijn (internal reference of personal communication in (Lesser et al., 2004)) Both formulations use the Shields parameter. This parameter shows the ratio between the bed shear stress ($\tau_b = \rho \cdot u_*^2$) and the sub-aquatic weight of a sand particle ($W = \left(\rho_s - \rho\right) \cdot g \cdot D$).

$$\theta = \frac{\rho_w \cdot u_*^2}{\left(\rho_s - \rho_w\right) \cdot g \cdot D_{50}} = \frac{u_*^2}{\Delta \cdot g \cdot D_{50}} \tag{2.22}$$

$$\Delta = \frac{\rho_s - \rho_w}{\rho_w} \tag{2.23}$$

Where

u_*	Shear velocity [m s^{-1}]
D_{50}	Median grain diameter [m]
g	Gravitational constant [m s^{-2}]
Δ	Specific density [-]
ν	Kinematic viscosity [m^2 s^{-1}]
ρ_s	Density of the sediment [kg m^{-3}]
ρ_w	Density of water [kg m^{-3}]

For every particle diameter there is a threshold at which it will be entrained by the flow. This threshold is given by the critical Shields parameter (θ_{cr}). For this parameter an analytical expression is made (van Rijn, 1984)

$$\begin{array}{rlll} D_* \le 4 & \theta_{cr} = 0.24\left(D_*\right)^{-1} & \tau_{cr} = 0.24 \cdot \left(\rho_s - \rho\right) \cdot g \cdot D \cdot \left(D_*\right)^{-1} \\ 4 \le D_* \le 10 & \theta_{cr} = 0.14\left(D_*\right)^{-0.64} & \tau_{cr} = 0.14 \cdot \left(\rho_s - \rho\right) \cdot g \cdot D \cdot \left(D_*\right)^{-0.64} \\ 10 \le D_* \le 20 & \theta_{cr} = 0.04\left(D_*\right)^{-0.10} & \tau_{cr} = 0.04 \cdot \left(\rho_s - \rho\right) \cdot g \cdot D \cdot \left(D_*\right)^{-0.10} \\ 20 \le D_* \le 150 & \theta_{cr} = 0.013\left(D_*\right)^{0.29} & \tau_{cr} = 0.013 \cdot \left(\rho_s - \rho\right) \cdot g \cdot D \cdot \left(D_*\right)^{0.29} \\ D_* > 150 & \theta_{cr} = 0.055 & \tau_{cr} = 0.055 \cdot \left(\rho_s - \rho\right) \cdot g \cdot D \end{array} \tag{2.24}$$

The dimensionless grain parameter used in equation (2.24) is

$$D_* = D_{50} \left(\frac{\Delta \cdot g}{\nu^2} \right)^{1/3} \tag{2.25}$$

Equation (A.16) of appendix A.5 specifies velocities over the depth using a specified shear velocity. In equation (2.26) the shear velocity is related to the depth averaged velocity.

$$u_* = \frac{u_{da} \cdot \kappa}{\ln\left(1 + \frac{z\left(u_{da}\right)}{z_0}\right)} \tag{2.26}$$

The reference concentration and the bed-load transport use two dimensionless parameters: the transport stage parameter (T) and the dimensionless grain parameter (D_*)

$$T = \frac{\mu_c \cdot \left(u_*\right)^2 - \left(u_{*,cr}\right)^2}{\left(u_{*,cr}\right)^2} \tag{2.27}$$

where

u_* Bed-shear velocity [m s^{-1}]

$u_{*,cr}$ Critical bed-shear velocity according to Shields [m s^{-1}]

u_{da} Depth average flow velocity [m s^{-1}]

The near-bed reference concentration is calculated using:

$$c_{ref} = 0.015\rho_s \frac{D_{50}}{a} \frac{T^{1.5}}{D_*^{0.3}} \tag{2.28}$$

$$a = \max\begin{pmatrix} k_s \\ \frac{1}{2}\Delta_r \\ 0.01h \end{pmatrix} \tag{2.29}$$

where:

c_{ref} Reference concentration [kg/m^3]

D_{50} Median grain diameter [m]

a Reference level [m]

T Transport stage parameter [-]

D_* Dimensionless grain parameter [-]

k_s Nikuradse roughness [m]

Δ_r Bed-form height [m]

h Water height [m]

The formulation of the reference level in Delft3D differs slightly from (van Rijn, 1984). Delft3D assigns a maximum value to the reference level, $a = 0.20h$. The second difference is the reference level with respect to the equivalent roughness height. This is defined in Delft3D as $a = AKSFAC \cdot k_s$, where AKSFAC is a user defined proportionality coefficient. However, the default value for this coefficient is one.

The Van Rijn formula for bed load transport reads (Lesser et al., 2004):

$$S_b = 0.5\ \rho_s\ D_{50}\ u_*\ \sqrt{\mu_c}\ D_*^{-0.3}\ T \tag{2.30}$$

2.1.3 Present literature on sediment entrainment

All the methods presented in this section are probabilistic methods. Currently, all the transport formulations currently implemented in Delft3D are deterministic. The advantage of a probabilistic method is the use of the instantaneous velocity instead of the time-averaged velocity. All the probabilistic methods use a distribution for the instantaneous velocity. In a deterministic approach

the time-averaged velocity and the threshold for entrainment are used. In the probabilistic approach a distribution for the instantaneous velocity is used. Most distributions use a mean value and a standard deviation. The mean value is the computed velocity in a specific grid-cell. A standard deviation for the flow velocity can to be obtained using the calculated turbulent kinetic energy.

Impulses on a particle

Celik described the dislodgement of uniform particles under turbulent flow conditions, using the turbulent impulse to describe the dislodgement (Celik et al., 2010). A flume experiment was carried out with densely packed spherical particles with a diameter of 12.7 mm.

$$I = F_D \cdot t_{impulse} \sim u_b^2 \cdot t_{impulse} \tag{2.31}$$

Where:

I Impulse on a particle [N s]

F_D Drag force on a particle [N]

$t_{impulse}$ Timescale of the impulse on the particle, see Figure 2.4 [s]

u_b Near-bed velocity [m s^{-1}]

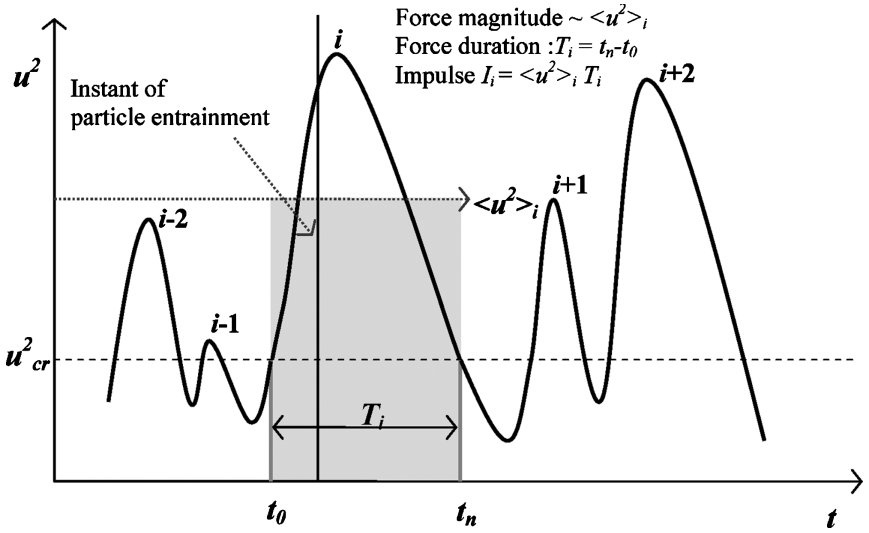

Figure 2.4: Impulse timescale. After (Celik et al., 2010)

A lognormal distribution is used to describe the impulse. The standard deviation of this distribution is determined using the coefficient of variation. A regression analysis showed a linear expression between the coefficient of variation and the particle Reynolds number.

The theoretical threshold was defined as the momentum of the particle, when it starts moving:

$$M = m \cdot u_{p,ini} \tag{2.32}$$

Where:

M Momentum of the particle [kg m s^{-1}]

m Mass of the particle [kg]

$u_{p,ini}$ Initial velocity when particle is dislodged [m s^{-1}]

The initial velocity in equation (2.32) is calculated by equating the velocity head to the potential energy that the particle gains after it is lifted. The potential energy is set to a value of 0.4 mm. The initial velocity calculated this way, did not match with the measurements.

According to Celik this is a better method to describe sediment transport under turbulent conditions. However, no distinction is made between bed load transport and suspended transport. Another problem is the threshold for movement defined by the momentum. This depends on local bed topography, such as grain size, shape, exposure and packing density. Unfortunately, no expressions have been developed yet. This method still has too many unsolved issues to implement, however when more experimental data is known, it can be a new way of describing sediment entrainment.

Forces on a particle

A second method is a force balance of the particles. The flow near the bed induces two forces on a particle: a drag force and a lift force. The drag force acts in the direction of the flow, the lift force in upward direction. The first who used a probabilistic approach for an entrainment formulation based on a lift force was Einstein. Einstein proposed a probabilistic pick-up rate formula (Einstein, 1950).

$$E = \alpha_E \, \rho_s \sqrt{\Delta \, g \, D_{50}} \, P \tag{2.33}$$

where:

E Pick-up rate [kg m^{-2} s^{-1}]

P Fraction of the time a sediment particle can be picked up by the flow. This is the probability that the Lift force exceeds the weight of a particle.

α_E Calibration coefficient

D_{50} Median particle diameter

For the lift force a normal distribution was used with a standard deviation varying in time

Wu, Yang, Chou and Lin used the drag force and the lift force to describe particle entrainment (Wu and Yang, 2004, Wu and Chou, 2003, Wu and Lin, 2002).

$$F_D = \tfrac{1}{2} \rho_w \, u_b^2 \, \xi_i \, C_D \, A \tag{2.34}$$

$$F_L = \tfrac{1}{2} \rho_w \, u_b^2 \, \xi_i \, C_L \, A \tag{2.35}$$

where:

F_D Drag force acting on a particle [N]

F_L Lift force acting on a particle [N]

ρ_w Density of water [kg m^{-3}]

ξ_i Hiding and exposure coefficient for sediment fracture *i* [-]

C_L Lift coefficient [-]

C_D Drag coefficient [-]

A Exposed sediment area [m^2]

To move a particle, the force has to exceed a certain threshold. For suspended transport the lift force has to be larger than the weight of the particle as illustrated in Figure 2.5. The threshold for rolling transport is caused by the moment of the weight around a downstream contact point (the black dot). The moment caused by lift force and drag force forces the transport.

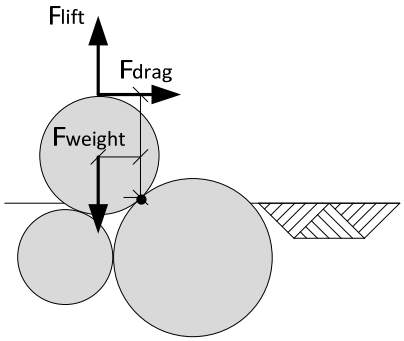

Figure 2.5: Forces on a single particle, including the moment arms to the contact point.

Several studies have been performed toward particle entrainment using forces on particles. Especially the probability density function of the instantaneous velocity differs. Cheng and Chiew used a Normal distribution for the instantaneous velocity. This is later verified with experiments carried out by Papanicolaou. (Papanicolaou et al., 2002). Other studies (Wu and Lin, 2002, Wu and Chou, 2003) use a lognormal distribution for the instantaneous velocity. This distribution is positive skewed distribution. A fourth order Gram-Charlier distribution is also used for describing the velocities. This advantage of this distribution is that not only the standard deviation, but also the skewness and flatness can be specified.

Shear stresses

Kleinhans and Van Rijn made a probabilistic version of Van Rijn 1993. Kleinhans and Van Rijn based bed-load transport and suspended load transport on the instantaneous shear stress times the probability of occurrence of that shear stress (Kleinhans and Van Rijn, 2002). After which, the total is integrated from a shear stress of minus infinity to plus infinity (equation (2.36)).

$$\overline{S} = \int_{-\infty}^{\infty} S(\tau_i) P(\tau_i) \mathrm{d}\tau_i \tag{2.36}$$

where

$\overline{S}$ Time-averaged volume sediment transport [$m^3\ m^{-1}\ s^{-1}$]

$S(\tau_i)$ Instantaneous volume sediment transport [$m^3\ m^{-1}\ s^{-1}$]

$P(\tau_i)$ Probability density function of a instantaneous shear stress τ_i [$m^2\ N^{-1}$]

τ_i Instantaneous bed shear stress [$N\ m^{-2}$]

In practice it is not possible to numerically integrate from minus to plus infinity. Bridge and Bennet assumed that a width of 6 standard deviations include most of the function (Bridge and Bennett, 1992).

Kleinhans and Van Rijn used a normal distribution to describe the instantaneous shear stress. The standard deviation was based on a relative turbulence intensity of 0.4. The critical shear stress for

entrainment was based upon the critical Shields parameter. A hiding and exposure factor was included to obtain the critical shear stress. (Kleinhans and Van Rijn, 2002)

Hofland and Battjes derived a formula to describe the bed load transport. (Hofland and Battjes, 2006). Papanicolaou proposed a normal distribution for the near-bed velocity (u_b) (Papanicolaou et al., 2002). The near-bed velocity squared (u_b^2) would then have a non-central χ^2 distribution with 1 degree of freedom. Hofland and Battjes used the normal distribution for u_b and evaluated the distribution of $u_b|u_b|$. The drag force on sediment particles and the bed shear stress are proportional to $u_b|u_b|$.

The drag force is, $F_D = \alpha_D |u_b| u_b$. The probability density function for F_D is

$$P(F_D) = \frac{1}{2\sqrt{2\pi\,\alpha_D |F_D|}} \exp\left[-\frac{1}{2}\left(\sqrt{\frac{|F_D|}{\alpha_D}} - \frac{F_D}{|F_D|}\delta\right)^2\right] \tag{2.37}$$

where

$\delta = \frac{\overline{u}_b}{\sigma_u}$ Reciprocal of the relative near-bed turbulent intensity [-]

$\overline{u}_b$ Time averaged near-bed flow velocity [m s^{-1}]

σ_u Standard deviation of the flow velocity [m s^{-1}]

α_D Proportionality factor between the drag force / shear stress and the near bed velocity squared [-]

The same distribution holds for the distribution of $\tau_b = \alpha_D |u_b| u_b$, but then with an different value for α_D

Hofland and Battjes validated equation (2.37) using an experimental set-up. In a bed of stones with a nominal diameter of 30 mm, an artificial stone was placed (Figure 2.6). This cube with a side of 30 mm measures the pressure on both sides. The drag force is determined by subtracting the pressures.

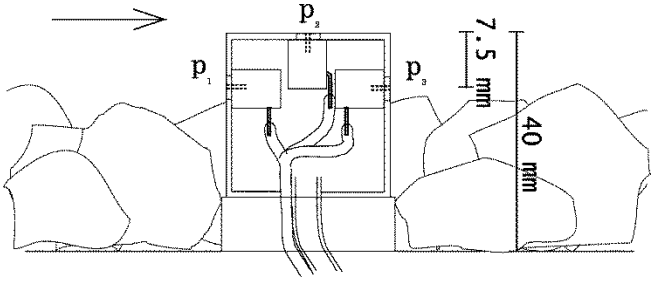

Figure 2.6: Measuring the pressures on a stone (Hofland and Battjes, 2006)

There were 4 experimental set-ups for the entrainment. The first set-up was a uniform open-channel flow (top picture of Figure 2.7). A second one was to evaluate the transition between a smooth bed and a rough bed (second picture of Figure 2.7). The last two experimental cases included a backward facing step. The difference is the placement of the step relative to the measuring stone. At the third

set-up the measuring stone was placed outside the recirculation zone (third picture of Figure 2.7) and at the last set-up at the reattachment point (Last picture of Figure 2.7)

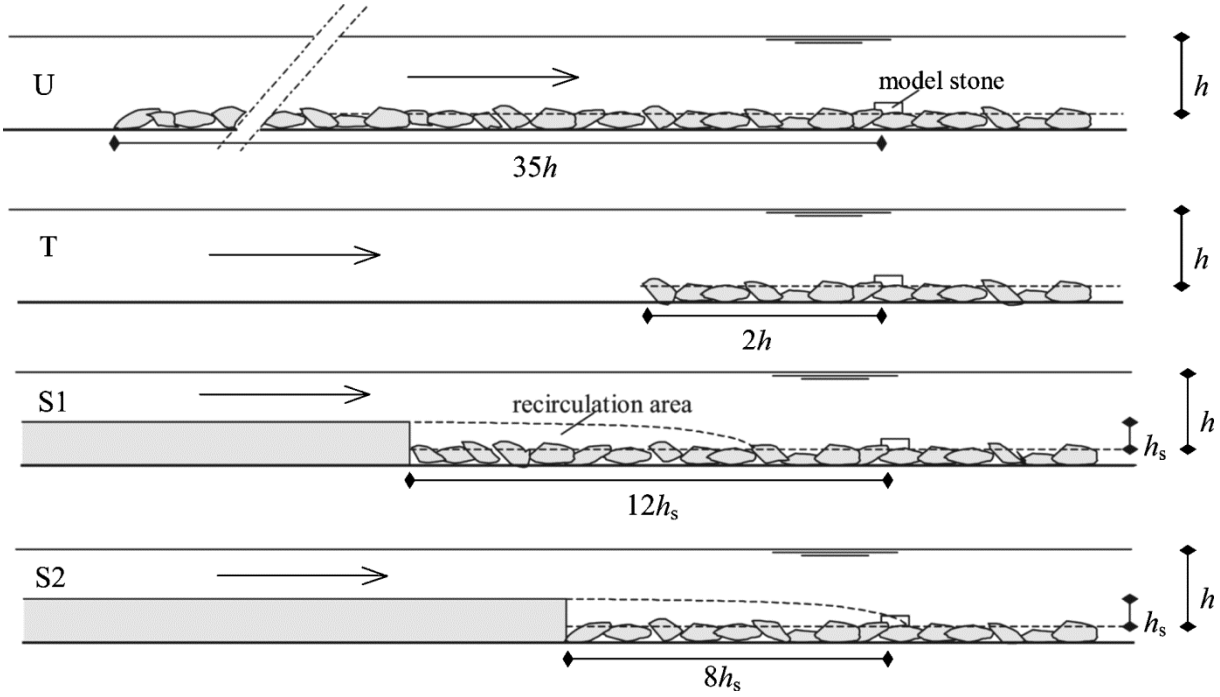

Figure 2.7: Multiple model set-ups for measuring the drag force distribution (Hofland and Battjes, 2006)

The skewness of the near-bed velocities was computed from the data produced by the measuring stone. The first two cases showed a negative skewed velocity distribution. The last two sheared a positive skewed velocity distribution. The positive skewness is coherent with the use of a lognormal distribution of Wu, Lin and Chou.

Equation (2.37) is calibrated with use of data of shear stresses on a smooth wall. This gave a value of 3.5 for δ .

Van Prooijen and Winterwerp rewrote equation (2.37). Assuming the shear stresses to be only positive. Only the shear stresses in the direction of the flow would cause entrainment. The α_D is replaced by a new scaled variable T_b, where α_D is already in included (Van Prooijen and Winterwerp, 2010).

$$P(T_b) = \frac{1}{2\sqrt{2\pi T_b}} \exp\left[-\frac{1}{2}\left(\sqrt{T_b} - \delta\right)^2\right] \tag{2.38}$$

$$T_b = \frac{\tau_b}{\rho_w o_u^2} = |\omega|\omega \tag{2.39}$$

$$\omega = \frac{u_b}{\sigma_u} \tag{2.40}$$

A correction factor (β_1) on the T_b has been introduced to mimic the ratio between the standard deviation and the mean value of the bed shear stresses. Another correction factor is needed to obtain the correct mean value (β_2)

Therefore

$$T_b^* = \beta_1 T_b - \beta_2 \delta^2 \tag{2.41}$$

Where

T_b^* Corrected scaled bed shear stress

β_1 Correction factor to fit the $\tau_b' / \overline{\tau}_b$ ratio of the measurements

β_2 Correction factor to fit the $\overline{\tau}_b$ value of the measurements

For β_1 and β_2 the values 1.75 and 0.83, respectively, are taken.

2.2 Methodology used in this thesis

In the previous sections different stochastic distributions have been used to describe the near-bed velocity. In this research a symmetric triangular distribution is used, because it is relatively easy to integrate this function analytically even if it is multiplied with the Van Rijn transport parameter.
The sediment transport formulation is based upon the Van Rijn 1993 formulation for a reference concentration and on the bed load transport formula of Van Rijn.

2.2.1 Probabilistic method for concentration

In the probabilistic calculation, the velocity is a stochastic variable with a mean and standard deviation. Figure 2.8 shows a triangular distribution for the near-bed velocities. The light gray area represents the probability an instantaneous velocity occurs ($P(u_i)\mathrm{d}u_i$). The dark gray area shows the velocities that contribute to the entrainment of sediment. The velocities have to be larger than a certain entrainment threshold for entrainment to occur. Figure 2.9 shows the Van Rijn transport parameter (T). This transport parameter is proportional to the instantaneous near-bed reference concentration ($c_{ref}(u_i)$). The transport parameter corresponding with the instantaneous velocity is shaded gray. When one multiplies the two, the concentration contribution of the specific instantaneous velocity of equation (2.42) is obtained (Kleinhans and Van Rijn, 2002, Hofland and Battjes, 2006, Van Prooijen and Winterwerp, 2010).

$$\mathrm{d}\tilde{c}_{ref} = P(u_i)\mathrm{d}u_i \cdot c_{ref}(u_i) \tag{2.42}$$

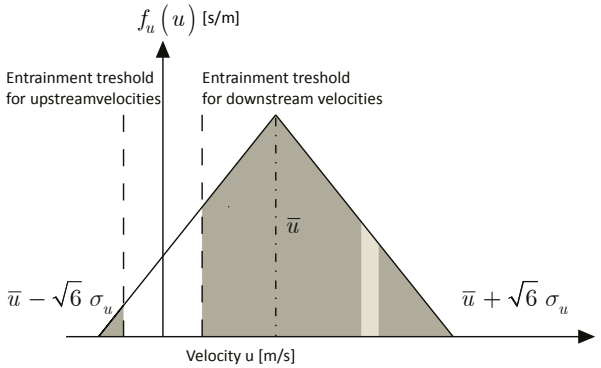

Figure 2.8: Instantaneous near-bed velocity.

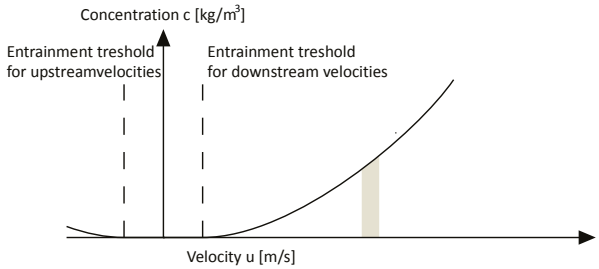

Figure 2.9: Van Rijn transport parameter for the instantaneous velocity.

When the intervals are chosen infinitely small and all these intervals are summed, the total concentration is calculated. There is only entrainment when the velocities are larger than the critical velocity needed for entrainment. Therefore, only the concentrations corresponding with these velocities are taken into account. The integral of the velocity times the concentration is evaluated from the critical velocity to infinity. Also the negative velocities are taken into account therefore the integral also has to be evaluated from minus infinity to minus the critical velocity. Equation (2.43) shows the result.

$$\tilde{c}_{ref} = \int_{ucr}^{\infty} P(u_i)\,\mathrm{d}u_i \cdot c_{ref}(u_i) + \int_{-\infty}^{-ucr} P(u_i)\,\mathrm{d}u_i \cdot c_{ref}(u_i) \tag{2.43}$$

For a deterministic case, the standard deviation is zero. The probability density function is in that case a Dirac-delta function around the mean of the distribution. The Dirac-delta-function has a zero width, an infinite height. It is still a probability density function; therefore the area is equal to 1. If this function is multiplied with the instantaneous Van Rijn transport parameter the same value is obtained for the time-average concentration.

The probabilistic approach has a few advantages over the deterministic approach. For the deterministic approach there is no entrainment when the velocity is zero. When the probabilistic approach is used, there is entrainment when the water is stagnant, but there is turbulence. A practical example of this is a reattachment point.

2.2.2 The triangular distribution

In section 2.1.3 a normal, lognormal and a chi squared distribution have used as a distribution of the near-bed velocity. When these distributions are multiplied with the expression for the near-bed reference concentration, this leads to an analytical non-integratable function. Such an expression could be integrated numerically. When this numerical integration is used as a sediment transport function, this numerical integration has to be performed at every grid cell, for every time step. This is very time-consuming. A triangular distribution multiplied with the Van Rijn T-parameter can integrated, because the triangular distribution consists of two linear parts.

A triangular distribution includes the turbulent fluctuations of the flow on the sediment transport. There are many researchers that have used a normal distribution as a description of the near bed velocities. In the range around the average value, the triangular distribution has similar properties. Figure 2.10 shows both the normal and the triangular distribution. The differences between the outcome of the triangular distribution and normal distribution are small (Appendix B.3).

The PDF of the triangular distribution is: (see derivation in Appendix B.1)

$$f_u = \frac{\sigma_u}{\sqrt{6}} - \frac{|u - \overline{u}|}{6\,\sigma_u} \tag{2.44}$$

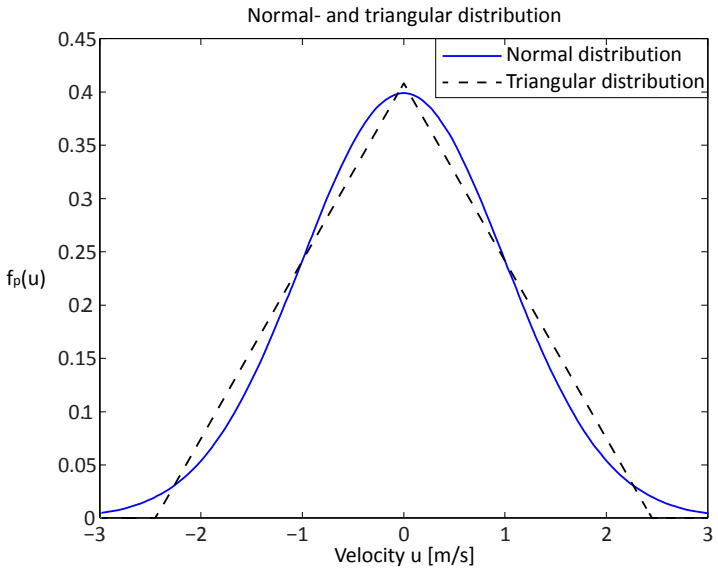

Figure 2.10: Normal and triangular distribution with a zero mean and a standard deviation of 1

The triangular distribution assumes no velocities larger than $\mu + \sqrt{6}\,\sigma$ in contrast to the normal distribution where every velocity has a chance of occurring.

Mean value of the velocity

The velocity halfway the lowest computational layer ($u_{k\max}$) is calculated in Delft3D. The bed shear velocity (u_*) is defined at the roughness height. It is calculated using a logarithmic velocity profile from halfway the lowest computational layer to the roughness height. Equation (2.45) describes this computation and it has been implemented in Delft3D (Deltares, 2010). Appendix A.5 gives a derivation of this formula.

$$u_* = u_{\mathrm{kmax}}\,\kappa \Big/ \ln\left(1 + \frac{\Delta z_b}{z_0}\right) \tag{2.45}$$

where:

u_{kmax} Velocity in the lowest computational layer [m s^{-1}]

u_* Bed shear velocity [m s^{-1}]

κ Von Karman coefficient (range 0.40 – 4.1) (Deltares, 2010) [-]

Δz_b Thickness of the bed layer [m]

z_0 Bed roughness length [m]

Standard deviation of the velocity

The turbulent kinetic energy (TKE) is defined by equation (2.46):

$$k = \frac{1}{2}\left(\overline{(u')^2} + \overline{(v')^2} + \overline{(w')^2}\right) \tag{2.46}$$

u', v' and w' are the perturbations of the time-averaged velocities. The mean squared perturbations are equal to the standard deviation of the flow. When the flow is assumed isotropic, the relation between the standard deviation and the TKE is, expressed by equation (2.47) with $\alpha_u = 1$.

$$\sigma_u = \alpha_u \sqrt{\tfrac{2}{3} k} \tag{2.47}$$

where

σ_u Standard deviation of the flow velocities in the bottom computational layer [m s^{-1}]

α_u An-isotropy parameter for the turbulent kinetic energy [-]

k Turbulent kinetic energy [m^2 s^{-2}]

The horizontal length scales of a river in most cases larger than the vertical. If the an-isotropy is taken into account, the an-isotropy parameter will be larger than 1. The topography of the Eminnence pool is calculated using isotropic conditions. In the results in section 4.3.2 also a sensitivity analysis is performed, which modifies the an-isotropy parameter.
In Delft3D the turbulent kinetic energy is calculated using the k-*ε* model. This model is described in appendix A.4

2.2.3 Van Rijn transport parameter

In the Van Rijn 1993 formulation for suspended sediment the only parameter, which includes the velocity is the transport parameter of equation (2.48). In the Van Rijn 1993 bed load formulation the T-parameter is multiplied with the velocity.

$$T = \frac{\mu_c \left(u_*\right)^2 - \left(u_{*,cr}\right)^2}{\left(u_{*,cr}\right)^2} \tag{2.48}$$

The critical shear stress velocity ($u_{*,cr}$) is calculated, using the Shields formula explained in section 2.1.2.
When the T-parameter is larger than zero, there is entrainment. Equation (2.49) shows the criterion for u for which the transport parameter is larger than zero.

$$T > 0 \text{ for } u > \frac{u_{*,cr}}{\sqrt{\mu_c}} \tag{2.49}$$

The corrected critical velocity for entrainment is:

$$u'_{cr} = 2\frac{u_{*,cr}}{\sqrt{\mu_c}} \tag{2.50}$$

In equation (2.50) the factor 2 is used for the difference in entrainment between the instantaneous velocities and the time-averaged velocities. De Ruiter showed that the critical shear stress velocity for instantaneous forcing is higher than for time-averaged forcing. (De Ruiter, 1982)

Figure 2.11 shows the triangular distribution in blue. The axis on the left shows the corresponding values. The red line is the Van Rijn transport parameter. The black line is the transport parameter to the power 1.5 times the triangular distribution. The black dashed lines are the corrected critical

velocity for positive and negative velocities. The probabilistic value for $T^{1.5}$ is found, when one would integrate from the start of the triangular distribution to the left vertical line and add the integration from the second vertical line to the end of the triangular distribution.

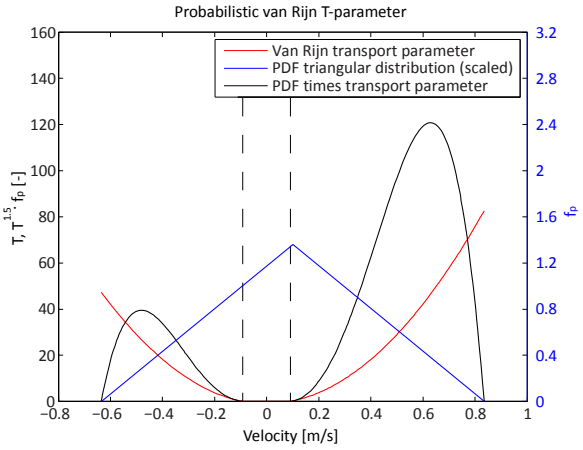

Figure 2.11: Example of probabilistic Van Rijn T-parameter

2.2.4 Suspended sediment transport

The Van Rijn (1993) formula for the suspended reference concentration is:

$$c_{ref} = 0.015 \rho_s \frac{D_{50}}{a} \frac{T^{1.5}}{D_*^{0.3}} \tag{2.51}$$

In this formulation the Van Rijn transport parameter can be expressed using the probabilistic approach

$$\tilde{c}_{ref} = 0.015\ \alpha_{sus}\ \rho_s \frac{D_{50}}{a\ D_*^{0.3}} \left(\int_{ucr'}^{\mu+\sqrt{6}\,\sigma} T\left(u_i\right)^{1.5} \cdot P\left(u_i\right) \mathrm{d}u_i + \int_{\mu-\sqrt{6}\,\sigma}^{-ucr'} T\left(u_i\right)^{1.5} \cdot P\left(u_i\right) \mathrm{d}u \right) \tag{2.52}$$

When the triangular distribution is applied, the upper and lower bound can be changed to $\overline{u} + \sqrt{6}\ \sigma_u$ and $\overline{u} - \sqrt{6}\ \sigma_u$ respectively. Appendix B shows the method of solving this integral. The solution of this integral is presented in Appendix B.2

2.2.5 Bed load transport

The Van Rijn formula for bed load transport reads: (Lesser et al., 2004)

$$S_b = 0.5\ \rho_s\ D_{50}\ u_*\ \sqrt{\mu_c}\ D_*^{-0.3}\ T \tag{2.53}$$

The same method as in the previous section can be used to obtain the probabilistic bed load transport. Equation (2.54) shows the integral to be solved. The solution is obtained in appendix B.2

$$S_b = 0.5\ \alpha_{bed}\ \rho_s\ D_{50}\ D_*^{-0.3} \left(\int_{ucr'}^{\mu+\sqrt{6}\,\sigma} \sqrt{\mu_c}\ u_i\ T\left(u_i\right)\ P\left(u_i\right) \mathrm{d}u_i + \int_{\mu-\sqrt{6}\,\sigma}^{-ucr'} \sqrt{\mu_c}\ u_i\ T\left(u_i\right)\ P\left(u_i\right) \mathrm{d}u \right) \tag{2.54}$$

2.3 Results

2.3.1 Calibration: trench migration experiment

To see whether the sediment transport formula proposed in this thesis, Van Rijn including turbulence (Van Rijn i.t.), predicts the correct order of magnitude of the near-bed concentration and the bed-load transport, first a 2 dimensional vertical model is used. Table 2.1 shows the main input parameters of this model. Because of the simplicity of the model, the impact of the sediment transport formula is simple to explain. Another advantage is that the parameters can be easily calibrated.

The model used for this, is a Delft3D model of a flume experiment carried out by Van Rijn. In the flume an alluvial layer is present. In this layer a deeper part, trench, is situated. The experiment and simulation show a migration of the trench along with the flow and a shallowing of the trench. In Figure 2.12 the lower line is the bed, including the trench. The upper line is the water level. A small increase in water is present at the trench.

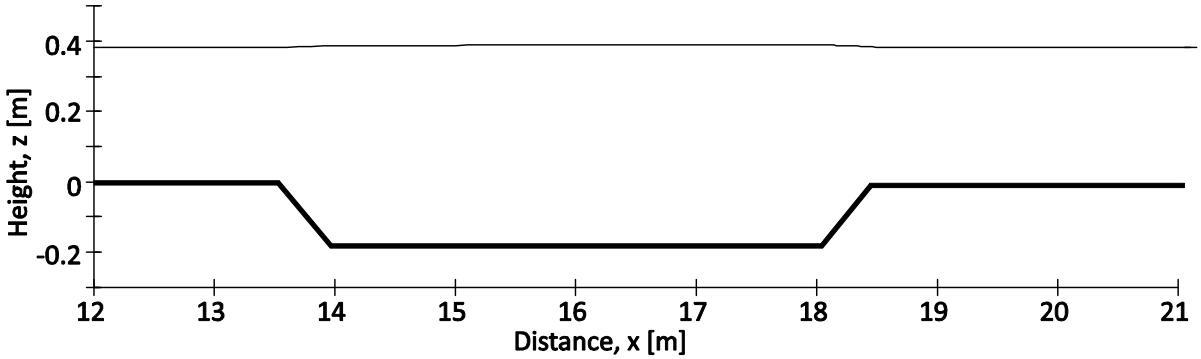

Figure 2.12: Bottom and water level of a longitudinal cross-section of the trench migration experiment based upon (Lesser et al., 2004)

Table 2.1: Input parameters for the model of the trench migration experiment

Variable	Value
Computational time	15 hours
Morfac	1
Simulated time	15 hours
Time step	0.004
Spin-up interval	5 minutes
Domain length	30 metre
Domain Width	0.5 metre
Depth	0.4 metre
D_{50}	140 μm
Roughness White Colebrook (k_s)	0.025 metre
z_0 equivalent	$z_0 = k_s / 30 = 8.33 \cdot 10^{-4}$ m
Inflow boundary	Discharge per cell: $1.989 \cdot 10^{-2}$ m^3 s^{-1}
Total discharge equivalent	$1.989 \cdot 10^{-2} \cdot 5 = 9.945 \cdot 10^{-2}$ m^3 s^{-1}
Outflow boundary	Water level 0.4 metre
Sediment inflow	0 kg s^{-1}
α_{sus}	0.54
α_{bed}	0.35
Aksfac	0.5
Bed slope effect	None

Figure 2.13 shows the computed velocities in the bottom layer at the start of the morphologic computation. The dashed line corresponds with the location of the trench. Because of the deepening, the velocities decrease. After the decrease in velocity the velocities increase again, with a peak at the end of the trench.

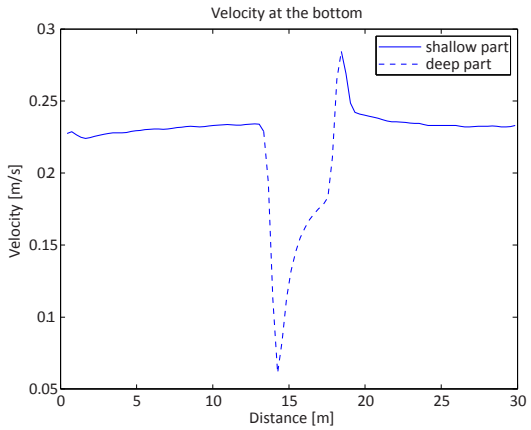

Figure 2.13: velocities at the bottom at the start of the morphologic computation

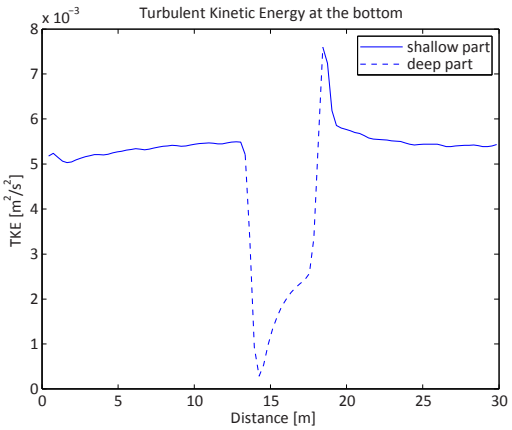

Figure 2.14: Turbulent kinetic energy at the bottom at the start of the morphologic computation

The turbulence increases in the middle of the trench as seen in Figure 2.14. At the entrance of the trench and the end of the trench a peak in turbulence is seen. This can be explained due to the sudden change in topography.

The near-bed concentration and the bed load transport of Van Rijn i.t. show the same three notable differences with Van Rijn 1993. The first difference is the peak at the end of the trench (around 18 metre). This peak is larger for Van Rijn 1993, where one would expect the peak would be larger for Van Rijn i.t., due to the increased turbulence. The explanation lies in the ripple factor (μ_c). For a higher water level the ripple factor is higher and therefore the entrainment is higher. The ripple factor has a less effect on Van Rijn i.t.. This becomes visible when the concentration against different water heights is plotted (Figure 2.17).

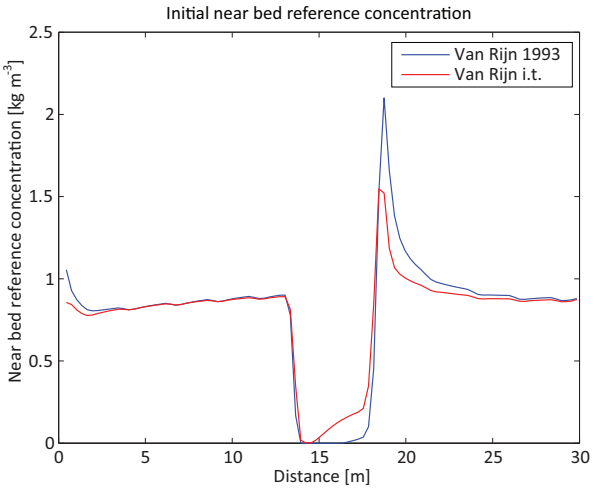

Figure 2.15: Near-bed concentration at the start of the morphologic computation

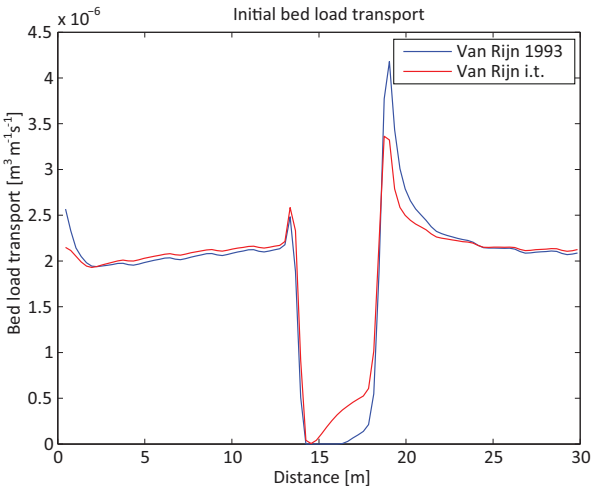

Figure 2.16: Bed load transport at the start of the morphologic computation

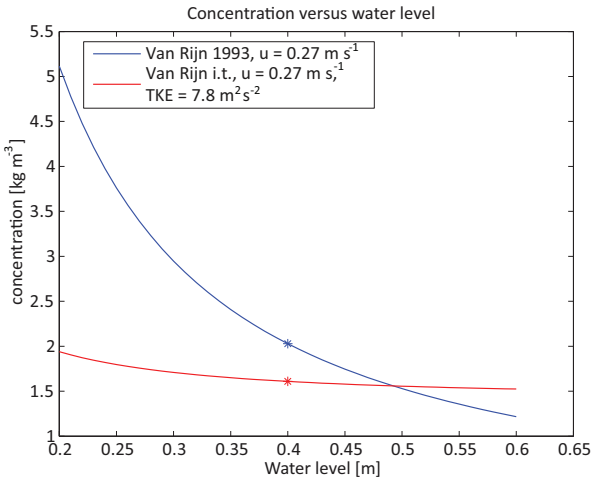

Figure 2.17: Near-bed concentration for different water heights

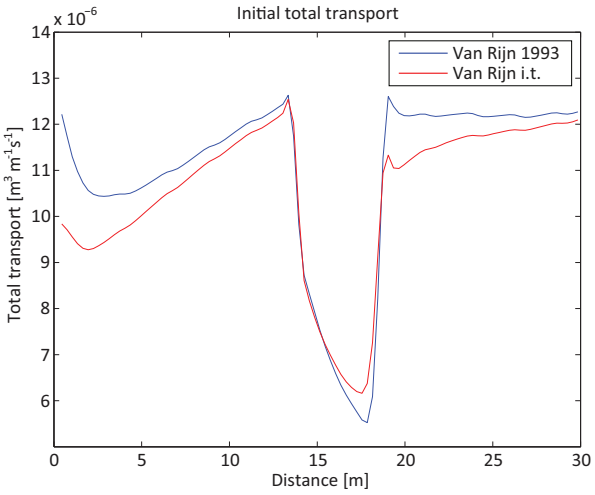

Figure 2.18: Total transport at the start of the morphologic computation

The second difference is that Van Rijn i.t. computes a higher concentration in the trench, whereas Van Rijn 1993 computes no concentration at this spot. The turbulent velocities are used in Van Rijn i.t. and therefore some of the instantaneous velocities are higher than the entrainment threshold.
The last difference is at the inflow boundary. Van Rijn 1993 computes higher concentrations and transports than Van Rijn i.t.. The water level variation at this location has a larger influence on Van Rijn 1993 than on Van Rijn i.t.

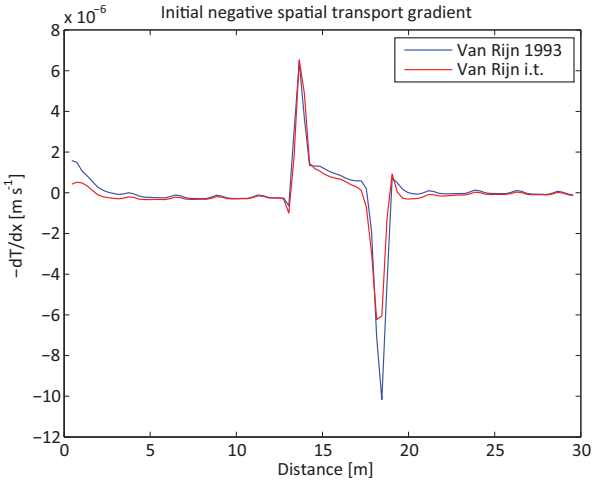

Figure 2.19: Spatial transport gradient at the start of the morphologic computation

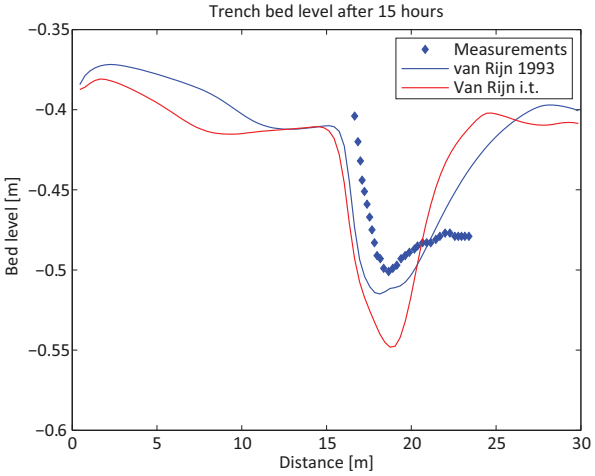

Figure 2.20: Bed level at the end of the simulations comparing to measurements

Figure 2.19 shows the negative spatial transport gradient, as used in the Exner equation (2.9), at the beginning of the morphologic computation. The peak at the entrance of the trench indicates that sedimentation will occur at this spot. At the end of the trench erosion will occur. Van Rijn 1993 computes more erosion at this location. The velocities will decrease more for the Van Rijn 1993 formulation than for Van Rijn i.t.. Van Rijn 1993 computes more erosion at the end of the trench. More erosion holds a lower bed level. This will result into lower velocities and thus less erosion when the trench has propagated a bit further. The computed bed level of Van Rijn 1993 will therefore become less steep than the bed level of Van Rijn i.t. (Figure 2.20).

Van Rijn i.t. is calibrated to match the initial near-bed reference concentration and bed load transport of Van Rijn 1993. The final result in bed level is comparable with Van Rijn 1993. However, Van Rijn 1993 shows a better correlation with the measurements. For this particular case Van Rijn i.t. does not show an improvement. In this case the turbulent velocity fluctuations do not have a large influence on the bed and thus on the morphology.

2.3.2 Validation: shear flow

The shear flow model is a 3 km long model of which the first 990 metres are separated in the middle by a thin dam. When one implements a thin dam in Delft3D, this acts as an infinite high wall. The wall has a zero thickness. When looking in the direction of the flow, the left side has a flow velocity of 2.5 m/s, the right side 0.5 m/s. Table 2.2 shows the rest of the main input parameters. Figure 2.21 shows the initial velocity at the lowest computational layer. It shows the magnitude and direction a couple of ten metres before and after the thin dam. The white line represents the thin dam. The flow pattern at the right side of the thin dam shows two instable eddies at the two upper dark blue parts. In Figure 2.22 the turbulent kinetic energy has been plotted. A spot of increased turbulence is visible at the middle of the channel. This spot move back and forth at the tip of the thin dam.

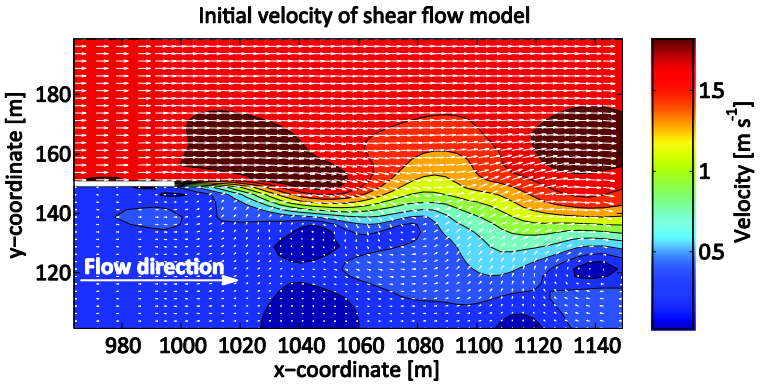

Figure 2.21: Initial velocity at the bed for the shear flow model

Table 2.2: Model parameters for the model of a shear flow

Variable	Value
Computational time	24 hours
Morfac	1
Simulated time	24 hours
Time step	6 seconds
Spin-up interval	4 hours from initial condition file
Domain length	3000 metre
Domain With	100 metre
Depth	5 metre
D_{50}	140 μm
Roughness Chézy	65
Inflow boundary above	Velocity 2.5 m/s
Inflow boundary below	Velocity 0.5 m/s
Outflow boundary	Water height 5 metre
Sediment inflow	0 kg s^{-1}
α_{sus}	2 · 0.54 = 1.08
α_{bed}	2 · 0.35 = 0.7
Aksfac	1
Bed slope effect	None

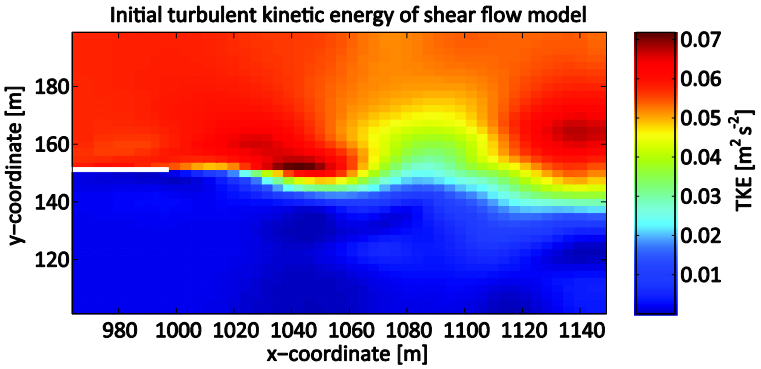

Figure 2.22: Initial turbulent kinetic energy at the bed for the shear flow model.

Figure 2.23 shows the reference concentration for Van Rijn 1993 at the start of the morphodynamic computation. Figure 2.24 shows the reference concentration for Van Rijn i.t.. The reference concentration for Van Rijn i.t. is a factor of two less than Van Rijn 1993. A similar, however to a lesser extent, is visible for the bed-load transport. Figure 2.25 shows the bed load for Van Rijn 1993 and Figure 2.26 for Van Rijn i.t.. In this computation the calibration parameters of the Van Rijn i.t. formulation (α_{sus}, α_{bed}) are twice as high as for the trench migration experiment. Yet, the concentration and bed load transport are still under-predicted.

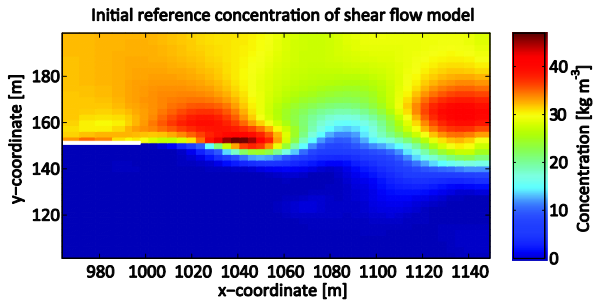

Figure 2.23: Initial reference concentration for Van Rijn 1993

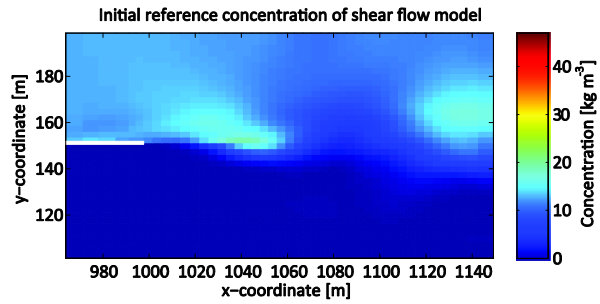

Figure 2.24 Initial reference concentration for Van Rijn including turbulence

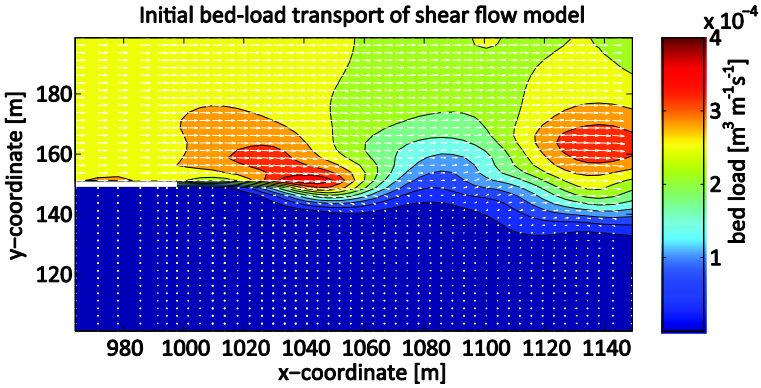

Figure 2.25: Initial bed load for Van Rijn 1993

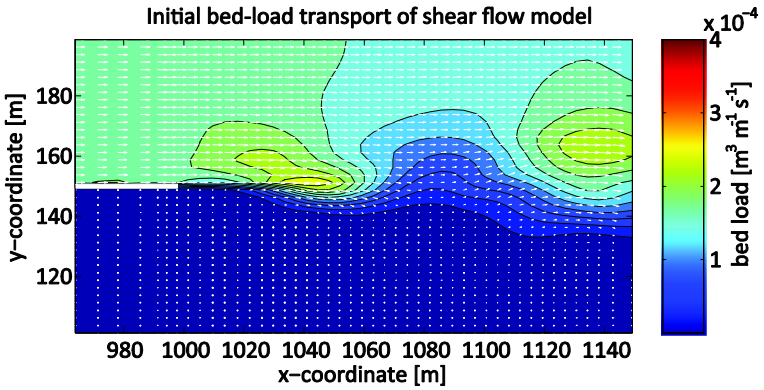

Figure 2.26: Initial bed load for Van Rijn including turbulence

The negative time-averaged transport gradients give a clearer view of the sedimentation or erosion. Figure 2.27 shows the difference in the time-averaged suspended transport gradient for Van Rijn 1993 and Van Rijn i.t.. Figure 2.28 shows the same for the bed-load transport. The negative values in blue present a case where the negative transport gradient for Van Rijn i.t. is smaller than for Van Rijn 1993. The dark blue areas near the tip of the thin dam indicate an higher erosion for Van Rijn i.t. than for Van Rijn 1993. The turquoise areas indicate a spot where Van Rijn i.t. computes less deposition than Van Rijn 1993. Both figures show blue spots right after the tip of the sheet. This means that here is more erosion for the Van Rijn including turbulence formulation. The effect is visible in the final topography computed with Van Rijn 1993 (left of Figure 2.29) compared to Van Rijn i.t. (right of Figure 2.29). Figure 2.30 shows a cross-section from the tip of the thin dam in stream-wise direction at the left side of the thin dam. Even though the average transport computed by Van Rijn i.t. is smaller than computed by Van Rijn 1993, the erosion at the tip of the thin wall is higher. This is even better visible when one would look a cross-section one grid-cell to the left side of the dam (Figure 2.31). At the right side of the thin dam (Figure 2.32), the erosion just behind the tip is also significantly higher for Van Rijn i.t..

The conclusion drawn from this model study is that Van Rijn i.t. shows more erosion at places where high turbulent velocity fluctuations are present, even when the average transport computed by Van Rijn i.t. is less than computed by Van Rijn 1993.

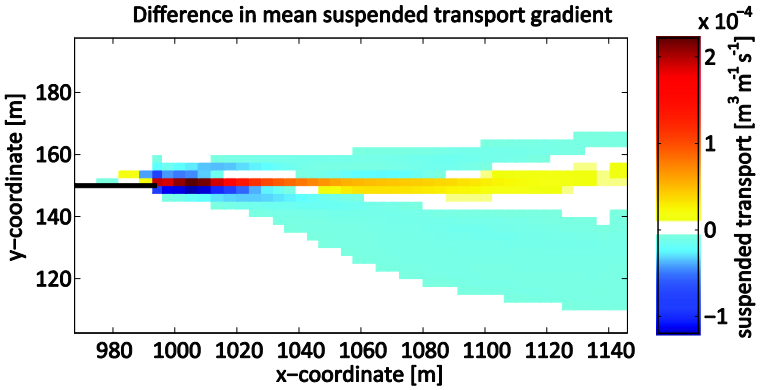

Figure 2.27: Difference in mean suspended transport gradient of Van Rijn 1993 and Van Rijn including turbulence

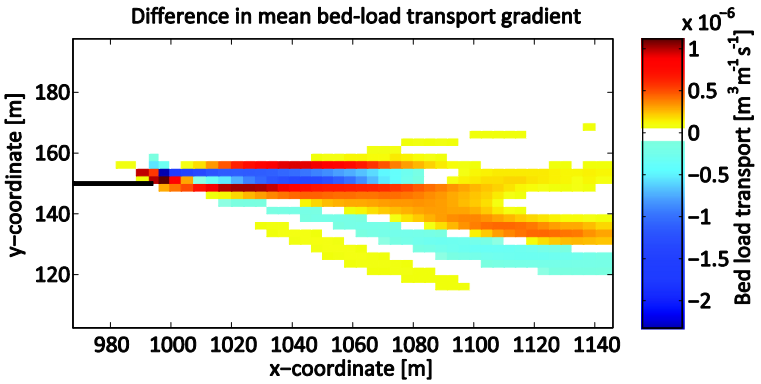

Figure 2.28: Difference in mean bed load transport gradient of Van Rijn 1993 and Van Rijn including turbulence

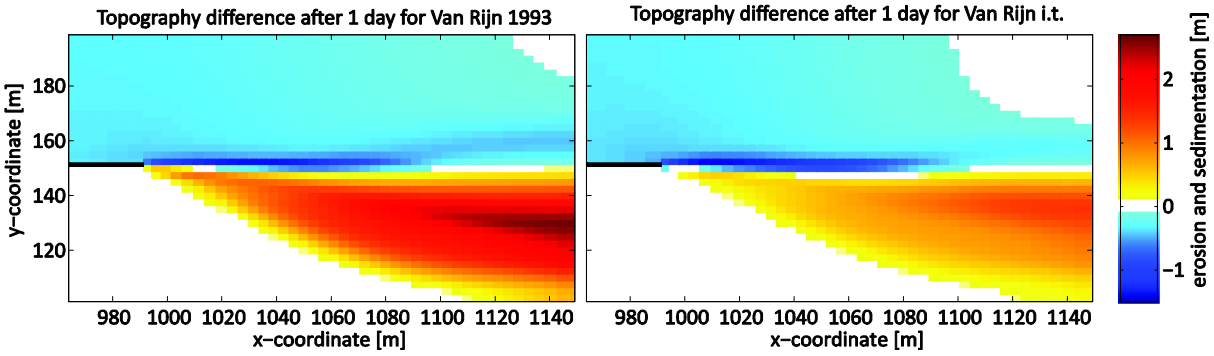

Figure 2.29: cumulative erosion and sedimentation after 1 day for Van Rijn 1993 (left) and Van Rijn i.t. (right)

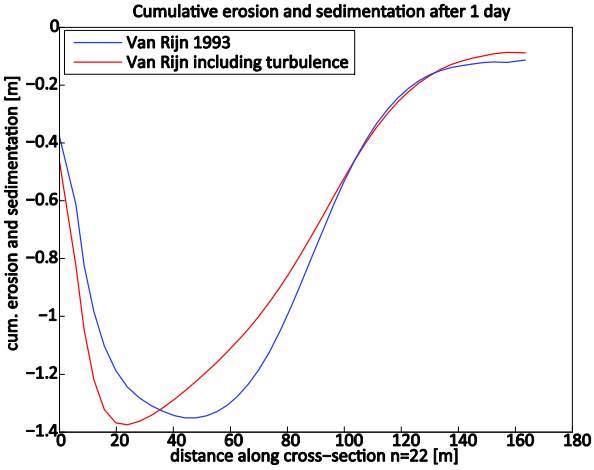

Figure 2.30: Cumulative erosion and sedimentation at the first row to the left of the tip of the sheet for Van Rijn in- and excluding turbulence

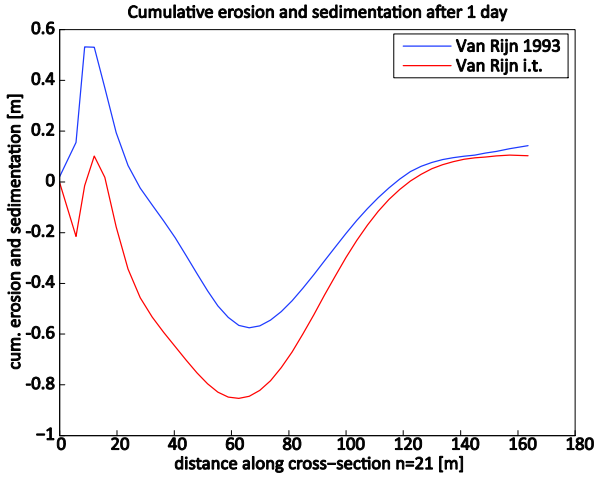

Figure 2.31: Cumulative erosion and sedimentation at the second row to the left of the tip of the sheet for Van Rijn in- and excluding turbulence

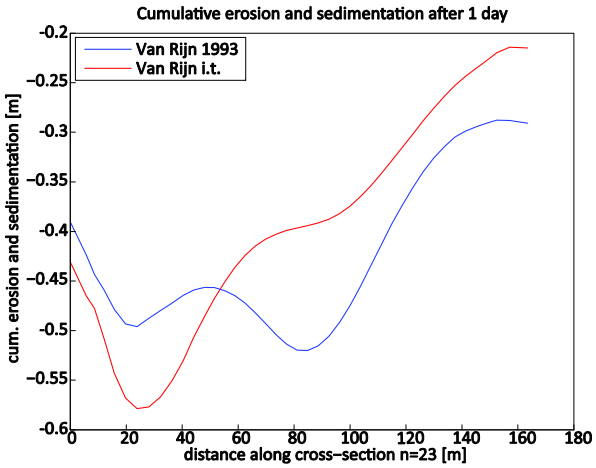

Figure 2.32: Cumulative erosion and sedimentation at the first row to the right of the tip of the sheet for Van Rijn in- and excluding turbulence

3 Development of a formulation for steep slopes

Three important failure processes play a role when considering the stability of sub-aqueous sandy slopes. The most well-known failure is macro instability or shear slope failure. This occurs when a slope is too steep with respect to the shear strength of the soil. A large mass of soil at a slope then starts to slide. A second process is liquefaction flow slide, where a layer of loosely packed sand becomes a liquid and starts flowing. The third process is a breach flow slide, where sand is eroded by a turbidity current in combination with breaching. This process is known from dredging deep sand pits. When the slope is steeper than the angle of repose a grain flow develops. This is a laminar flow caused by the rolling of sediment down the slope.

3.1 State of the art

3.1.1 Macro instability

Slopes can fail by sliding. A huge part of the slope will then slide down along a slide plane (see Figure 3.1).

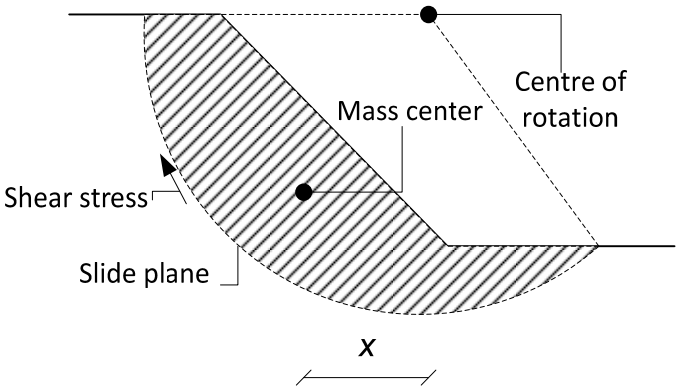

Figure 3.1: Slope failure along a circular slide plane according to Bishop's method

Figure 3.1 shows the sliding of a slope according to Bishop. The method assumes a circular slide plane. The driving mechanism of the sliding is the moment caused by the weight of sliding area around the centre of rotation (indicated by *x*). If one would compute this numerically, the mass is divided into different vertical bars with a width Δx_i and height h_i, where i is the number of the bar.

$$M_D = \sum_{i=1}^{n} \gamma_i \cdot h_i \cdot \Delta x_i \cdot x \tag{3.1}$$

Where

γ_i Weight of the soil of slice i [N m^{-3}]

x Horizontal distance from the centre of the slice i to the centre of the slip circle [m]

This is counteracted by the resisting moment, caused by the shear stresses along the slide plane multiplied with the radius of the slide plane.

$$M_R = R \sum_{i=1}^{n} \tau_{S,i} \cdot L_i \tag{3.2}$$

Where:

R Radius of the slip circle [m]

$\tau_{S,i}$ Shear stress at the bottom of the slice of the slip circle [N m^{-2}]

L_i Length of the arc at the bottom of slice i [m]

This calculation is performed for many slide planes with corresponding centres of rotation. The slide plane where the driving moment (M_D) is larger than resisting moment (M_R) is the plane where the soil could fail. In the software, D-Geo-Stability, it is possible to calculate the possible slide plane for a slope.

3.1.2 Liquefaction

The freshly deposited sediment on the banks of the sandbars at the Colorado River is loosely packed When sediment on a slope is loosely packed (see left side of Figure 3.2) the flow induced shear stress can induce contractant behaviour. The sediment will be more densely packed afterwards. The volume between the grains is filled with water (represented by the darker gray in Figure 3.2). After the contraction this volume is less, therefore water has to flow out of the pores (see right side of Figure 3.2). An increase in water pressure (see middle of Figure 3.2) can occur when the outflow of water lags behind the displacement. This results into reduced grain stresses. When the grain stresses are nearly zero liquefaction occurs.

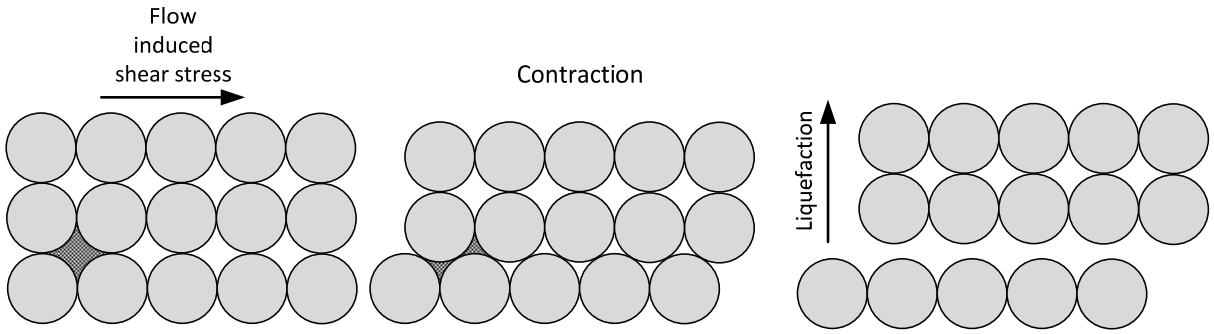

Figure 3.2: Contractant behaviour of sand particles and liquefaction

3.1.3 Breaching process and turbidity currents

On a sandy slope of about 1:5 to 1:3 a small disturbance can cause the slope to fail. When a small part of the slope is steeper than the critical angle of repose due to some local disturbance, this small slope may propagate uphill, this is called the breaching effect (see Figure 3.3) This breach is then a moving boundary providing sediment for a turbidity current (Mastbergen and Van Den Berg, 2003).
Due to the velocity and shear stress imposed by this current even more grains are eroded and the density of the current increases. The turbidity current will develop more speed when propagating further down the slope. A gradient in velocity and thus a gradient in sediment pick up over the slope may develop. This could even make the slope steeper than the original slope (breach flow slide).

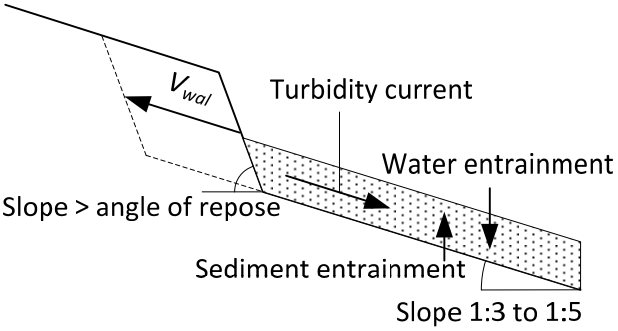

Figure 3.3: Breaching as a sediment supply for the turbidity current. Based upon (Mastbergen and Van Den Berg, 2003)

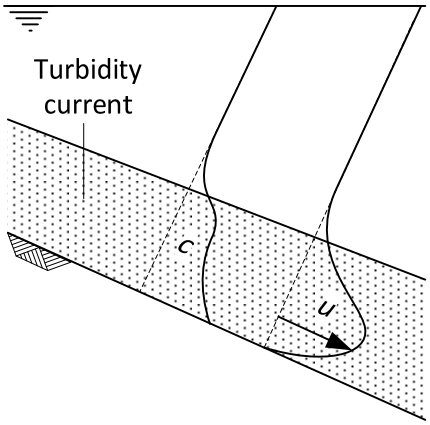

Figure 3.4: Velocity and concentration profile in the turbidity current

A series of studies has been performed toward the breaching process of underwater slopes. The result was a model called HM Breach. This is a 1D stationary model with an extension toward a 2D approach in which the width of the slope is taken into account. The model is based upon the continuity equations of water and sediment. Further, the momentum of the mixture flow is considered. With the flow equations the erosion of the bed is calculated (Mastbergen, 2009, Mastbergen and Van Den Berg, 2003).

The turbidity current can be represented 3 dimensionally and extended for unsteady flow. The momentum equations are then represented by the Navier-Stokes equations. There is a gradient in the concentration and in the velocity profile in vertical direction. Parallel to the slope the current changes due to the entrainment of sediment and water. Transverse to the slope fanning plays a role. This is the widening of the turbidity current as it propagates down slope. Due to the widening the roller in front of the turbidity current is stretched. The angular momentum is conserved and the roller is shortened, therefore the roller starts rolling faster. The current will entrain more water, which makes the turbidity current higher. Ultimately the current will dissolve, because the height was stretched too much. These processes cannot be computed in detail in Delft3D or HM Breach.

3.2 Methodology used in this thesis

In this study three ways of slope slumping are examined. The first two are simulating avalanching. The methods will prohibit sand to be deposited on a steep slope. The third will simulate a slope slump by changing a steep slope to the equilibrium slope. For calculating the slope, the depth of the cell which is evaluate, is used, as well as the depth of the cells that lie uphill in x and y direction. The full method is explained in appendix C.1.

3.2.1 Avalanching via suspended transport

When a modelled slope becomes as steep as the angle of repose, any new deposited sediment will trigger an avalanche and thus flow away immediately. The angle is dependent on the packing of the sediment, but for this formulation a fixed value of 32 degrees is taken. The avalanche can be modelled as if the sediment that is about to be deposited, has to stay in suspension. To do this, the sedimentation term in the sedimentation-erosion formulation has to be set to zero on a steep slope. The sedimentation or deposition term is represented by equation (3.3). This equation is derived in appendix A.6.

$$D = w_s c_{kmx(bot)} \approx \alpha_1 w_s c_{kmx} \tag{3.3}$$

In equation (3.3) the sedimentation is calculated by multiplying the particle fall velocity with a concentration (c_{kmx}) and a calibration factor (α_1). When this calibration factor is set to zero, no sedimentation will take place.

The erosion term of equation (3.4) will not be affected by setting α_1 to zero.

$$E \approx -\alpha_2 \varepsilon_s \frac{c_{kmx} - c_{ref}}{\Delta z} \tag{3.4}$$

The sediment that cannot be deposited will be transported in the direction of the suspended load at the bottom. One downside to this method is that there has to be erosion for this method to work. When the critical shear stress needed for erosion is not exceeded, this formulation will have no effect. The physical reasoning to justify this is as following: the flow will decrease the strength of a slope; therefore the chance that a slope fails in stagnant water is less than when the velocities are high. However, a really steep slope will always slump, whether there is a flow or not.

3.2.2 Avalanching via bed-load transport

At a slope larger than 32 degrees, the sand cannot be deposited on the slope. Instead of holding the sediment in suspension, it can also be transported as bed load. The advantage of bed load transport over suspended transport is that bed load can be influenced by the bed slope. This means that the sediment gets transported partially in the flow direction, but also down-slope. In section 2.1.2 the direction of the bed load according to Koch and Flokstra has been described.

Equation (3.5) shows the deposition term in metres per second. Equation (3.6) shows the bed load transport due to the slumping in x-direction. It is the sedimentation term multiplied with the density of the sediment and the area of the grid cell, to get the mass change per time unit. Then it is divided by the distance over which it should be transported and multiplied with the relative velocity in x or y direction. Equation (3.6) and (3.7) show the bed load in x and y direction.

$$D = w_s c_{kmx(bot)} \tag{3.5}$$

$$S_{slump,u} = \rho_s \frac{A_{grid}}{\Delta x} \frac{u}{\|\mathbf{u}\|} D \tag{3.6}$$

$$S_{slump,v} = \rho_s \frac{A_{grid}}{\Delta y} \frac{v}{\|\mathbf{u}\|} D \tag{3.7}$$

where:

$S_{slump,u}$	Bed load in x-direction due to slumping before update for bed-slope effect [kg m^{-1} s^{-1}]
$S_{slump,v}$	Bed load in y-direction due to slumping before update for bed-slope effect [kg m^{-1} s^{-1}]
ρ_s	Density of the sediment [kg m^{-3}]
A_{grid}	Area of the grid cell [m^2]
Δx , Δy	grid size in x and y direction [m]
u , v	Velocity in x and y direction [m s^{-1}]

$\|\mathbf{u}\|$ Total velocity magnitude [m s^{-1}]

D Sediment deposition [m s^{-1}]

Delft3D uses the approximation that the grid cells are orthogonal. In this case it would hold that the area of the grid cell can be expressed as the width times the length. Substituting equation (3.8) and (3.5) into equation (3.6) and (3.7), the slump-transport of equation (3.9) and (3.10) are obtained.

$$A_{grid} = \Delta x \, \Delta y \tag{3.8}$$

$$S_{slump,u} = \rho_s \; \Delta y \frac{u}{\|\mathbf{u}\|} w_s \, c_{kmx(bot)} \tag{3.9}$$

$$S_{slump,v} = \rho_s \; \Delta x \frac{v}{\|\mathbf{u}\|} w_s \, c_{kmx(bot)} \tag{3.10}$$

After this process the bed load is corrected for slope effects, by the formulation of Koch and Flokstra as described in section 2.1.2.

3.2.3 Steep slope changed to equilibrium slope

The last slope process is a slope slump. When a slope is too steep it is changed to the equilibrium slope. The sediment that has to move, to change to the equilibrium slope, is then deposited in the adjacent cells. The new depth of the cell is calculated to match the slope angle with equation(C.8) from appendix C.1. An equilibrium slope of 25 degrees is used in the computations.

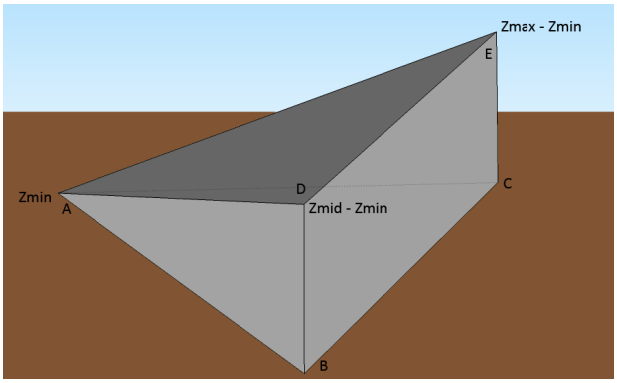

Figure 3.5: Volume of a slope defined by three depth points

The volume of the slope before slumping is calculated with two pyramids. The first is ABCD (in Figure 3.5). This is the first part of equation (3.11). The second pyramid is ACDE (in Figure 3.5). This is represented by the second part of equation (3.11).

The volume after the slope is slumped and changed to its equilibrium profile is calculated the same way, but now with the new depth. (see equation (3.12)). The difference is the volume that has to be transported is:

$$V_{ini} = \frac{1}{3} A_T \left(z_{\text{mid}} - z_{\text{min}} \right) + \frac{1}{3} A_T \left(z_{\text{max}} - z_{\text{min}} \right) \tag{3.11}$$

$$V_{end} = \frac{1}{3} A_T \left(z_{\text{mid}} - z_{\text{min}} \right) + \frac{1}{3} A_T \left(z_{\text{max,new}} - z_{\text{min}} \right) \tag{3.12}$$

$$V_{slump} = V_{ini} - V_{end} = \frac{1}{3} A_T \left(z_{\text{max}} - z_{\text{max,new}} \right) \tag{3.13}$$

where:

V_{slump} The volume that has to be transported due to a slump [m^3]

V_{ini} The initial volume under the three depth points before a slump [m^3]

V_{end} The volume under the three depth points after a slump [m^3]

A_T The area of the triangle defined by the three bed level points ABC [m^2]

$z_{\min}$ The minimal height of the three depth points [m]

z_{mid} The median height of the three depth points [m]

$z_{\max}$ The highest of the three depth points [m]

The volume of sediment that slumps is transported as bed load:

$$S_{slump,u} = \frac{\rho_s V_{slump}}{\Delta x \, \Delta t} \frac{u}{\|\mathbf{u}\|} \tag{3.14}$$

$$S_{slump,v} = \frac{\rho_s V_{slump}}{\Delta y \, \Delta t} \frac{v}{\|\mathbf{u}\|} \tag{3.15}$$

The bed-load due to the slumping is equally divided over the different sediment fractions. When no sediment is available, no slumping will occur. If there no sediment available from one of the fraction, the magnitude of the transport is less than that when it would be available.

3.3 Results of a test in a channel with steep banks

To test the three slope slumping formulations, the formulations are implemented in a model of a straight channel with steep banks of 35 degrees. Both banks are modelled with 7 grid cell. The sizes of the grid cells, as well as the width of the model, are similar to that of the model of the Eminence pool. Figure 3.6 shows a cross-section of the initial topography and water level of the model and Table 3.1 shows the input data of the models.

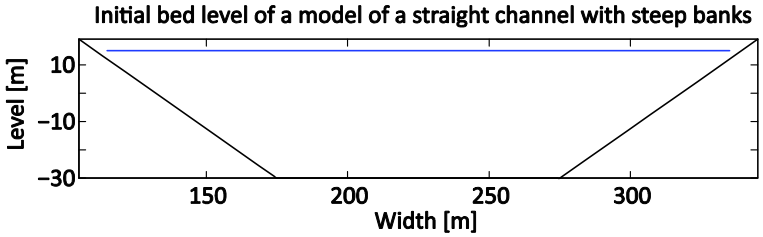

Figure 3.6: Cross-section of the initial topography and water level of the channel with steep banks

Table 3.1: Input parameters of the model of the channel with steep banks

Variable	Value
Computational time	8 hours. (slope to equilibrium slope: 30 min)
Morfac	1
Simulated time	8 hours
Time step	0.02 minutes
Spin-up interval	Restart file 4 hours

Domain length	876.3 metre, grid length 12.7 metre
Domain width	250 metre, grid width 10 metre
Depth	45 metre
Bank slope	35 degrees
D_{50}	100 μm
Roughness z_0	0.001 metre
Inflow boundary	Total Discharge: 0.058 m^3 s^{-1}
Outflow boundary	Water level 0.14 metre
Sediment inflow D_{50}	0 kg s^{-1}
Aksfac	1
Bed slope effect	Koch and Flokstra
Ashields	1.5
Bshields	0.5

Figure 3.7 shows the initial bed load transport and velocity over the width of the model. It shows the difference in direction due to the bed slope effect.

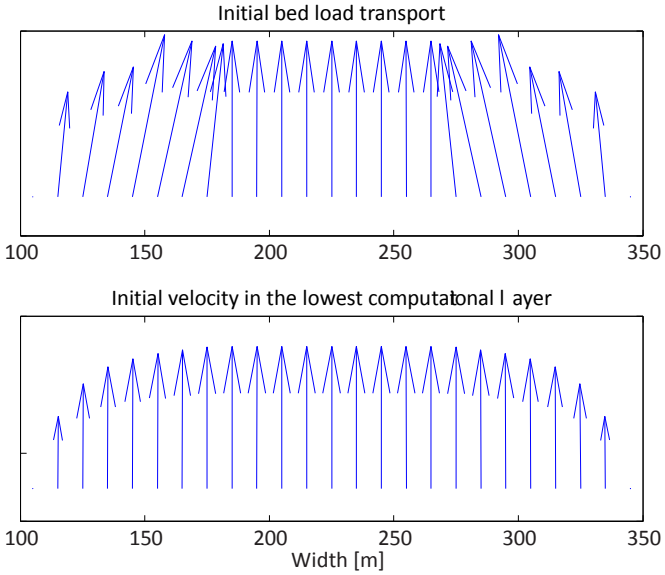

Figure 3.7: Bed load transport (above) and velocity (below) at the start of the morphological computation

Figure 3.8 shows the cumulative erosion and sedimentation of the three models described in section 3.2 relative to a reference run, where no slope slumping occurs. The model where no sedimentation is allowed on a steep slope and the model where the sedimentation is transported as bed load show similar results. Figure 3.9 shows a cross-section at 680 m from the inflow boundary. In this figure it is clear that the sedimentation to bed load formulations has a larger deposition at the flat bed. However, the effect on the banks is negligible.

When the slope is changed to the equilibrium slope a much larger effect is seen. The right side of Figure 3.9 shows that the slope is eroded 2.5 metres and deposited down the slope. This is nearly 10 times more than according to the other two formulations. The lowest plot in Figure 3.8 shows the erosion and sedimentation along the whole domain for the slope slumping formulation. Here are some unexplained differences in bed level. At some grid cells the erosion differs much from that of the neighbouring cells. The pattern is in the direction of the bed load. However, there is no explanation for this at the moment.

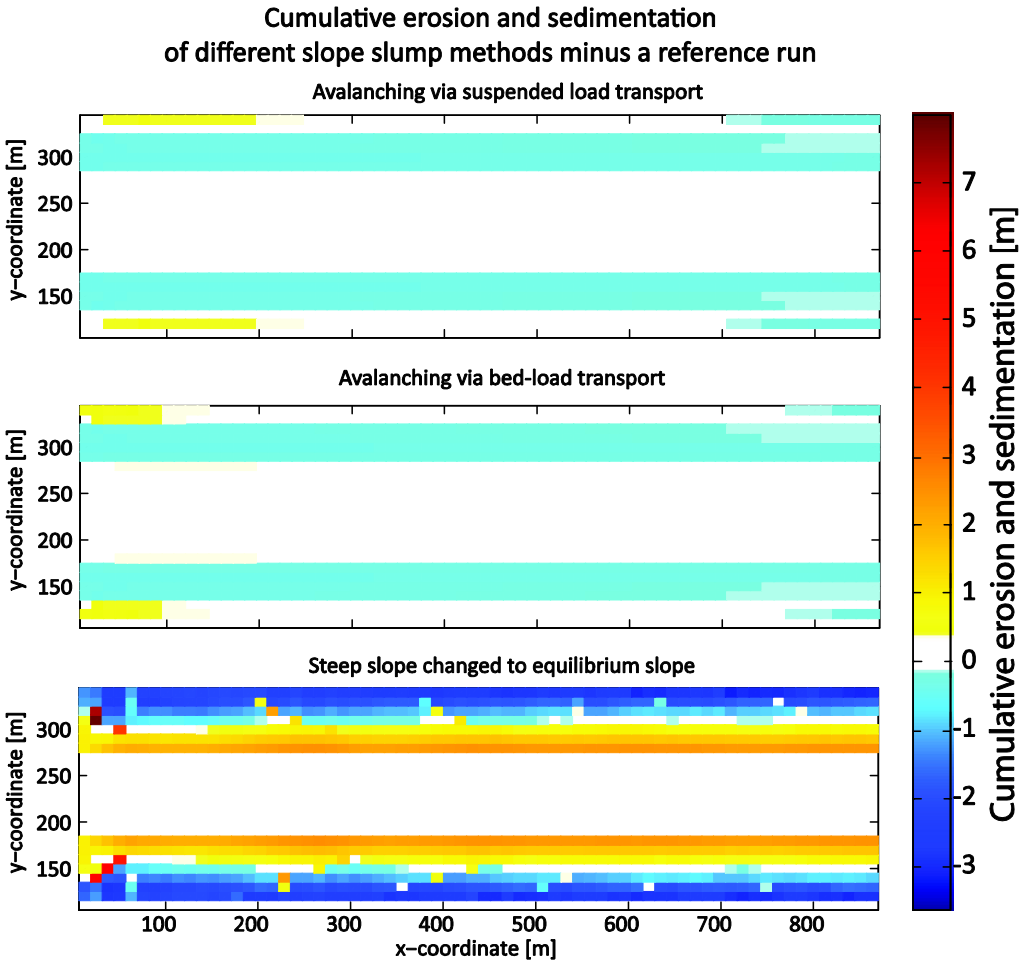

Figure 3.8: cumulative erosion and sedimentation of different slope slumping methods minus a reference run without slumping

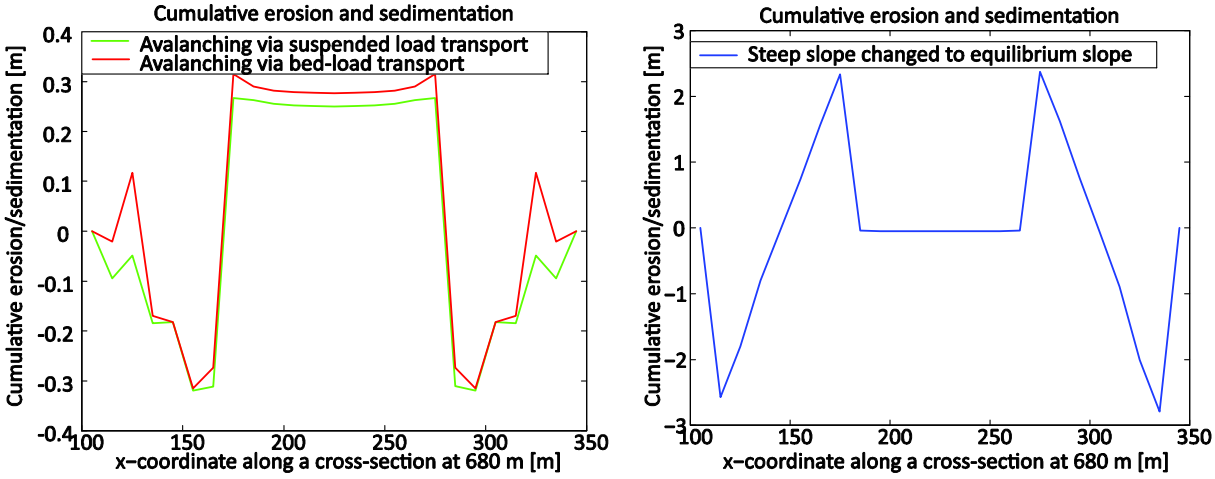

Figure 3.9:Cross-sections of cumulative erosion and sedimentation of the two avalanching methods minus a reference run without slumping (left) and the steep slope change to equilibrium slope minus a reference run without slumping (right)

4 Application to the Eminence pool model

4.1 State of the art modelling

In the models of Sloff, Kemp and Logan, the influence of 5 model parameters were investigated. Logan showed that the eddy diffusivity of sediment is negligible compared to the advection of sediment. When the eddy diffusivity is set to zero, this has little effect on the deposition in the eddy. (Logan et al., 2010)

An increase in horizontal eddy viscosity showed to dampen the temporal velocity fluctuations. These fluctuations cause the sediment to flow into the eddy. Thus, an increase in horizontal eddy viscosity leads to less sediment transported into the eddy. (Logan et al., 2010)

A decrease of roughness height and the coupled reference level leads to a higher reference concentration. The sediment is carried further into the eddy and higher into the water column. This causes the sandbar to become longer (Sloff et al., 2009). Logan used a roughness height of 0.05 m upstream of the Eminence pool and 0.001 m in the rest of the domain in order to calibrate the water levels correctly (Logan et al., 2010). Due to the sudden difference in the roughness the model computed a large spatial difference in turbulent kinetic energy.

Besides the hydrodynamic parameters, the morphologic parameters have also been tuned. The inflow of sediment in the model has a large impact on the final topography. During the 2008 HFE concentration measurements were conducted in a pool between the Eminence and the Willy Taylor pool. These concentrations were used as input for the boundary upstream of the Eminence pool. Sloff found that the model performed at best when half of the measured sediment inflow was taken as a boundary condition. (Sloff et al., 2009)

The first model created by Sloff used a uniform layer of sediment of 1 meter consisting out of 5 sediment fractions. Kemp computed the availability of sediment using by subtracting the lowest bed level measured at every spot from the bed level before the 2008 HFE. Logan performed a limited sensitivity analysis on the size of the bed-fractions as well on the thickness of the initial sediment layer. She concluded that both had a negligible impact on the final topography of the sand bars. (Logan et al., 2010)

4.2 Modelling methodology applied in this thesis

The model of Liz Kemp included both the Eminence pool and the Willy Taylor pool. The model used by Brandy Logan was cut off right after the Eminence pool. The reason behind this is the lack of recent topography data in the rapid between the Willy Taylor pool and the Eminence pool. Therefore the water levels at this location could not be well described by the model.
In the Eminence pool an eddy developed. This eddy was during the simulation on the boundary, and therefore velocities at the outflow boundary where directed toward the model. This eddy is very important for sediment distribution. Therefore in this study the domain is extended to halfway the Willy Taylor pool. Table 4.1 show input parameters of the model. Table 4.2 shows the sediment fraction used in the model.

Table 4.1: Input parameters for the Eminence pool model

Variable	Value
Computational time	26.83 hours
Morfac	6
Simulated time	6 days and 11 hours
Time step	0.025 minutes
Spin-up interval	1 hour
Domain length	1.15 Km
Domain width	Maximum 170 metres
Depth	Maximum 16 metres
Roughness z_0	Varying from 0.05 upstream to 0.001 near the pool
Inflow boundary	Discharge per grid cell, see section 4.2.3
Outflow boundary	Water level, see section 4.2.4
α_{sus}	2 · 0.54 = 1.08
α_{bed}	2 · 0.35 = 0.7
Aksfac	1
Bed slope effect	Koch and Flokstra
Ashields	1.5
Bshields	0.5

Table 4.2: Sediment used in the model of Kemp and Logan (Logan et al., 2010)

Grain fraction	Grain size (mm)	Range (mm)	Fraction of the bed
Very fine sand	0.088	0.062-0.125	0.055
Find sand	0.176	0.125-0.250	0.405
Medium sand	0.354	0.250-0.500	0.458
Coarse sand	0.707	0.500-1.000	0.080
Very coarse sand	2.000	1.000-4.000	0.002

4.2.1 Grid, depth and erodible layers

Figure 4.1 shows the computational grid of the Eminence pool. The depth of the model is interpolated to these grid points from the 2 measured profiles in 2008 of the two pools. The empty spots are filled with the data from December 2004. This was after the HFE of 2004, which occurred in November. Some data at the banks were still blank. This is filled in using an interpolation method. Figure 4.2 shows this initial depth profile.

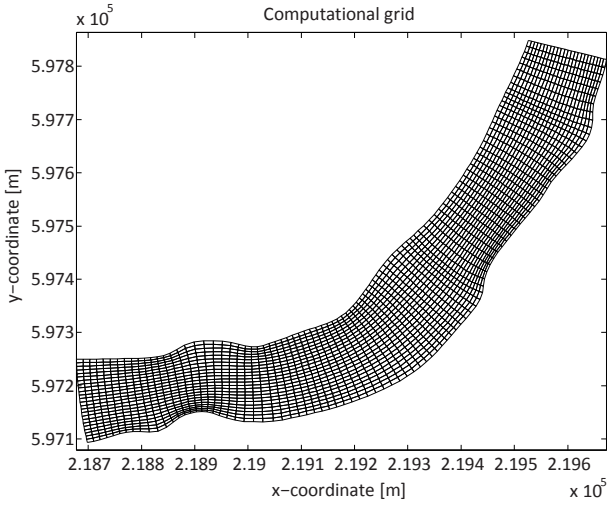

Figure 4.1: Computational grid of the Eminence pool

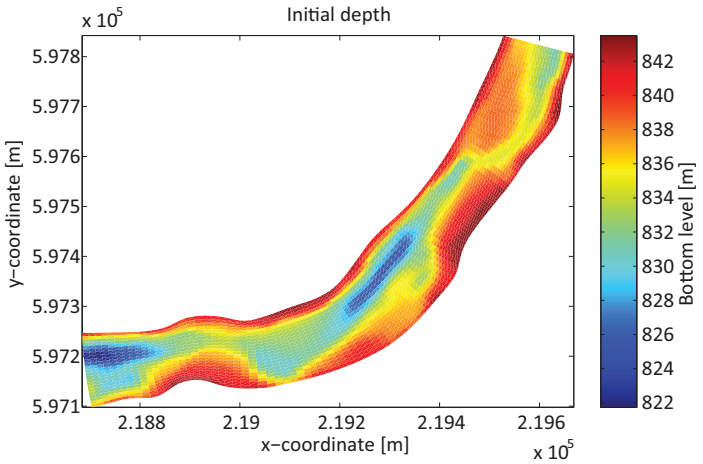

Figure 4.2: The initial depth of the model of the Eminence pool

The Colorado River flows through a rocky area. Therefore, the bed does not only consist of alluvial sediments. At some parts of the river no sediment is available. Figure 4.3 shows how large the layer of available sediment is. This layer is computed by extracting the highest measured bed level by the lowest measured bed level.

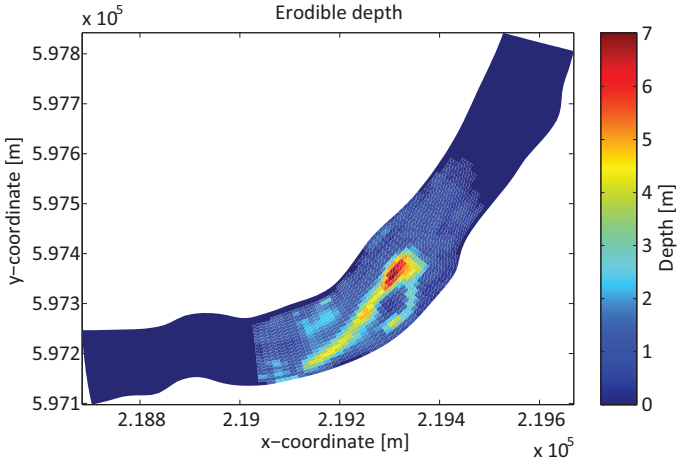

Figure 4.3: The initial erodible depth of the model of the Eminence pool

4.2.2 Recalibration

Due to the extension of the model, the model has to be recalibrated again for the hydrodynamic behaviour. The calibration is possible in many ways. A common way is to adapt the roughness. The model responds very sensitively to this parameter. Therefore when the model is calibrated for one situation, this does not mean it is able to describe another situation as well. In this situation, the primary calibration is done by calibrating the boundaries.

4.2.3 Inflow boundary

Figure 4.4 and Figure 4.5 show the measured hydrograph at the Eminence pool in blue. The discharge used as the upstream boundary condition is represented in red. Figure 4.4 show the topography measurements. The black squares show that in those measurements a slope slump was visible. In Figure 4.5 the velocity measurements of the Eminence pool are plotted.

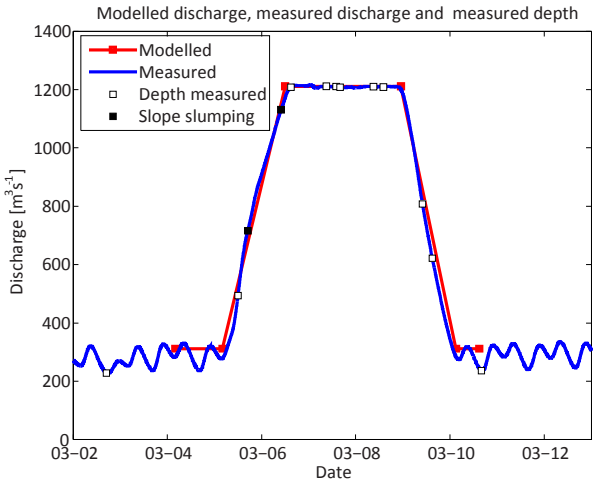

Figure 4.4: Modelled and measured discharge including depth measurements

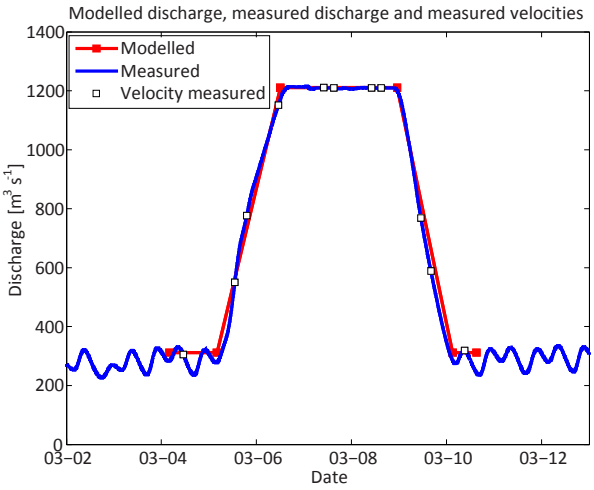

Figure 4.5: Modelled and measured discharge including velocity measurements

The inflow boundary used in the model is a discharge per width. In the earlier model a total discharge was used. The total discharge can cause numerical instabilities, due to the distribution of the discharge among the grid cells based upon the water height. When the water depth changes much in a short time, the discharge will also change a lot. This causes the water level again to change. Resonance may occur this way. When morphology is included it is even more instable due to the responds of the bed on the changing velocities.

The inflow boundary has a discharge per grid cell, defined per grid cell. For each grid cell a discharge is calculated.
The discharge is in a stationary flow

$$Q = B\,h\,C\sqrt{h\,i} \tag{4.1}$$

Thus, the proportionality of Q can be expressed.

$$Q \sim Bh^{3/2} \tag{4.2}$$

For each grid-cell $Bh^{3/2}$ is calculated. The discharge for a specific grid cell is the total discharge times the $Bh^{3/2}$ value divided by the sum of all $Bh^{3/2}$ values. The same method is applied for the sediment inflow. However this is divided over the specific discharge $Bh^{1/2}$. The inflow is sediment is taken less than in the model of Logan or Kemp, because these models over-predicted the sandbar height.

4.2.4 Outflow boundary

The outflow boundary is a water level boundary. The outflow of the model is a water level boundary. This water level is based upon the discharge using the formula from (Hazel Jr et al., 2006):

$$h = 835.5083 + 0.0066\,Q - 1.6682 \cdot 10^{-6} Q^2 \tag{4.3}$$

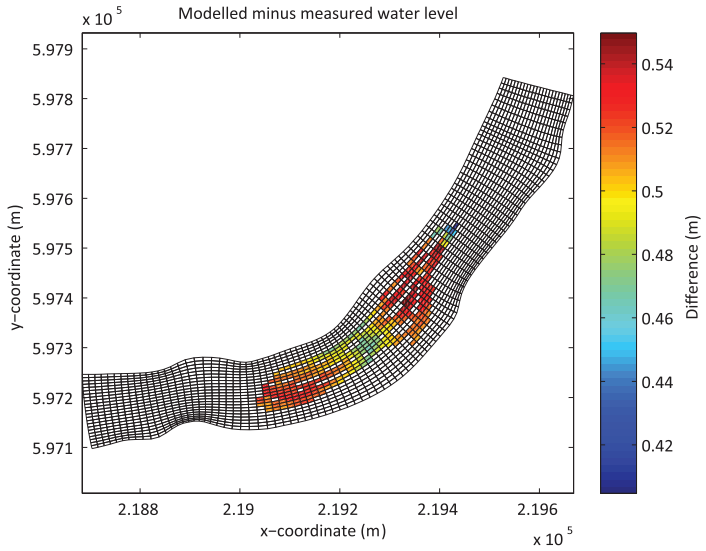

4.2.5 Transport formula and method for slumping and avalanching

The transport formula for suspended load and for bed load transport derived in section 2.2 (Van Rijn i.t.) is used in the model. The results computed with Van Rijn i.t. are compared to the results of Van Rijn 1993.

The two methods for avalanching and the method for slope slumping as described in section 3.2 are included in the model.

4.3 Results of the Eminence pool model

4.3.1 Hydrodynamics

Figure 4.6 and Figure 4.7 show the measured depth averaged velocities versus the computed ones. Figure 4.8 shows the initial topography as a reference for the next figures. All figures show the same part of the Colorado River. Figure 4.6 shows the velocities on the rising part of the hydrograph at 5 March 19:00. The direction of the measured velocities corresponds with the computed velocities. There is a slight difference in the location of the eddy centre. Figure 4.7 shows the velocities at the stationary part of the hydrograph at 7 March 10:00. The eddy centres of the computed velocities and the measured ones, differ a little bit more.

The measured and computed flow patterns downstream of the eddy behave differently. The measured velocities are more spread across the width of the channel, whereas the computed velocities show an eddy at the right bank. There is no topography data available of the rapid between the Eminence pool and the Willy Taylor pool. The initial topography in the model shows a little bump near the right bank at this rapid. This causes the water to flow more to the left bank than to the right bank. Also the velocities near the right bank would be higher when the bump would not be present. There is no topography data of the rapid, it is also said to be non-erodible. The topography at this

location does therefore not change and therefore the flow stays more to the left bank, than to the right.

The computed velocity at the reattachment point is more curved to the left than the measurement show. In a 3D model, this leads to a spiral bend flow. The flow velocities near the bottom are directed more towards the eddy than in reality, transporting more sediment into the eddy than in reality.

Downstream of the eddy the opposite is happening; here the flow is curved to the right, whereas the measurements show a straighter pattern. In combination with the eddy at the right bank, this gives an extra deposition near the right bank.

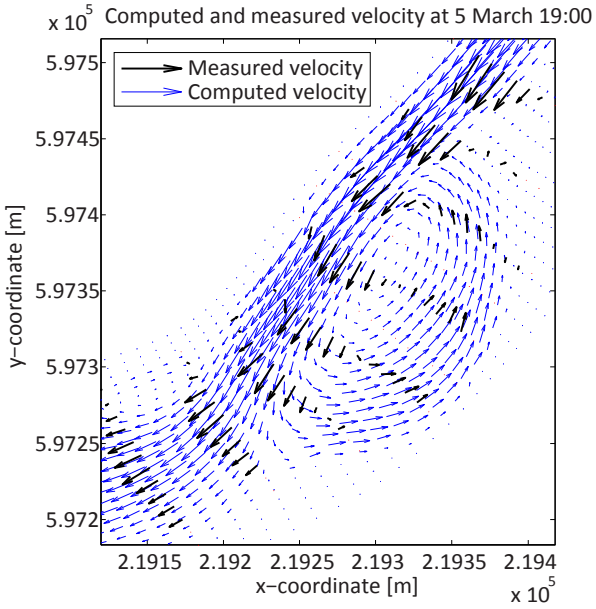

Figure 4.6: Measured and computed velocities at the Eminence pool at 5 March 19:00

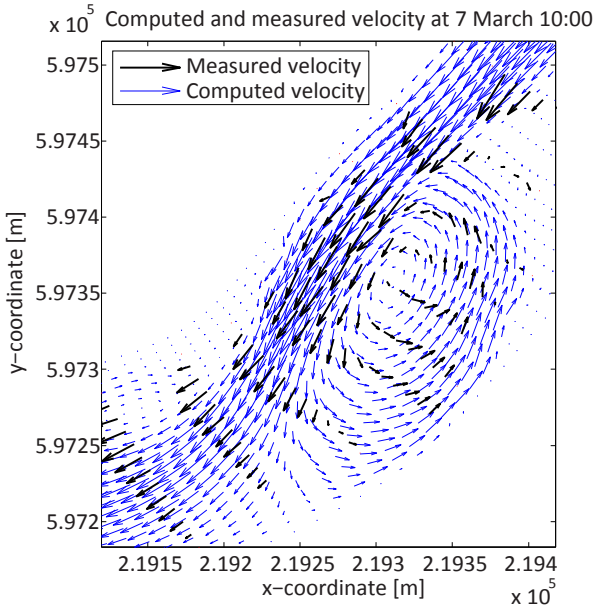

Figure 4.7: Measured and computed velocities at the Eminence pool at 7 March 10:00

Figure 4.9 shows the relation between the velocity and the turbulent kinetic energy for the morphologic computation with Van Rijn 1993. The velocities and TKE of the lowest computational layer for every hour between ray 35 and 65 are plotted. These rays correspond with the area at which the Eminence pool is present. The plot shows a distinct increase of turbulence when the velocities are higher. Also there are low velocities with a high turbulence. The time-averaged flow has also a contribution to the TKE; therefore it makes sense that there is a lower boundary to the TKE at different velocities.

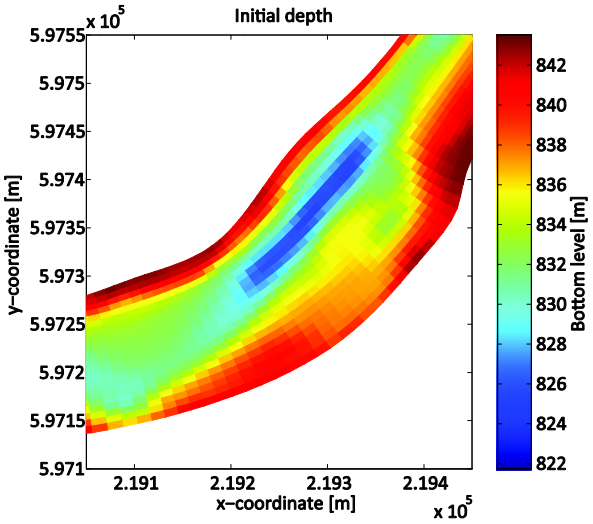

Figure 4.8: Initial bed level of the Eminence pool

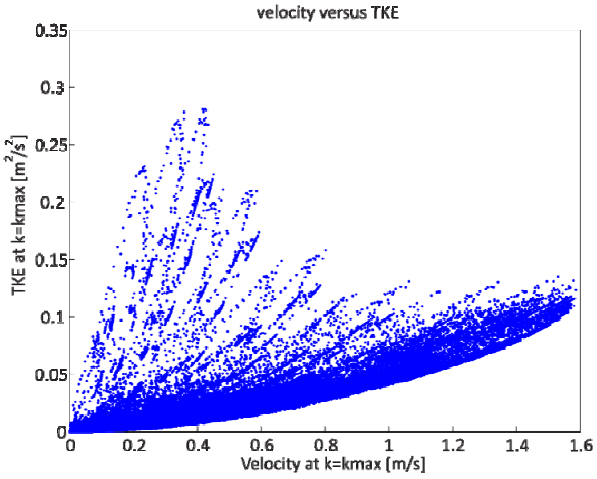

Figure 4.9: Velocity versus turbulent kinetic energy

4.3.2 Morphodynamics

There are 5 key points that were predicted wrongly in the previous models. The first column of Table 4.3 shows the aspects of the model, the second column specifies what was wrong about these aspects in the previous models. The third till last column shows the improved formulations of this thesis. The next section will give more detailed information about the improvement of these aspects when Van Rijn i.t. is used. The two sections thereafter will respectively show the improvement for a higher an-isotropy factor and for the avalanching formulations

Table 4.3: Key aspects of the previous and current models

Aspect	**Previous models**	**Van Rijn i.t.**	**Van Rijn i.t. + an-isotropy factor**	**Both avalanching formulations**
Sandbar height	Too high	Less high, due to less sediment input	significantly lower than previous models	Less high, due to less sediment input
Extension of sandbar into the pool	Too far	Even further than previous model	Higher an-isotropy factor leads to further extension	Even further than previous model
Representation of steep banks	Too steep (max 43 degrees)	Less steep (max 40 degrees)	Steeper than in previous model (46 and 51 degrees).	Less steep (max 40 degrees)
Width of the main stream	Too small	Improved, but still too small	Widens with a higher an-isotropy factor. With $\alpha_u = 2$, it represents the measurements	Improved, but still too small
Erosion hole in the main stream and pool	none	none	none	None

Van Rijn including turbulence

The first deficit the previous models of Kemp and Logan showed was an over-prediction of the reattachment bar height. Therefore the sediment inflow at the boundary was diminished. This caused a sediment shortage in the model and therefore the base of the reattachment bar was eroded. Figure 4.11 shows the measured difference in topography and here a deposition is visible at the reattachment bar. When Van Rijn 1993 is used the erosion is a little bit more (Figure 4.10, left) than for Van Rijn i.t. (Figure 4.10, right). This is also clearly visible in the difference between the two (Figure 4.12). Van Rijn i.t. computes a lower near-bed reference concentration, leading to less erosion at the base of the reattachment bar.

When the sediment inflow in the model would be increased, it is suspected that there will be a deposition at the base of the reattachment as was visible in the computed bed levels of Logan and Kemp.

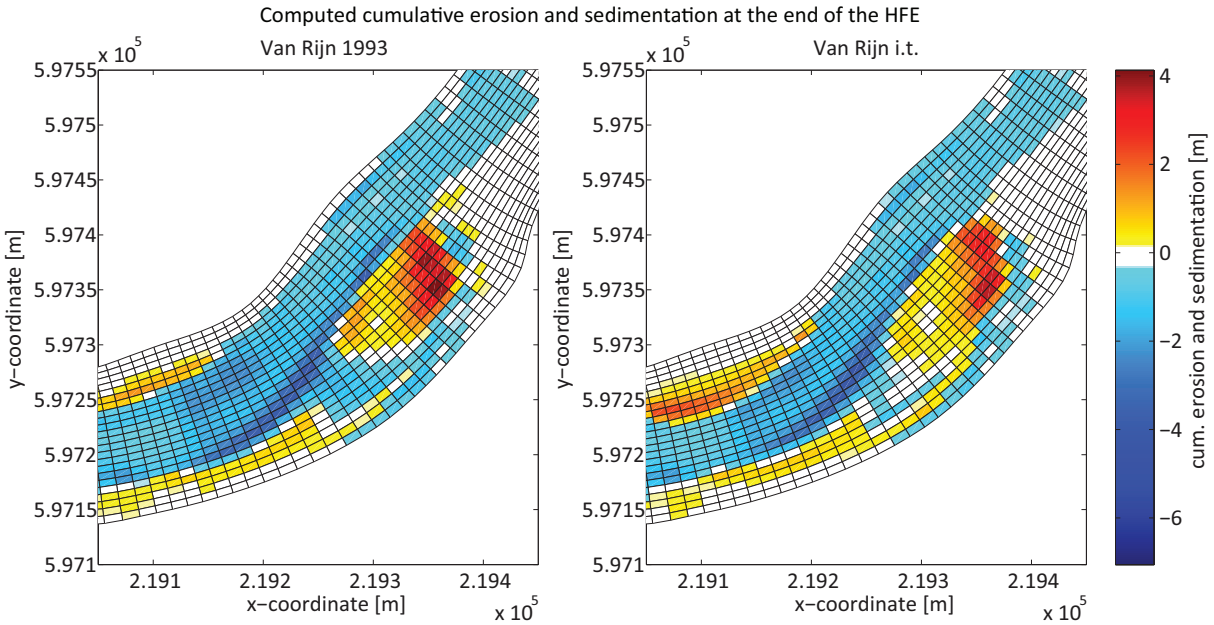

Figure 4.10: Computed cumulative erosion sedimentation at 10 March 15:00 for Van Rijn 1993 (left) and Van Rijn i.t. (right)

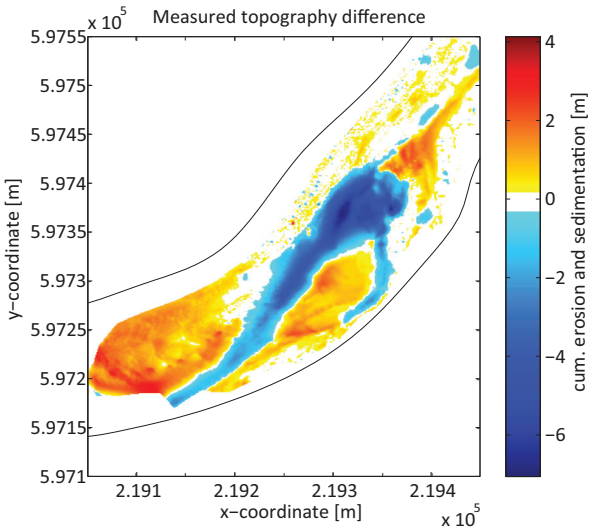

Figure 4.11: Measured topography difference before and after the HFE

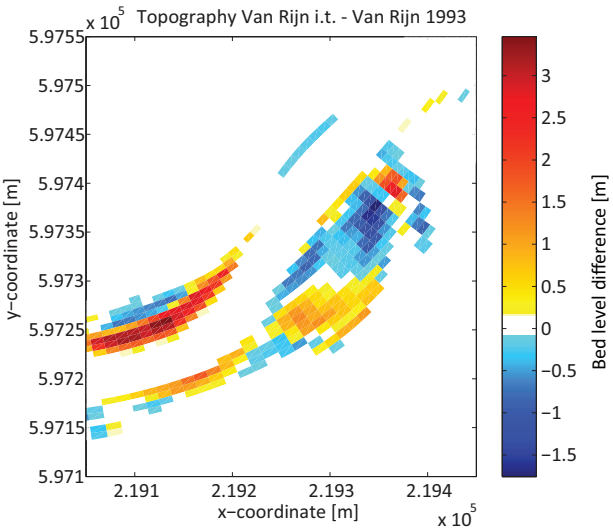

Figure 4.12: Topography computed with Van Rijn i.t. minus Van Rijn 1993

The second problem with the models was that the sandbar extended too far into the pool. Figure 4.14 shows the difference between the computed topography and the measured topography for Van Rijn 1993 (left) and Van Rijn i.t. (right). The red areas in the figure show more deposition in the model than in reality. Both formulations show an extension too far into the pool.

In the eddy the turbulence near the bottom is increased (Figure 4.14). Therefore Van Rijn i.t. will keep the sediment longer into suspension and extending the sandbar. In Figure 4.12 the positive, red values show that Van Rijn i.t. predicts a higher bed level than Van Rijn 1993. It is visible that the sandbar extents more into the pool in the computation using Van Rijn i.t.. The avalanching and slumping formulations should make sure that the slope does not extent too far. More on the effect of turbulence will be shown in the nest section, where a sensitivity analysis is performed on the influence of turbulence on the sandbar. The sandbar computed by Van Rijn i.t. will not be as high as Van Rijn 1993. Probably due to the lesser sediment transport. Figure 4.15 shows the relative total transport difference between Van Rijn 1993 and Van Rijn i.t.. Blue means that Van Rijn i.t. computes less transport. In most of the domain Van Rijn i.t. under-predicts the transport compared to Van Rijn 1993.

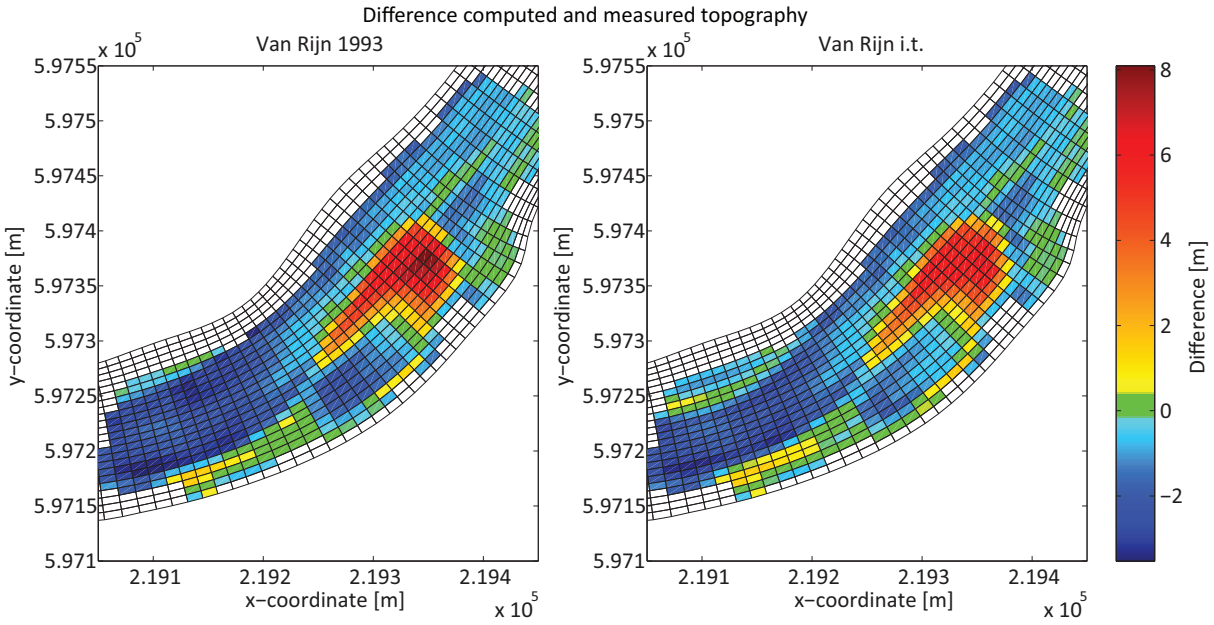

Figure 4.13: Difference between measured and computed topography for Van Rijn 1993 (left) and Van Rijn i.t. (right)

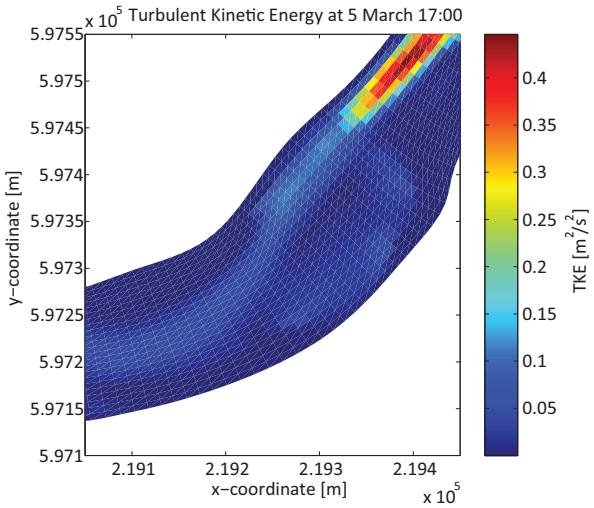

Figure 4.14: Turbulent kinetic energy for Van Rijn i.t. on the rising part of the HFE at 5 March 17:00

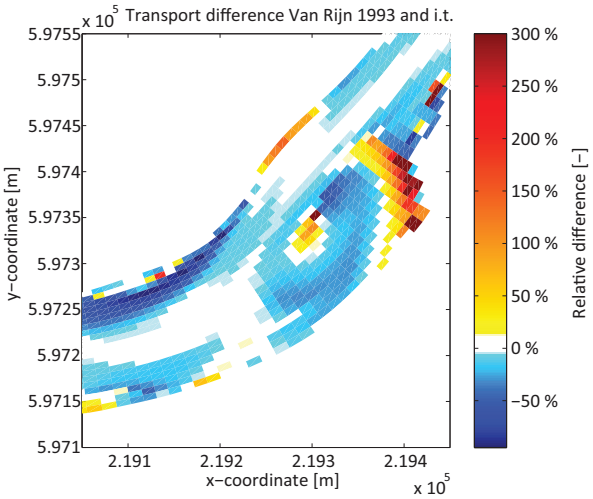

Figure 4.15: Time averaged total transport difference between Van Rijn 1993 and Van Rijn i.t.

The previous models showed a narrowing of the channel in comparison to the measurements. In the extended model this is also the case. Figure 4.16 shows the measured and computed cross-sections upstream of the reattachment bar of the Eminence pool. Figure 4.17 shows the cross-sections on top of the reattachment bar for the same computations and measurements. In Figure 4.17 Van Rijn i.t. computes a slightly wider main stream at the reattachment bar.

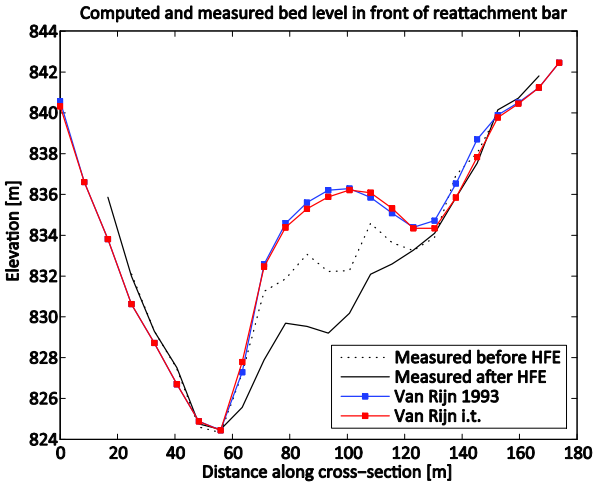

Figure 4.16: Computed and measured cross-section upstream of the reattachment bar before and at the end of the HFE

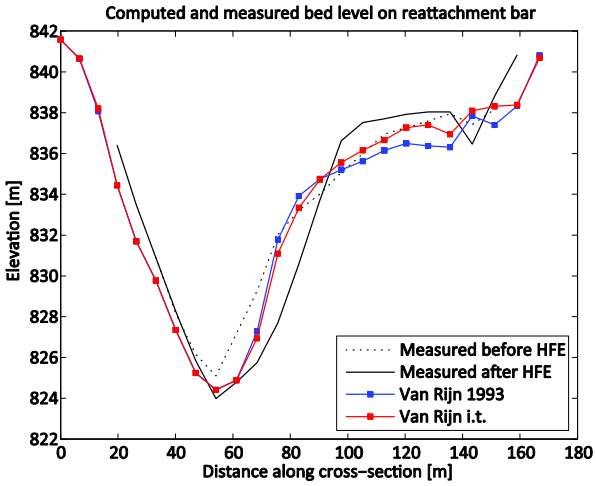

Figure 4.17: Computed and measured cross-section at the reattachment bar before and at the end of the HFE

The measured topography shows a scour hole in the main stream (Figure 4.11). This is not visible in the computed topography. The hypothesis was that including the turbulence would create this scour hole. In the model most of the main stream is aggregated. The topography in the modelled main stream differs much from reality. It can be concluded that including the turbulent velocity fluctuations in the sediment transport formula do not give a better representation of the scour hole.

The model using Van Rijn i.t. shows more realistic slopes of the reattachment bar. When Van Rijn 1993 is used the maximum angle is 43 degrees. When Van Rijn i.t. is used it is 40 degrees. The reason for this has to be found in the limited transport computed by Van Rijn i.t.. Figure 4.18 shows the bed

level and turbulence at the cross-section on the reattachment bar. There is increased turbulence at the foot of the slope. The Van Rijn i.t. formula will compute erosion at this area, therefore the steepness of the slope will increase. The turbulence cannot be the reason that the slope becomes more gentle. Therefore it is probably the lesser sediment transport.

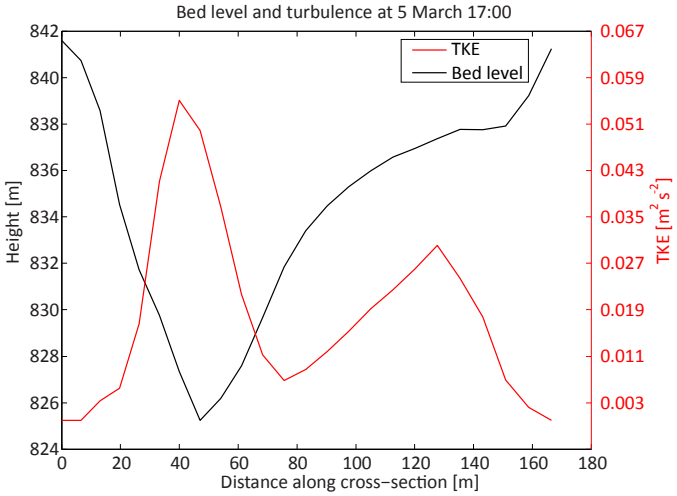

Figure 4.18: Bed level and TKE at 5 march 17:00 at the reattachment bar

Sensitivity analysis for influence of turbulence on deposition

Figure 4.19 shows the computed erosion and sedimentation when Van Rijn i.t. is used in combination with an an-isotropy parameter (described in section 2.2.2). The left part of Figure 4.19 shows the computed topography of an an-isotropy parameter of 1.5, the right shows the result when a value of 2 is used. The increased effect of the turbulence keeps the sediment longer in suspension. The sediment is deposited further into the pool. Also the sandbar becomes narrower. Sloff found the same effects, when the roughness height and the corresponding reference level were lowered. The effect is a larger near-bed reference concentration. The sediment will stay longer into suspension and is therefore transported further into the pool.(Sloff et al., 2009)

The height of the reattachment bar is significantly lower than the previous models of Kemp and Logan compute. The is partly caused by the lower amount of sediment flowing into the model and partly due to the sediment carried further into the Eminence pool.

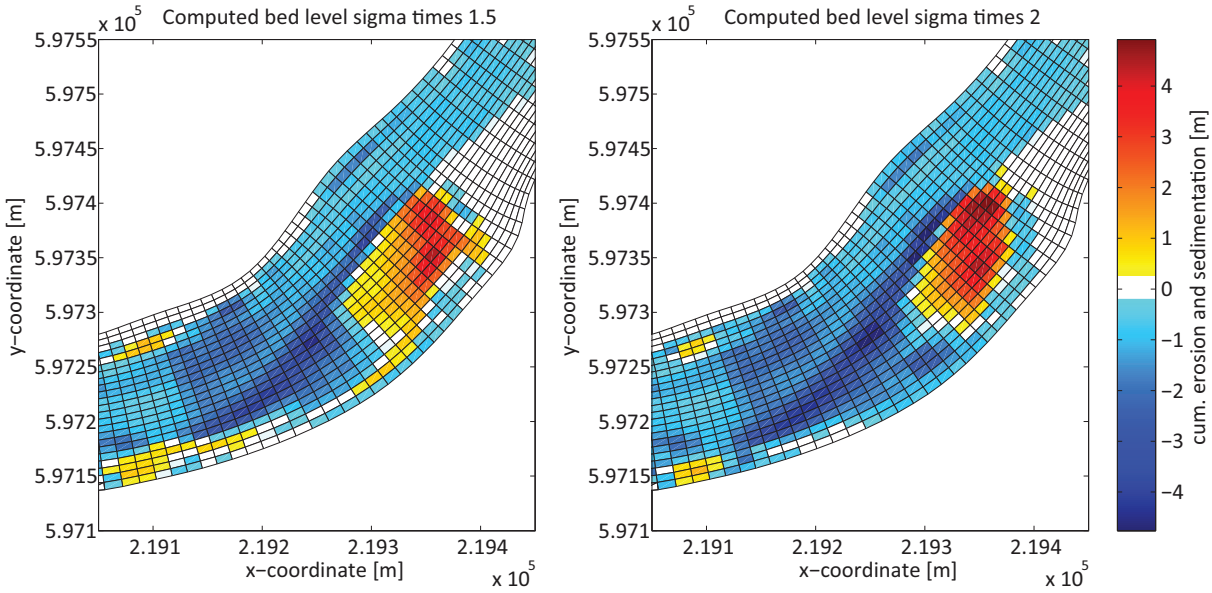

Figure 4.19: Erosion and deposition for Van Rijn i.t. using an an-isotropic parameter of 1.5 (left) and erosion and deposition for Van Rijn i.t. using an-isotropic parameter of 2 (right)

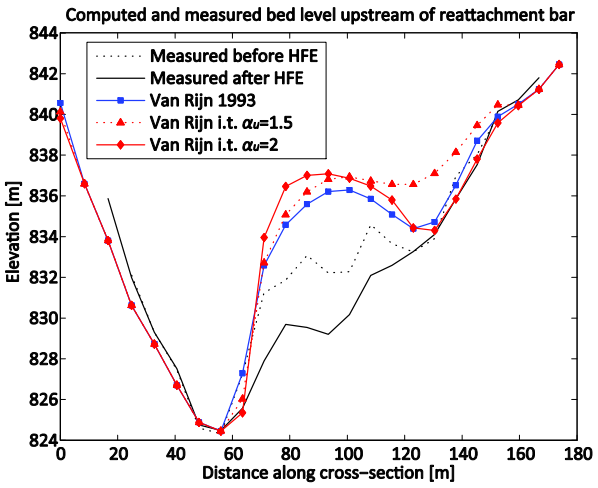

Figure 4.20: Computed and measured cross-section upstream of the reattachment bar before and at the end of the HFE for Van Rijn i.t. including an an-isotropy factor

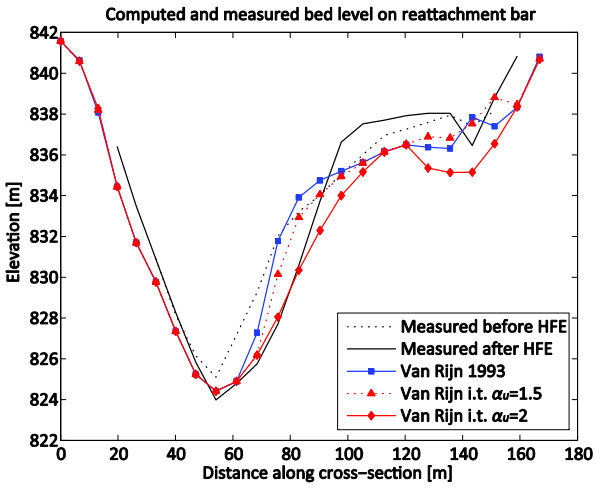

Figure 4.21: Computed and measured cross-section at the reattachment bar before and at the end of the HFE for Van Rijn i.t. including an an-isotropy factor

Figure 4.20 shows a cross-section of the measured and computed topography upstream of the Eminence reattachment bar. Figure 4.21 shows the cross-sections on top of the reattachment bar. The computations using an an-isotropy factor higher than 1 show a wider main channel. When an an-isotropy factor of 2 is used, the channel becomes as wide as was measured.

When an an-isotropy factor of 1.5 is used, the slope at the reattachment bar increases to 46 degrees. The an-isotropy factor of 2 shows a slope of 51 degrees. The increased turbulence is merely present at the foot of the slope. Increasing the effect of turbulence induces more erosion at this spot, which leads to a higher slope. The main channel does become wider, when a higher an-isotropy factor is used.

The erosion hole in the Eminence pool is also not reproduced with a higher an-isotropy factor. The sediment is carried further into the pool, where the measurements show an erosion hole.

Figure 4.22 shows the change in sediment thickness at the bed during the HFE. The spot is on the left side of the main channel at a location with increased turbulence as well as a thick initial sediment layer. The blue line shows the computation for Van Rijn 1993, the solid red line for Van Rijn i.t. for an isotropic condition. The transport computed by Van Rijn i.t. is lower than for van Rijn 1993. This is also visible when looking at the solid lines. It takes a longer time for the spot to be completely eroded when Van Rijn i.t. is used. When an an-isotropy factor is used the transport is increased, this is visible in an increased sediment thickness before the rising limb of the hydrograph. Also the sediment is eroded faster during the stationary part of the hydrograph.

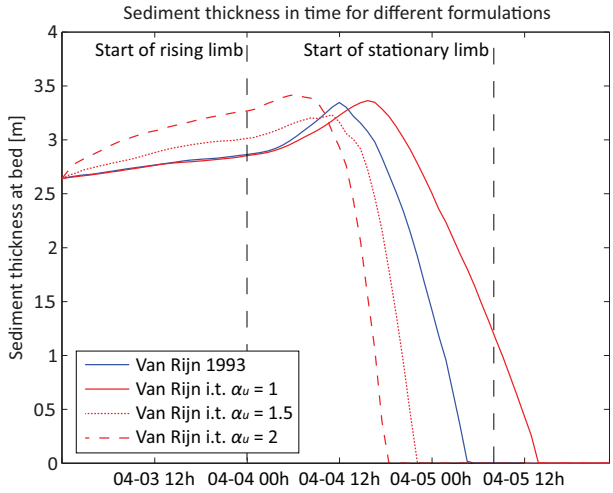

Figure 4.22: Sediment thickness at the bed at the left side of the main channel in time

Slope slumping and avalanching

The model including the slope to equilibrium slope of section 3.2.3 was not stable. Therefore this model shows no results. It is common for Delft3D to become instable when large bed level changes are applied. The Delft3d manual (Deltares, 2010) warns about the stability of the calculation when dredging and dumping is used. This is a similar large scale depth change as this slope slumping method. The change in topography due to the slumping triggered a water level oscillation, which made the model unstable.

When an avalanching formulation is applied a gentler slope is computed. In Figure 4.23, the maximum bed angles are shown, which occurred during the computation of the whole HFE. The left figure shows the result for Van Rijn 1993 without avalanching. The right shows the bed slope for the avalanching to bed-load as described in section 3.2.2. Van Rijn 1993 shows a maximum slope of 43 degrees. When the avalanching to bed-load or to suspended load is applied the maximum slope becomes 40 degrees. A critical angle of 32 degrees was used as parameter at which the slope should avalanche. The slopes are still significantly higher than the critical slope angel. This indicates that the erosion computed with the avalanching formulation is not high enough to cause the slopes to become as gentle as the maximum possible slope angle.

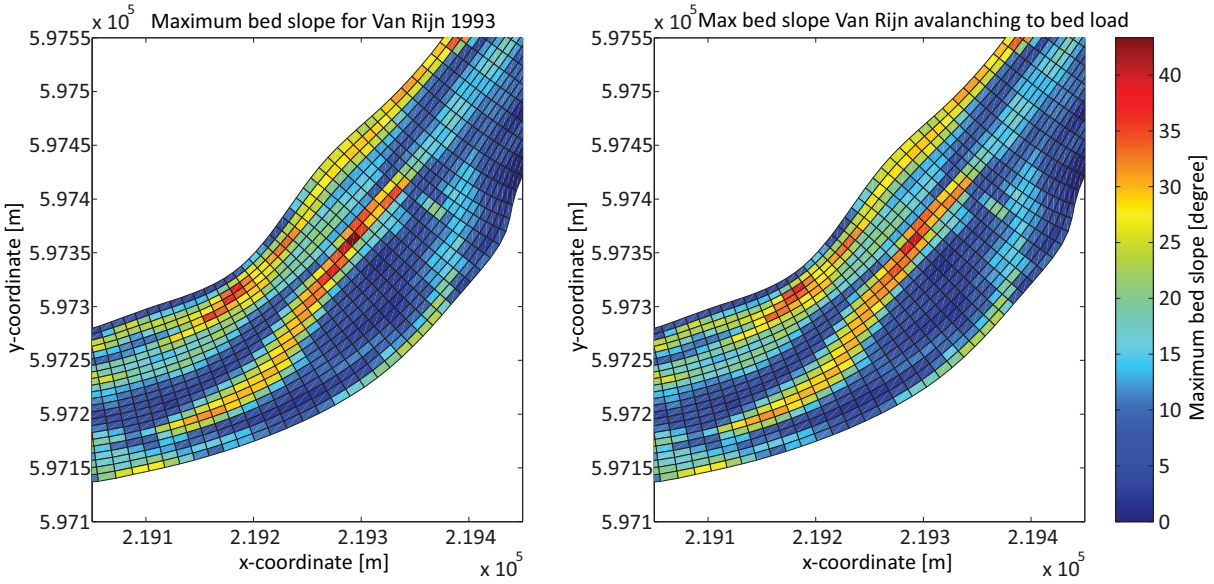

Figure 4.23: Computed maximum bed slope over the whole simulation for Van Rijn 1993 (left) and Van Rijn 1993 including avalanching to bed-load (right)

Figure 4.24 shows the difference between Van Rijn 1993 including the slope slumping formulations and Van Rijn. The left part shows the slope to suspended load formulation of section 3.2.1. The right part shows the slope to bed load formulation of section 3.2.2. A negative value means that Van Rijn with avalanching computes a lower bed level. The difference between the two avalanching formulations is small. When one looks at the difference between the avalanching formulations for Van Rijn i.t., the difference is more noticeable.

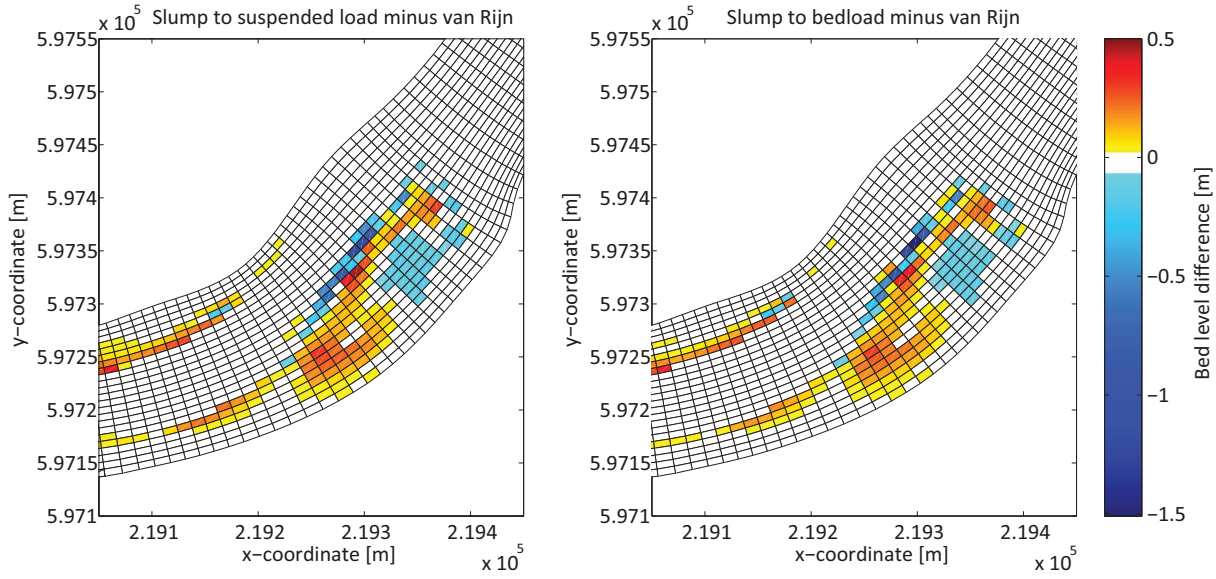

Figure 4.24: Bed level Van Rijn 1993 and slope slumping to suspended load minus Van Rijn 1993 (left), bed level Van Rijn 1993 and slope slumping to bed load minus Van Rijn 1993 (right)

A problem in the previous model was the computed main channel, which was too narrow opposed to reality. The Van Rijn 1993 formulation without avalanching (Figure 4.23, left) shows a large slope at the left bank of the main channel. Figure 4.24 and Figure 4.28 shows erosion at the banks of the bar. The amount of erosion does not equal the over-prediction of sedimentation. Figure 4.25 shows a

cross-section on top of the Eminence reattachment bar. The main channel is slightly wider, however not as wide as was measured.

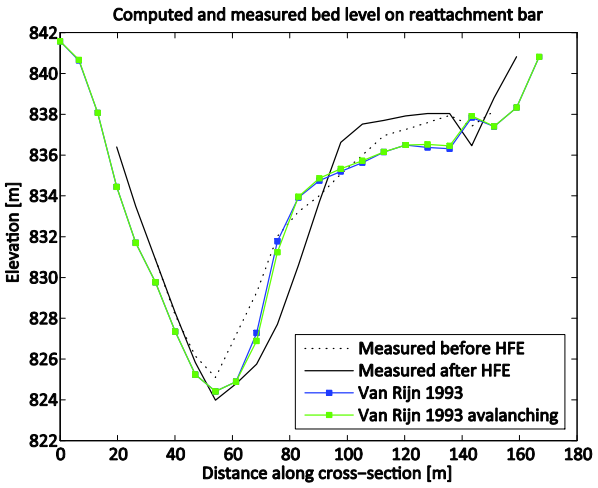

Figure 4.25: Computed and measured cross-section upstream of the reattachment bar before and at the end of the HFE for Van Rijn 1993 including avalanching to bed load

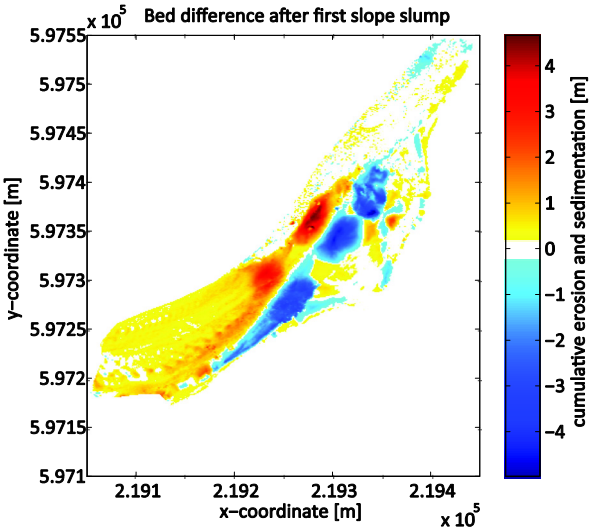

Figure 4.26: Topography difference between pre-HFE bed level and bed level after first slope slump

The sandbar modelled with Van Rijn 1993 was extended too much into the pool. At the extension, there is somewhat less sedimentation. However, the sandbar is extended further into the pool. The difference in sandbar height is almost certain not a direct influence of the avalanching formulation. Figure 4.23 shows no steep slopes at this location. The erosion is due to a difference in topography created by other avalanched spots. Figure 4.26 shows the difference in measured topography before the 2008 HFE and after the first measured slope slump during the HFE at 5 March 2008, 17:00h. The three blue areas indicate three places where slope slumpings have occurred.

From the analysis of these results a conclusive reason for the difference in bar growth cannot be given. The base of the reattachment bar showed more aggregation, when the avalanching formulation is used. A possible explanation could be that it is due to the difference in topography or the extra sediment that became available at the avalanching, This is the part of the bar, which was also present in the measurements. Thus, the height of the sandbar is better represented. In this computation the erosion hole in the pool was not visible.

Van Rijn including turbulence and avalanching combined

Table 4.4 shows the key aspects of the computed topography using Van Rijn i.t. and a slumping formulation.

Table 4.4: Key aspect of the topography computed with Van Rijn i.t. and avalanching

Aspect	Van Rijn i.t. and avalanching
Sandbar height	Higher than Van Rijn i.t.
Extension of sandbar into the pool	Further into the pool than Van Rijn i.t.
Representation of steep banks	37 degrees, significantly gentler than computed with Van Rijn i.t. or with avalanching separately
Width of the main stream	Wider than computed with Van Rijn i.t. or avalanching. Smaller than with an an-isotropy factor
Erosion hole in the main stream and pool	None

Figure 4.27 shows the difference between the combined results of the avalanching formulation including Van Rijn i.t. and Van Rijn 1993.

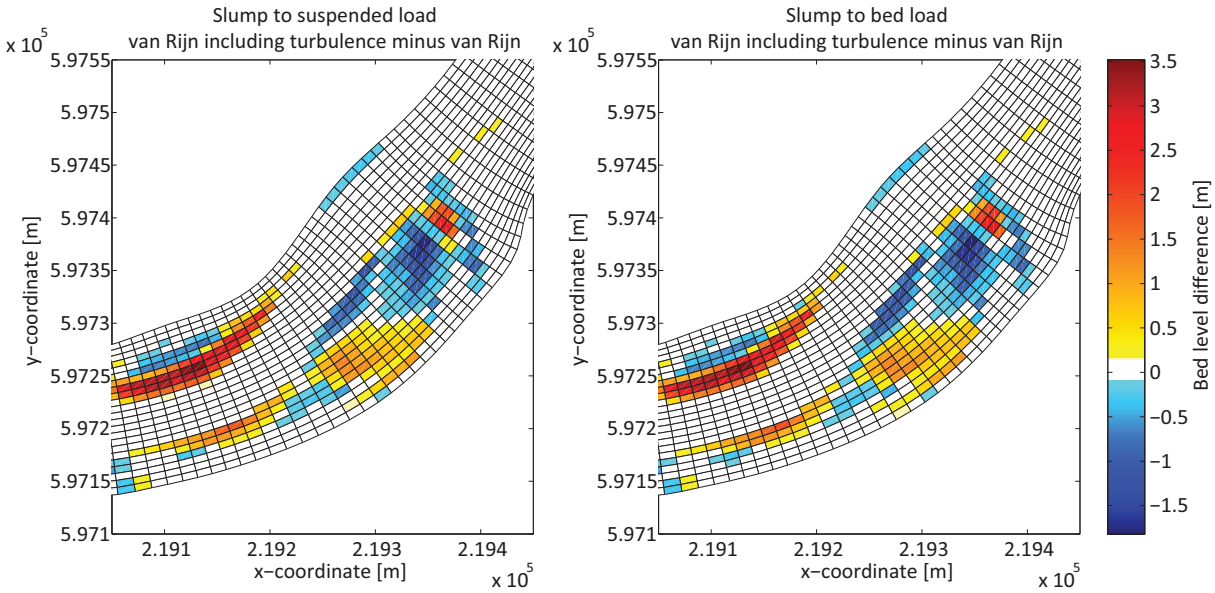

Figure 4.27: Bed level Van Rijn including turbulence and slope slumping to suspended load minus Van Rijn 1993 (left), bed level Van Rijn including turbulence and slope slumping to bed load minus Van Rijn 1993 (right)

The computed slope at the bank of the reattachment bar is 37 degrees. This is a gentler slope than computed using Van Rijn i.t. or using an avalanche method Also the main stream is wider than computed with Van Rijn i.t. or with avalanching. This is visible if one compares Figure 4.28 and Figure 4.27. Figure 4.28 shows the avalanching formulation including van Rijn i.t. minus Van Rijn i.t.. and Figure 4.27 shows the the avalanching formulation including van Rijn i.t. minus Van Rijn 1993. Figure 4.30 shows a cross-section on top of the reattachment bar. The wider main stream is clearly visible in this figure. All the models compute an increased turbulence at the foot of the slope of the reattachment bar. This area is eroded more when a computation is performed with Van Rijn i.t., than

when Van Rijn 1993 is used. The slope will become steeper; the avalanching method prevents deposition of sediment and thus the channel becomes wider.

The sandbar extents more into the pool, when the avalanching formulation is combined with Van Rijn i.t. (see Figure 4.28). This could be the effect of the wider main stream. The same can be seen when the avalanching formulation is used with Van Rijn 1993 (see Figure 4.24). The base of the reattachment bar is less eroded in comparison to Van Rijn i.t. (Figure 4.28) and Van Rijn 1993 (Figure 4.27). As for the other simulations, the erosion hole in the pool is not represented in this computed topography. The cross-section showed in Figure 4.29 is taken upstream of the reattachment bar. The measured erosion does not show in the computed topography.

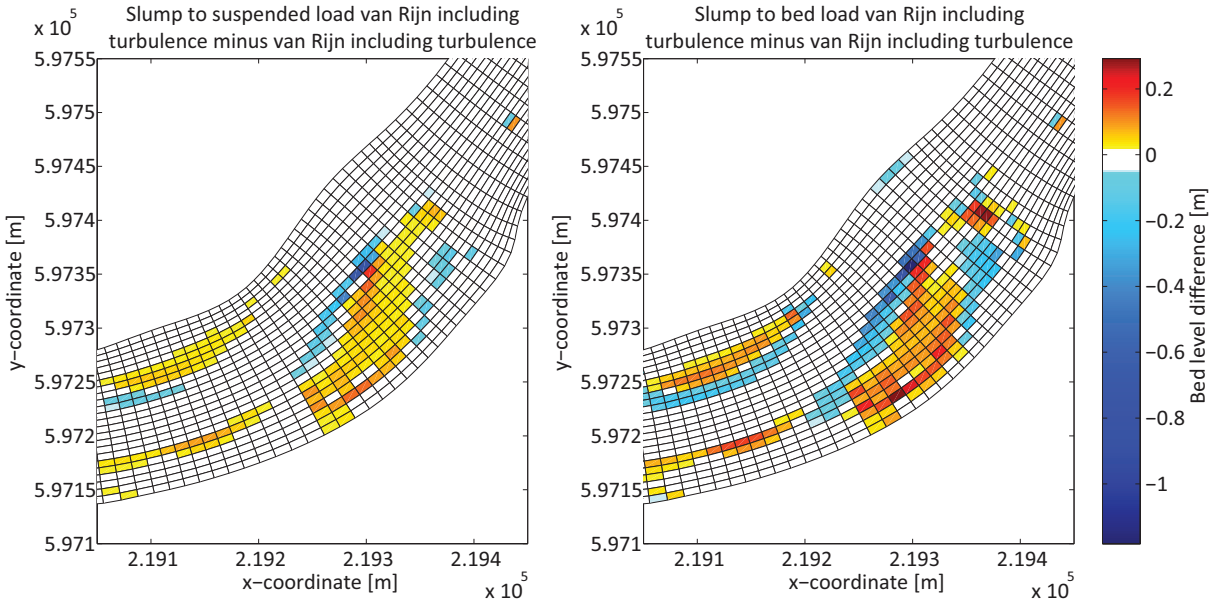

Figure 4.28: Bed level Van Rijn including turbulence and slope slumping to suspended load minus Van Rijn including turbulence (left), bed level Van Rijn including turbulence and slope slumping to bed load minus Van Rijn including turbulence (right)

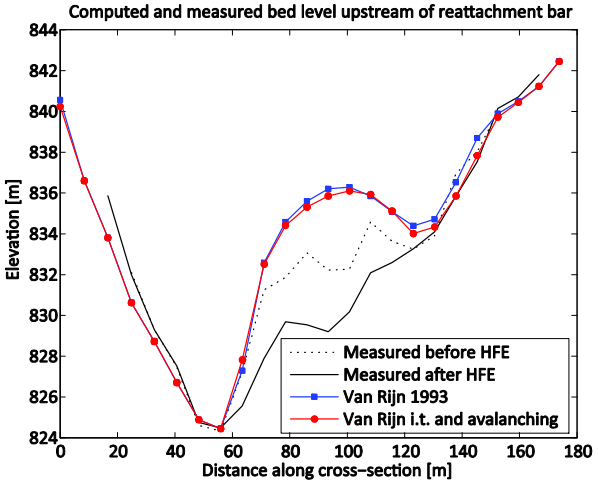

Figure 4.29: Computed and measured cross-section upstream of the reattachment bar before and at the end of the HFE for Van Rijn i.t. including avalanching to bed load

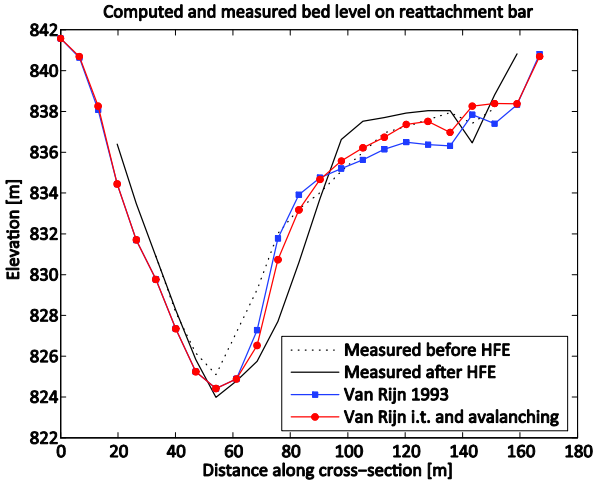

Figure 4.30: Computed and measured cross-section at the reattachment bar before and at the end of the HFE for Van Rijn i.t. including avalanching to bed load

5 Conclusions

The formulation for the near-bed reference concentration and the bed-load transport was improved by including the effects of turbulent velocity fluctuations. The developed steep slopes in the model were counteracted by the avalanching and slumping formulation. The results of the computations showed that an avalanching together with a formulation that includes turbulence has the potential of improving the computed topography.

5.1 Sediment transport

- The transport formula derived in this thesis, Van Rijn including turbulence (Van Rijn i.t.), is effective to erode more sediment at places with high turbulence. This is tested in a model of a confluence of two parallel river-sections with different velocities. The two river sections were modelled using a thin dam. There was a larger erosion hole behind the thin dam for Van Rijn i.t. than for Van Rijn 1993.
- Due to the limited amount of sediment available, all sediment in the main river at the Eminence pool is eroded for the Van Rijn 1993 formulation as well for Van Rijn i.t.. Therefore the amount of sediment eroded did not change. However, the scour whole was not simulated well, because the whole reach was eroded and not one spot.
- For the Eminence pool model Van Rijn i.t. computes a topography with a wider channel than Van Rijn 1993. When the influence of the turbulence on the near-bed reference concentration and bed load transport is increased the channel becomes even wider. This is more comparable with the measured channel width.
- The other deficits of earlier models of the Eminence pool were not improved by the new formulation. The over-prediction of the sandbar height was decreased by diminishing the sediment input. The measured erosion in the pool was still not visible in the model. This is probably triggered by the large difference in topography after the massive slope slumps.
- When Van Rijn i.t. was used the reattachment bar in the Eminence pool model extended even further into the pool. Also the banks of the reattachment bar became even steeper.

5.2 Slope slumping and avalanching

- Two avalanche formulations were introduced, which affect the transport and deposition when a critical slope is exceeded. Both avalanching formulas will create more gentle slopes in the Eminence pool model. However, the computed slopes are still larger than the critical angle at which avalanching occurs. A ban on deposition at steep slopes does not seem to work. The slump method where the slope is changed to the equilibrium slope performed well for the model of the straight channel. It showed the largest change in bed level. In the model of the Eminence pool the large change in bed level caused a water level oscillation, which caused the model to crash. This approach therefore needs further consideration.
- The effect of large slope slumps was dominant for the growth of the sandbar. The topography after the slump is significantly different than before. This will induce different hydrodynamic and morphodynamic behaviour.
- The avalanching model shows no avalanching at the tip of the sandbar. The computed slopes at this point are too gentle to fail. Either the slopes at the tip of the reattachment bar do not become as steep in the model as in reality, or the slopes fail at an angle lower than the angle of repose. If the latter is the case, then the slopes fail due to a reduced strength of the slope.

- Both the avalanching to bed load and slumping to suspended load perform well in describing the location of the avalanches. The large slumps that occurred during the HFE were not found in the computed bed level. The computed topography changes due to the avalanching are far less than the measurements show.
- When the avalanching formulation was used, the slope angle was changed from 43 to 40 degrees. The avalanching has effect, however not to the required extent.

6 Recommendations

6.1 Erosion problem

The growth of the sandbars can be increased by preventing the slopes from slumping. The model results of the avalanching model show erosion spots at places where also avalanching and slope slumping occurred. However, the failure mechanism is not precisely known. It should be examined whether the slumping could be caused by the erosion at the toe of the existing bar, or by the fluidization of the freshly deposited, unpacked sediments, or by a combination of both. Laboratory experiments could be carried out to investigate this.

When the failure mechanism or mechanisms are known, one could model a flood in the Colorado River to identify the areas where avalanching or slumping could occur. These areas could be reinforced before the High Flood Experiment is carried out. Clay, rock or a geo-textile could prevent a slope from avalanching and slumping. If one would apply this at every sandbar this would be too expensive. However, one could investigate at a few locations whether it has a positive effect.
At the falling limb and after the HFE, the pore pressures in the sandbar are high. This reduces the strength of the sandbar. If one would apply coarse sand drainage, these pressures would reduce and the strength of the bar would be increased.

6.2 Use of formulations in other fields

The Van Rijn i.t. formulation could be useful to model situations where high turbulence occurs.
An example could be a confluence of two river branches. Especially when the velocities differ much, turbulence becomes important. In the modelling of groynes, the erosion behind the tip of the groyne is not modelled well. The use of Van Rijn i.t. could be an improvement of such a model. Also the Van Rijn i.t. formulations would be useful when modelling a flow with a reattachment point. At this point there is scour due to high turbulence; however the average velocity is zero.

The formulation on avalanching could be used to model scour holes. These holes are known for their steep slopes.

6.3 Modelling approach

6.3.1 Improving derived formulations

- In the transport equations in this thesis natural logarithms are included. The natural logarithm is approximated in the Delf3D Fortran code using a finite series of expressions and takes a relatively long time to solve. A way to fasten the calculation is to use a look-up-table for this natural logarithm. For values in-between an interpolation method could be used.
- The influence of the parameters for the sediment transport in this thesis could be further examined. Such as the an-isotropy parameter, the calibration parameters, α_{sus} and α_{bed}, and the instantaneous critical entrainment velocity.
- The slope avalanching could be improved by not only stopping the deposition of sediment, but also eroding extra sediment. The slope slumping formulation could be improved by slumping less sediment per time step. This way, the slumping method does not trigger the water levels to become numerically unstable. In conclusion there has to be a formulation

eroding more sediment than the avalanching formulation and less than the slope slumping formulation.

6.3.2 Improving Eminence pool model

- Alter the topography at the rapid between the Eminence and the Willy Taylor pool. At this spot the bed levels have not been measured. The bed near the right bank is shallower than up- and downstream of the rapid. When this part is deepened the flow would go more toward the right bank, as is measured.
- The creation of a model of the situation after the slope slumping has occurred. In this way the sediment budget is specified at the right location. For this model the layers of available sediment should be updated to the new topography. The large bulge of sediment would move more into the main channel of the river.
- Creating a model where dredging and dumping are used to simulate the slope slumping. This could lead to an unstable model because of the major changes in topography. The dredging and dumping are a nice way to see whether the hydrodynamics and morphodynamics are described correctly. It would not be useful as an automatic slope slumping formulation, because one would have to specify where and what amount of sediment has to slump, but it gives an assessment of the impact of the slumping on the morphology.
- A better understanding of the sediment inflow and the composition of the bed at the Eminence pool. There are echo sounders which are able to measure the interface between the rocky bottom and the alluvial bed.
- A possibly better model could be made when the sediment fractions at the bottom would be layered. The deposition and erosion of different layers would then be administrated. When fine sand is deposited on top of coarse sand, the fine sand would be easier to entrain.
- In this model a reduced sediment inflow was used, because the sandbars were over-predicted in the previous models. For a next model, it would be recommended to increase this sediment inflow.
- Apply the approach used in this thesis to other eddy-fan systems in the Marble- and Grand-Canyon reaches.

References

ANDERSON, M. T., GRAF, J. B., MARZOLF, G. R., SURVEY, G. & MONITORING, G. C. 1996. *Controlled Flooding of the Colorado River in Grand Canyon: the Rationale and Data-Collection Planned*, US Geological Survey.

BISSCHOP, F., VISSER, P., VAN RHEE, C. & VERHAGEN, H. J. Year. Erosion due to high flow velocities: A description of relevant processes. *In:* ICCE 2010, 2011 Shanghai. sediment. 24.

BRIDGE, J. S. & BENNETT, S. J. 1992. A model for the entrainment and transport of sediment grains of mixed sizes, shapes, and densities. *Water Resources Research,* 28**,** 337-363.

CELIK, A. O., DIPLAS, P., DANCEY, C. L. & VALYRAKIS, M. 2010. Impulse and particle dislodgement under turbulent flow conditions. *Physics of Fluids,* 22**,** 046601.

DE RUITER, J. 1982. The mechanism of sediment transport on bed forms. *Euromech 156: Mechanics of Sediment Transport.* Istanbul.

DELTARES 2010. Delft3D-FLOW, Simulation of multi-dimensional hydrodynamic flows and transport phenomena, including sediments. Delft.

EINSTEIN, H. A. 1950. The bed-load function for sediment transportation in open channel flows. *Technical Bullitin,* 1026.

HAZEL JR, J. E., GRAMS, P. E., SCHMIDT, J. C. & KAPLINSKI, M. 2010. Sandbar Response in Marble and Grand Canyons, Arizona, Following the 2008 High-Flow Experiment on the Colorado River. *U.S. Geological Survey Scientific Investigations.*

HAZEL JR, J. E., KAPLINSKI, M., PARNELL, R., KOHL, K. & TOPPING, D. J. 2006. Stage-Discharge Relations for the Colorado River in Glen, Marble and Grand Canyons, Arizona 1990-2005. Reston, Verginia.

HOFLAND, B. & BATTJES, J. A. 2006. Probability density function of instantaneous drag forces and shear stresses on a bed. *Journal of Hydraulic Engineering,* 132**,** 1169.

KEMP, L. 2010. *The evolution of sandbars along the Colorado River downstream of the Glen Canyon Dam.* Msc, TU Delft.

KLEINHANS, M. G. & VAN RIJN, L. C. 2002. Stochastic prediction of sediment transport in sand-gravel bed rivers. *Journal of Hydraulic Engineering,* 128**,** 412.

KOCH, F., FLOKSTRA, C. & CONGRESS, I. A. F. H. R. 1980. *Bed level computations for curved alluvial channels*, Delft Hydraulics Laboratory.

LESSER, G. R., ROELVINK, J. A., VAN KESTER, J. A. T. M. & STELLING, G. S. 2004. Development and validation of a three-dimensional morphological model. *Coastal Engineering,* 51**,** 883-915.

LOGAN, B., NELSON, J., MCDONALD, R. & WRIGHT, S. 2010. Mechanics and modeling of flow, sediment transport and morphologic change in riverine lateral separation zones. *2nd Joint Federal Interagency Conference.* Las Vegas.

MASTBERGEN, D. R. 2009. Oeverstabiliteit bij verdieping waterbodems. *Rekenmodel HMBreach.* Delft Cluster.

MASTBERGEN, D. R. & VAN DEN BERG, J. H. 2003. Breaching in fine sands and the generation of sustained turbidity currents in submarine canyons. *Sedimentology,* 50**,** 625-637.

MELIS, T. S. 2010. *2008 High-flow Experiment at Glen Canyon Dam Benefits Colorado River Resources in Grand Canyon National Park*, US Geological Survey.

O'BRIEN, G. & PEDERSON, J. 2008. Geomorphic attributes of 232 cultural sites along the colorado river in Grand Canyon National Park, Arizona. Logan: Department of Geology, Utah State University.

PAPANICOLAOU, A., DIPLAS, P., EVAGGELOPOULOS, N. & FOTOPOULOS, S. 2002. Stochastic incipient motion criterion for spheres under various bed packing conditions. *Journal of Hydraulic Engineering,* 128**,** 369.

RUBIN, D. M., TOPPING, D. J., SCHMIDT, J. C., HAZEL, J., KAPLINSKI, M. & MELIS, T. S. 2002. Recent sediment studies refute Glen Canyon Dam hypothesis. *EOS, Transactions, American Geophysical Union,* 83**,** 273.

SCHMIDT, J. C., GRAMS, P. E. & LESCHIN, M. F. 1999. Variation in the magnitude and style of deposition and erosion in three long (8-12 km) reaches as determined by photographic analysis. *The controlled flood in Grand Canyon,* 1**,** 185-204.

SLOFF, C. J., WRIGHT, S. & KAPLINSKI, M. 2009. High resolution three dimensional modelling of river eddy sandbars, Grand Canyon, U.S.A.. Coastal and Estuarine morphodynamics. *RCEM 2009.* Santa Fe, Argentina.

STRUIKSMA, N. Year. Mathematical modelling of bedload transport over non-erodible layers. *In:* IAHR Symposium on River Coastal and Estuarine Morphodynamics (RCEM), 1999 Genova. 6-10.

TOPPING, D. J. 2009. Type to HAZEL JR, J. E., GRAMS, P. E., SCHMIDT, J. C. & KAPLINSKI, M.

TOPPING, D. J., RUBIN, D., SCHMIDT, J., HAZEL, J., WRIGHT, S., MELIS, T. & KAPLINSKI, M. Year. Comparison of sediment-transport and bar-response results from the 1996 and 2004 controlled-flood experiments on the Colorado River in Grand Canyon. *In:* Eighth Federal Interagency Sedimentation Conference, 2006 Reno, Nevada. 6.

TOPPING, D. J., RUBIN, D. M. & VIERRA JR, L. E. 2000. Colorado River sediment transport 1. Natural sediment supply limitation and the influence of Glen Canyon Dam. *Water Resources Research,* 36**,** 515-542.

TOPPING, D. J. E. A. 2010. Sediment transport during three controlledflood experiments on the Colorado River downstream from Glen Canyon Dam, with implications for eddysandbar deposition in Grand Canyon National Park. Virginia: U.S. Geological Survey.

U.S. DEPARTMENT OF THE INTERIOR 1988. Glen Canyon Environmental Studies final report. Salt Lake City: U.S. Bureau of Reclamation.

USGS. 2011. *USGS Surface-Water Data for the Nation* [Online]. Available: http://waterdata.usgs.gov/nwis/sw [Accessed 2011-06-09 2011].

VAN PROOIJEN, B. & WINTERWERP, J. 2010. A stochastic formulation for erosion of cohesive sediments. *J. Geophys. Res,* 115**,** C01005.

VAN RHEE, C. 2010. Sediment entrainment at high flow velocity. *Journal of Hydraulic Engineering,* 136**,** 572.

VAN RIJN, L. C. 1984. Sediment Transport, Part II: Suspended Load Transport. *Journal of Hydraulic Engineering,* 110**,** 1613-1641.

VAN RIJN, L. C. 1993. *Principles of sediment transport in rivers, estuaries and coastal seas Part I: Edition 1993,* Amsterdam, Aqua Publications.

WRIGHT, S. A. & KAPLINSKI, M. 2011. Flow structures and sandbar dynamics in a canyon river during a controlled flood, Colorado River, Arizona. *Journal of Geophysical Research,* 116**,** F01019.

WU, F. C. & CHOU, Y. J. 2003. Rolling and lifting probabilities for sediment entrainment. *Journal of Hydraulic Engineering,* 129**,** 110.

WU, F. C. & LIN, Y. C. 2002. Pickup probability of sediment under log-normal velocity distribution. *Journal of Hydraulic Engineering,* 128**,** 438.

WU, F. C. & YANG, K. H. 2004. Entrainment probabilities of mixed-size sediment incorporating near-bed coherent flow structures. *Journal of Hydraulic Engineering,* 130**,** 1187.

List of figures

List of tables

Appendix A Delft3D description

This appendix is a description of the used model package Delft3D. The first sections are about the hydrodynamics, the latter sections about the sediment transport.

A.1 Staggered grid in Delft3D

Figure A.1 shows an illustration of the staggered grid in 3D. In the illustration the velocities in x and y direction on the top of the cube are left away because of the clarity of the figure. Also the velocities in the y-direction at the front plane are left away.

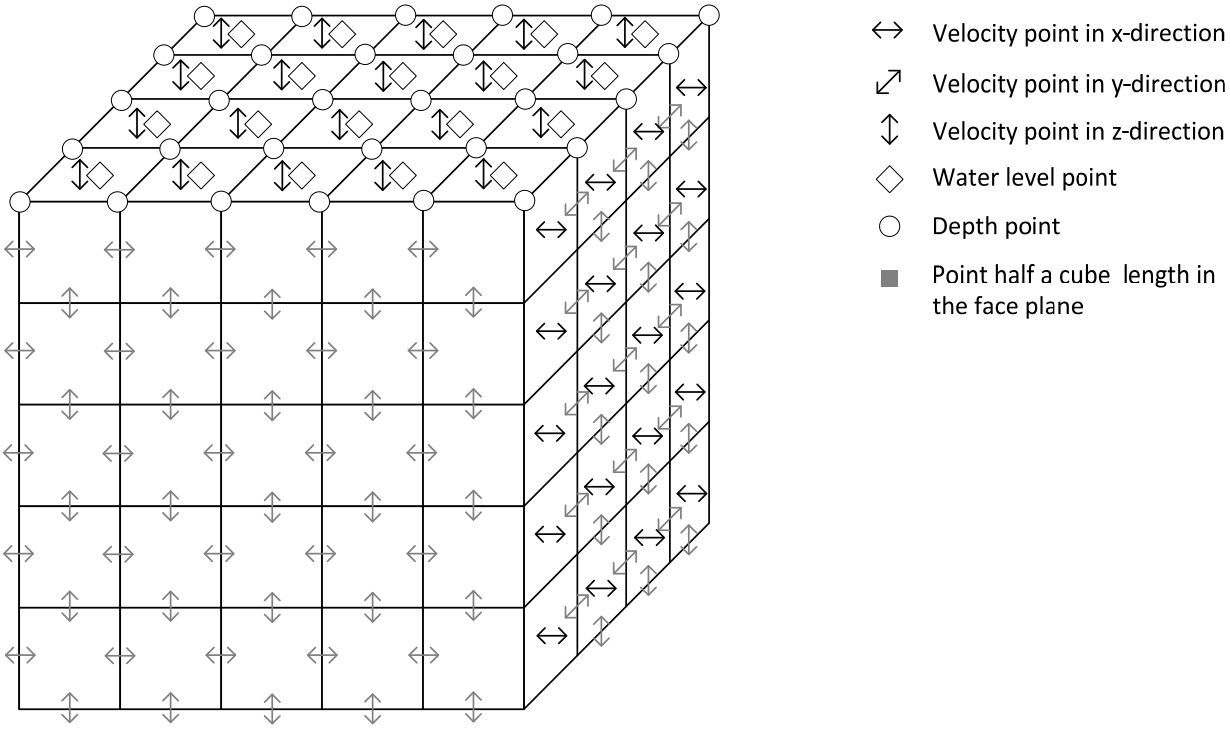

Figure A.1: Staggered grid used in Delft3D

A.2 Sigma coordinate system

The Delft3D model of the Eminence pool and the Willy Taylor pool uses a sigma coordinate system in vertical direction. The sigma grid is fitted to the bottom and to the water surface. Each layer is defined as a fraction of the total water depth (see Figure A.2). The sigma coordinate is expressed as equation (A.1)

$$\sigma = \frac{z - \zeta}{h} \tag{A.1}$$

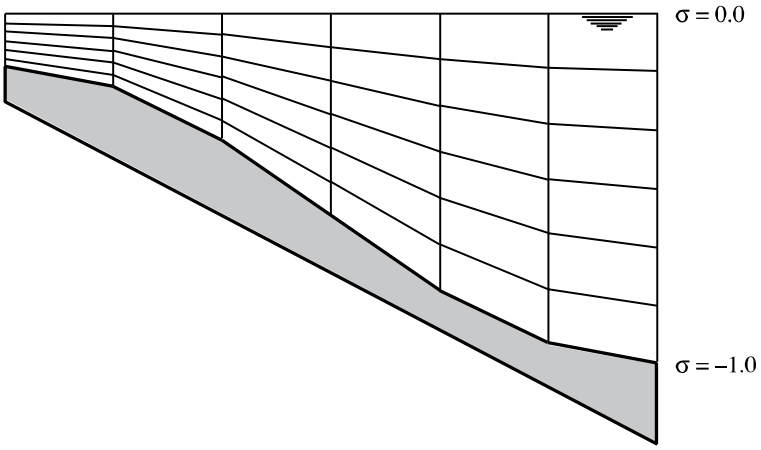

Figure A.2: An illustration of the sigma grid. From (Lesser et al., 2004)

A.3 Equations of motion

The equation of motion consists of two parts: the continuity equation and the momentum equations. For readability, all the equations are written in Cartesian coordinates. Delft3D uses a curvilinear coordinate system. The coefficients: $\sqrt{G_{\xi\xi}}$ and $\sqrt{G_{\eta\eta}}$ are used for this transformation. ξ and η are the horizontal coordinates.

A.3.1 Continuity equation

$$\frac{\partial \rho}{\partial t} + \nabla\left(\rho \vec{u}\right) = 0 \tag{A.2}$$

A.3.2 Momentum equations: Navier-Stokes

Delft3D solves the Navier-Stokes with a few approximations

- Hydrostatic pressure assumption
- Bousinesq approximation
- f-plane approximation
- Reynolds averaging

The full Navier-Stokes equations in a Cartesian coordinate system, assuming the vertical (z) direction coincides with the force of gravity, are:

$$\rho\left(\frac{\partial u}{\partial t} + u\frac{\partial u}{\partial x} + v\frac{\partial u}{\partial y} + w\frac{\partial u}{\partial z}\right) = -\frac{\partial p}{\partial x} + \mu\left(\frac{\partial^2 u}{\partial x^2} + \frac{\partial^2 u}{\partial y^2} + \frac{\partial^2 u}{\partial z^2}\right) + fv \tag{A.3}$$

$$\rho\left(\frac{\partial v}{\partial t} + u\frac{\partial v}{\partial x} + v\frac{\partial v}{\partial y} + w\frac{\partial v}{\partial z}\right) = -\frac{\partial p}{\partial y} + \mu\left(\frac{\partial^2 v}{\partial x^2} + \frac{\partial^2 v}{\partial y^2} + \frac{\partial^2 v}{\partial z^2}\right) - fu \tag{A.4}$$

$$\rho\left(\frac{\partial w}{\partial t} + u\frac{\partial w}{\partial x} + v\frac{\partial w}{\partial y} + w\frac{\partial w}{\partial z}\right) = -\frac{\partial p}{\partial z} + \mu\left(\frac{\partial^2 w}{\partial x^2} + \frac{\partial^2 w}{\partial y^2} + \frac{\partial^2 w}{\partial z^2}\right) + \rho g \tag{A.5}$$

Hydrostatic pressure assumption

In Delft3D the "hydrostatic pressure assumption" is made. The vertical accelerations are not taken into account in the vertical momentum equation. The vertical momentum equation is then simplified to:

$$\frac{\partial p}{\partial z} = \rho g h \tag{A.6}$$

Boussinesq approximation

This approximation assumes the density of the water to be constant, with respect to the depth. This holds for relative shallow areas, such as rivers, but not for ocean trenches of a view kilometre depth. In this thesis a river is modelled, therefore the Boussinesq approximation holds.

f-plane approximation

Large scale water movements are influenced by the rotation of the earth. This is expressed in a force: the Coriolis force. The f-plane approximation assumes a constant Coriolis force over the calculated domain. This model is a small scale model; therefore the f-plane approximation can be used.

Reynolds averaging

The principle of Reynolds averaging is to include small scale turbulence in a larger scale model. The velocity components are split into a time average motion ($\overline{u}$) and a fluctuating part (u'):

$$u = \overline{u} + u' \tag{A.7}$$

After the substitution of (A.7) into the Navier-Stokes equations (A.3) to (A.6), the equations are time averaged.

A.4 k-ε model

To calculate the Reynolds stresses, a turbulence model is needed. The k-ε model is such a model. It calculates the turbulent kinetic energy

The k-ε model without waves from Delft3D manual:

$$\frac{\partial k}{\partial t} + u\frac{\partial k}{\partial x} + v\frac{\partial k}{\partial y} + \frac{w}{d+\zeta}\frac{\partial k}{\partial \sigma} = \frac{1}{\left(d+\zeta\right)^2}\frac{\partial}{\partial \sigma}\left(D_k\frac{\partial k}{\partial \sigma}\right) + P_k + B_k - \varepsilon \tag{A.8}$$

$$\frac{\partial \varepsilon}{\partial t} + u\frac{\partial \varepsilon}{\partial x} + v\frac{\partial \varepsilon}{\partial y} + \frac{w}{d+\zeta}\frac{\partial \varepsilon}{\partial \sigma} = \frac{1}{\left(d+\zeta\right)^2}\frac{\partial}{\partial \sigma}\left(D_\varepsilon\frac{\partial \varepsilon}{\partial \sigma}\right) + P_\varepsilon + B_\varepsilon - c_{2\varepsilon}\frac{\varepsilon^2}{k} \tag{A.9}$$

where

D_k, D_ε turbulent diffusion coefficient for respectively turbulent kinetic energy and dissipation

P_k, P_ε production of respectively turbulent kinetic energy and dissipation

B_k, B_ε Buoyancy effect of respectively turbulent kinetic energy and dissipation

With the turbulent kinetic energy and the dissipation the turbulent viscosity can be calculated:

$$\nu_t = c_\mu\frac{k^2}{\varepsilon} \tag{A.10}$$

A.5 Bottom boundary condition

A.5.1 Velocity

On sub-grid level in the bottom layer a logarithmic velocity profile used in Delft3D. This velocity profile can be derived from the definition of the shear velocity of equation(A.11).

$$u_* = \sqrt{\frac{\tau_b}{\rho_w}} = \kappa z\frac{\partial u}{\partial z} \tag{A.11}$$

When equation(A.11) is integrated one gets:

$$u\left(z\right) = \frac{u_*}{\kappa}\ln\left(z\right) + C \tag{A.12}$$

To calculate the integration constant C, a boundary condition is needed:

$$u\left(z_0\right) = 0 \tag{A.13}$$

With this boundary condition the standard logarithmic profile is obtained. This profile is defined from z_0 to $H + z_0$.

$$u\left(z\right) = \frac{u_*}{\kappa}\ln\left(\frac{z}{z_0}\right) \in \left[z_0, H + z_0\right] \tag{A.14}$$

In Delft3D the vertical profile is defined from 0 to H, therefore equation (A.14) has to be transformed to a new coordinate $\tilde{z}$, where

$$\tilde{z} = z - z_0 \Rightarrow z = \tilde{z} + z0 \tag{A.15}$$

Substituting equation (A.15) into equation (A.14), the following equation is obtained:

$$u\left(\tilde{z}\right) = \frac{u_*}{\kappa}\ln\left(\frac{\tilde{z} + z_0}{z_0}\right) \in \left[0, H\right] \tag{A.16}$$

The bed velocity in Delft3D is defined between the middle of the bottom and the layer closest to the bottom.

$$\tilde{z} = \tfrac{1}{2}\Delta z_b \tag{A.17}$$

With this definition the logarithmic profile used in Delft3D is obtained:

$$u_b = u\left(\tfrac{1}{2}\Delta z_b\right) = \frac{u_*}{\kappa}\ln\left(1 + \frac{\Delta z_b}{2z_0}\right) \tag{A.18}$$

A.5.2 Turbulent kinetic energy and dissipation

The production and dissipation of turbulent kinetic energy at the bed is assumed to be in equilibrium. This leads to the Dirichlet boundary conditions at the bed:

$$k_{bed} = \frac{u_*^2}{\sqrt{c_\mu}} \tag{A.19}$$

$$\varepsilon_{bed} = \frac{u_*^3}{\kappa\, z_0} \tag{A.20}$$

At the surface the turbulent kinetic energy and the dissipation is set to zero.

A.6 Sediment entrainment

To calculate the sediment entrainment, Delft3D uses a calculated reference sediment concentration on the reference level defined by (van Rijn, 1984). Figure A.3 shows the different layers from the bottom. The layers below or at the concentration reference level (a) are set equal to this reference concentration. In the kmx-layer the sinks and sources are calculated. In the layers above an advection diffusion equation is used for the calculation of the sediment concentrations.

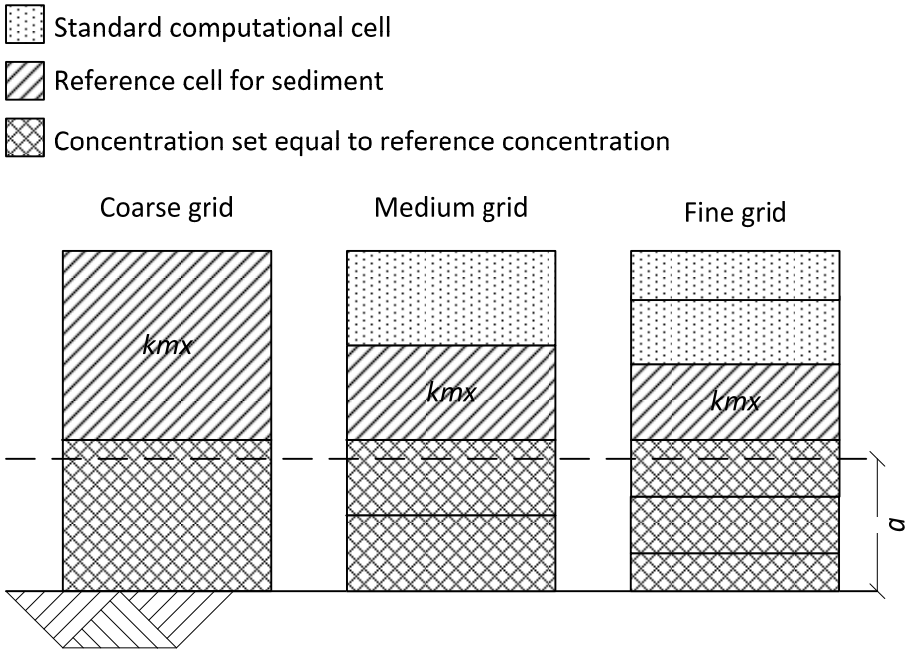

Figure A.3: Reference layer in Delft3D for different vertical grid densities. Based upon (Deltares, 2010)

The sub-grid concentration from the kmx-layer to the bottom is assumed to be described by a Rouse profile:

$$c = c_{ref}\left(\frac{a(h-z)}{z(h-a)}\right)^{A} \tag{A.21}$$

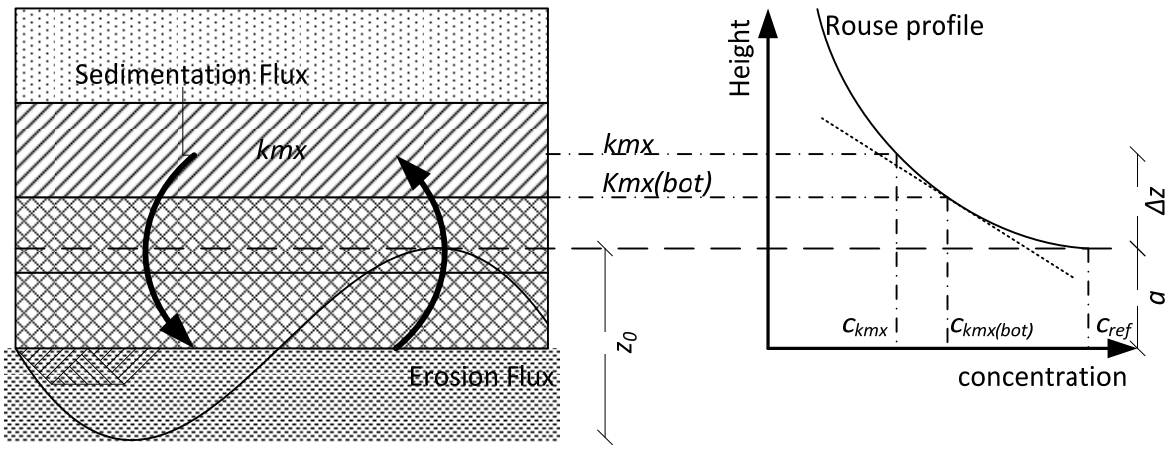

Figure A.4: Approximation of the concentration and concentration gradient at the bottom of the kmx-layer. Based upon (Deltares, 2010)

Figure A.4 shows the locations of the reference level, the kmx-layer and the bottom of the kmx-layer and the corresponding concentrations. The c_{kmx} is calculated using the advection-diffusion equation in the whole water column. The c_{ref} is calculated using an entrainment function. Now the only unknown parameter (A) can be calculated.

$$c_{kmx} = c_{ref}\left(\frac{a\left(h - z_{kmx}\right)}{z_{kmx}\left(h - a\right)}\right)^{A} \Rightarrow A = \frac{\ln\left(\frac{c_{kmx}}{c_a}\right)}{\ln\left(\frac{a\left(h - z_{kmx}\right)}{z_{kmx}\left(h - a\right)}\right)} \tag{A.22}$$

Delft3D also calculates the concentration at the bottom of the kmx-layer from the reference concentration:

$$c_{kmx(bot)} = c_{ref}\left(\frac{a\left(h - z_{kmx(bot)}\right)}{z_{kmx(bot)}\left(h - a\right)}\right)^{A} \tag{A.23}$$

This is expressed as a correction factor times the concentration in the middle of the kmx-layer:

$$c_{kmx(bot)} = \alpha_1 c_{kmx} \tag{A.24}$$

Where:

α_1 Is equal to $c_{kmx(bot)} \big/ c_{kmx}$

The concentration gradient at the bottom of the kmx-layer is found by differentiating equation (A.23) with respect to *z*:

$$\frac{\partial c}{\partial z_{kmx(bot)}} = A c_{ref}\left(\frac{a\left(h - z_{kmx(bot)}\right)}{z_{kmx(bot)}\left(h - a\right)}\right)^{A-1} \cdot \left(\frac{-ah}{z_{kmx(bot)}^2\left(h - a\right)}\right) \tag{A.25}$$

Equation (A.25) can be approximated using finite differences and a correction factor:

$$\frac{\partial c}{\partial z_{kmx(bot)}} = \alpha_2 \frac{c_{kmx} - c_{ref}}{\Delta z} \tag{A.26}$$

The diffusive erosion becomes:

$$E = -\varepsilon_s \frac{\partial c}{\partial z_{kmx(bot)}} \approx -\alpha_2 \varepsilon_s \frac{c_{kmx} - c_{ref}}{\Delta z} = \alpha_2 \varepsilon_s \frac{c_{ref}}{\Delta z} - \alpha_2 \varepsilon_s \frac{c_{kmx}}{\Delta z} \tag{A.27}$$

The sedimentation is the fall velocity times the concentration:

$$S = w_s c_{kmx(bot)} \approx \alpha_1 w_s c_{kmx} \tag{A.28}$$

The total source and sink of the kmx-layer are:

$$\text{Source} = \alpha_2 \varepsilon_s \frac{c_{ref}}{\Delta z} \tag{A.29}$$

$$\text{Sink} = \alpha_2 \varepsilon_s \frac{c_{kmx}}{\Delta z} + \alpha_1 w_s c_{kmx} \tag{A.30}$$

Appendix B New formulation for sediment transport

B.1 Triangular distribution

A classical triangular distribution has three parameters

$$Tri\left(a,b,c\right) \tag{B.1}$$

Where a and b are the bounds of the distribution and c is the mode of the distribution. When a normal distribution is approximated the triangular distribution should be symmetrical just like the normal distribution. The a and b parameters of equation (B.1) should be of equal distance from the mode of the distribution (equation (B.2)).

$$Tri\left(\overline{u}-a,\overline{u}+a,\overline{u}\right) \tag{B.2}$$

The variance of this distribution is:

$$\mathrm{var}=\frac{a^2}{6} \tag{B.3}$$

The corresponding standard deviation is

$$\sigma_u=\sqrt{\mathrm{var}}=\sqrt{\frac{a^2}{6}} \tag{B.4}$$

The a parameter of equation (B.4) can be expressed in terms of sigma

$$a=\sqrt{6}\,\sigma_u \tag{B.5}$$

With these modifications the PDF of the triangular distribution becomes

$$f_u=\frac{\sigma_u}{\sqrt{6}}-\frac{\left|u-\overline{u}\right|}{6\,\sigma_u} \tag{B.6}$$

B.2 Probabilistic representation of the Van Rijn transport parameter

Figure B.1 shows six different solutions for the two integrals of equation (B.7) represented in the six boxes

$$\int_{ucr'}^{\overline{u}+\sqrt{6}\,\sigma(u)} T\left(u_i\right)\cdot P\left(u_i\right)du_i+\int_{\overline{u}-\sqrt{6}\,\sigma(u)}^{-ucr'} T\left(u_i\right)\cdot P\left(u_i\right)du \tag{B.7}$$

$$T\left(u_i\right)\cdot P\left(u_i\right)=\begin{cases}0 & u\le\overline{u}-\sqrt{6}\,\sigma_u\\ \left(\dfrac{\mu_c\cdot u^2-u_{cr}^2}{u_{cr}^2}\right)\left(\dfrac{1}{\sqrt{6}\,\sigma_u}-\dfrac{\overline{u}-u}{6\,\sigma_u^2}\right) & \overline{u}-\sqrt{6}\,\sigma_u<u\le\overline{u}\\ \left(\dfrac{\mu_c\cdot u^2-u_{cr}^2}{u_{cr}^2}\right)\left(\dfrac{1}{\sqrt{6}\,\sigma_u}+\dfrac{\overline{u}-u}{6\,\sigma_u^2}\right) & \overline{u}<u\le\overline{u}+\sqrt{6}\,\sigma_u\\ 0 & u>\overline{u}+\sqrt{6}\,\sigma_u\end{cases} \tag{B.8}$$

In Figure B.1 T^+ stands for the left side of equation (B.7). This represents the contribution of velocities in positive direction. T^- is the left side of equation (B.7), which are the contributions of the velocities in negative, counter-stream wise direction.

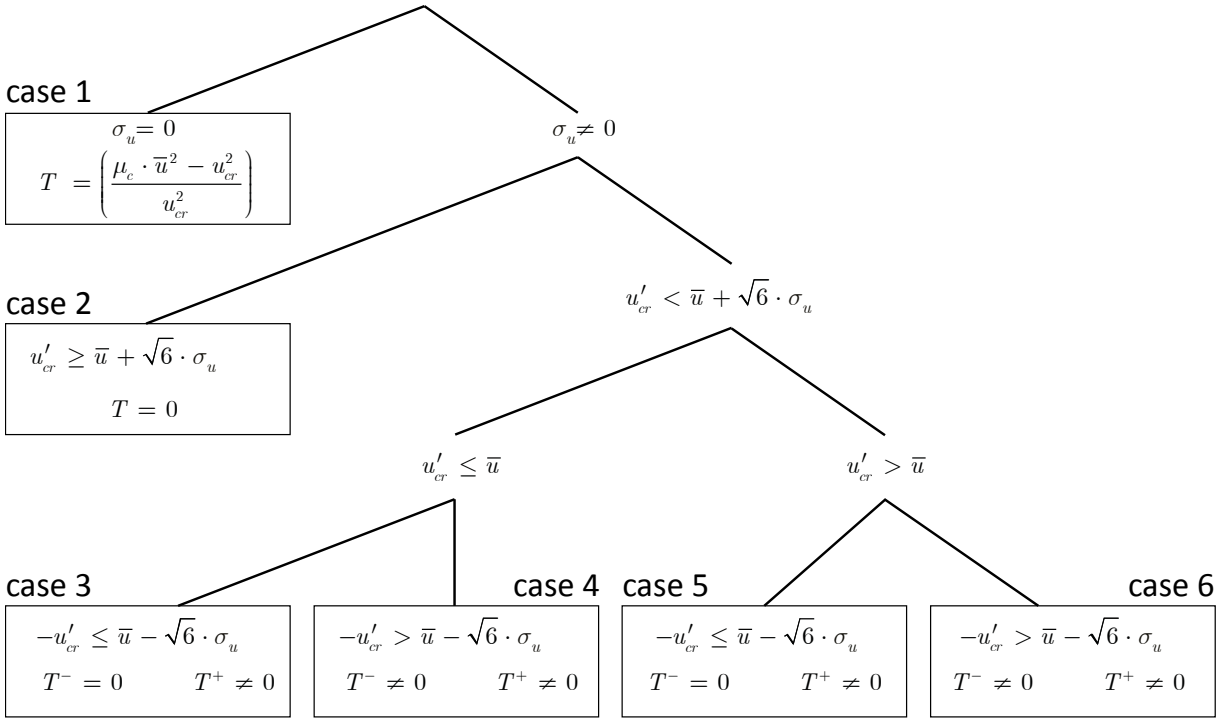

Figure B.1: schematic representation of the possible solutions of the integral of the transport parameter T

Starting at the top, there is the possibility the standard deviation is equal to zero (case 1). In this case no turbulence is present. The consequence is a deterministic expression for T. The top right branch represents the probabilistic cases. When the critical velocity needed for entrainment is higher than the upper bound of the PDF ($u'_{cr} \geq \overline{u} + \sqrt{6}\,\sigma_u$) there is no entrainment (case 2). The probability is zero in that case. When a distribution on the domain of $[-\infty, \infty]$ would have been used, there would be some entrainment, but due to the low probabilities of occurrence it would have been very small.

In the third and fifth case the contributions of the negative velocities are zero. The lower bound of the PDF is larger than the negative velocity needed for entrainment ($-u'_{cr} \leq \overline{u} - \sqrt{6}\,\sigma_u$). The probability that these velocities occur are therefore equal to zero. In case 3 the critical velocity is smaller than the mean velocity in case 5 it is the other way around. The triangular distribution is a piecewise function and therefore its integral is too. The value of the integral is described on a different part of the piecewise function for case 3 and 5.

Case 4 and 6 do have contributions of the negative velocities on the calculation of T. In these cases the lower bound of the PDF is smaller than the negative critical velocity ($-u'_{cr} > \overline{u} - \sqrt{6}\,\sigma_u$). The difference between case 4 and 6 is the same as for 3 and 5: in case 4 the critical velocity is smaller than the mean velocity in case 6 it is larger.

B.2.1 Reference concentration for suspended transport

The probabilistic suspended sediment formulation with a triangular distribution is:

$$\int_{ucr'}^{\overline{u}+\sqrt{6}\,\sigma(u)} T\left(u_i\right)^{1.5} \cdot P\left(u_i\right) du_i + \int_{\overline{u}-\sqrt{6}\,\sigma(u)}^{-ucr'} T\left(u_i\right)^{1.5} \cdot P\left(u_i\right) du \tag{B.9}$$

Where:

$$T\left(u\right)^{1.5}\cdot P\left(u\right)=\begin{cases}0 & u\le \overline{u}-\sqrt{6}\,\sigma_u\\ \left(\dfrac{\mu_c\cdot u^2-u_{cr}^2}{u_{cr}^2}\right)^{1.5}\left(\dfrac{1}{\sqrt{6}\,\sigma_u}-\dfrac{\overline{u}-u}{6\,\sigma_u^2}\right) & \overline{u}-\sqrt{6}\,\sigma_u<u\le\overline{u}\\ \left(\dfrac{\mu_c\cdot u^2-u_{cr}^2}{u_{cr}^2}\right)^{1.5}\left(\dfrac{1}{\sqrt{6}\,\sigma_u}+\dfrac{\overline{u}-u}{6\,\sigma_u^2}\right) & \overline{u}<u\le\overline{u}+\sqrt{6}\,\sigma_u\\ 0 & u>\overline{u}+\sqrt{6}\,\sigma_u\end{cases} \tag{B.10}$$

The solution of the indefinite integral of equation (B.9) is just like equation (B.10) defined on four intervals

For $u\le\overline{u}-\sqrt{6}\,\sigma_u$, $T\left(u\right)^{1.5}\cdot P\left(u\right)=0$

For $\overline{u}-\sqrt{6}\,\sigma_u<u\le\overline{u}$

$$\begin{aligned}f_1=&\frac{1}{16}\frac{u_{cr}\sqrt{6}\ln\left(\sqrt{\mu_c}u+\sqrt{\mu_c u^2-u_{cr}^2}\right)}{\sqrt{\mu_c}\sigma_u}-\frac{1}{16}\frac{u_{cr}\sqrt{6}\ln\left(\sqrt{\mu_c}\overline{u}-\sqrt{\mu_c}\sqrt{6}\sigma_u+A\right)}{\sqrt{\mu_c}\sigma_u}-\\&-\frac{9}{40}\frac{A}{u_{cr}}-\frac{1}{24}\frac{\mu_c\ \overline{u}\ u^3\sqrt{\mu_c u^2-u_{cr}^2}}{u_{cr}^3\ \sigma_u^2}-\frac{1}{15}\frac{\sqrt{\mu_c u^2-u_{cr}^2}u^2}{u_{cr}\sigma_u^2}+\frac{3}{10}\frac{\mu_c A\overline{u}^2}{u_{cr}^3}-\frac{3}{80}\frac{\overline{u}^2A}{u_{cr}\sigma_u^2}+\\&+\frac{1}{16}\frac{u_{cr}\overline{u}\ln\left(\sqrt{\mu_c}\overline{u}-\sqrt{\mu_c}\sqrt{6}\ \sigma_u+A\right)}{\sqrt{\mu_c}\sigma^2}+\frac{1}{30}\frac{\mu_c\sqrt{\mu_c u^2-u_{cr}^2}u^4}{u_{cr}^3\sigma^2}+\frac{3}{10}\frac{\mu_c\sigma_u^2A}{u_{cr}^3}+\frac{1}{120}\frac{\mu_c\overline{u}^4A}{u_{cr}^3\sigma_u^2}\\&-\frac{5}{48}\frac{\sqrt{6}u\sqrt{\mu_c u^2-u_{cr}^2}}{u_{cr}\sigma_u}+\frac{3}{40}\frac{\overline{u}A\sqrt{6}}{u_{cr}\sigma_u}+\frac{1}{30}\frac{u_{cr}\sqrt{\mu_c u^2-u_{cr}^2}}{\mu_c\sigma_u^2}-\frac{1}{30}\frac{u_{cr}A}{\mu_c\sigma_u^2}-\\&-\frac{1}{16}\frac{u_{cr}\overline{u}\ln\left(\sqrt{\mu_c}u+\sqrt{\mu_c u^2-u_{cr}^2}\right)}{\sqrt{\mu_c}\sigma_u^2}+\frac{5}{48}\frac{\overline{u}\ u\sqrt{\mu_c u^2-u_{cr}^2}}{u_{cr}\sigma_u^2}+\frac{1}{24}\frac{\mu_c\sqrt{6}\ u^3\sqrt{\mu_c t^2-u_{cr}^2}}{u_{cr}^3\sigma_u}-\\&-\frac{1}{5}\frac{\mu_c\sigma_u A\ \overline{u}\ \sqrt{6}}{u_{cr}^3}-\frac{1}{30}\frac{\mu_c u^3A\sqrt{6}}{u_{cr}^3\sigma_u}\end{aligned} \tag{B.11}$$

Where

$$A=\sqrt{-2\ \mu_c\ \overline{u}\ \sqrt{6}\ \sigma_u+6\,\mu_c\ \sigma_u^2-u_{cr}^2+\mu_c\ \overline{u}^2} \tag{B.12}$$

For $\overline{u}<u\le\overline{u}+\sqrt{6}\,\sigma_u$

$$f_2 = \frac{3}{40}\frac{\overline{u}A\sqrt{6}}{u_{cr}\,\sigma_u}\sigma_u - \frac{5}{48}\frac{\sqrt{6}\;u\sqrt{\mu_c u^2 - u_{cr}^2}}{u_{cr}\,\sigma_u} - \frac{1}{30}\frac{\mu_c\sqrt{\mu_c u^2 - u_{cr}^2}\,u^4}{u_{cr}^3\;\sigma_u^2} - \frac{1}{60}\frac{\mu_c\,\overline{u}^4\sqrt{\mu_c\overline{u} - u_{cr}^2}}{u_{cr}^3\;\sigma_u^2}$$
$$+\frac{1}{16}\frac{u_{cr}\,\overline{u}\ln\left(\sqrt{\mu_c}\,\overline{u} - \sqrt{\mu_c}\sqrt{6}\;\sigma_u + A\right)}{\sqrt{\mu_c}\;\sigma_u^2} + \frac{1}{16}\frac{u_{cr}\,\overline{u}\;\ln\left(\sqrt{\mu_c}u + \sqrt{\mu_c u^2 - u_{cr}^2}\right)}{\sqrt{\mu_c}\;\sigma_u^2}$$
$$-\frac{1}{8}\frac{u_{cr}\,\overline{u}\;\ln\left(\sqrt{\mu_c}\,\overline{u} + \sqrt{\mu_c\overline{u} - u_{cr}^2}\right)}{\sqrt{\mu_c}\;\sigma_u^2} - \frac{3}{80}\frac{\overline{u}^2 A}{u_{cr}\;\sigma_u^2} - \frac{9}{40}\frac{A}{u_{cr}} + \frac{3}{40}\frac{\mu^2\sqrt{\mu_c\overline{u} - u_{cr}^2}}{u_{cr}\;\sigma_u^2} + \frac{3}{10}\frac{\mu_c A\overline{u}^2}{u_{cr}^3}$$
$$+\frac{1}{24}\frac{\mu_c\,\overline{u}u^3\sqrt{\mu_c u^2 - u_{cr}^2}}{u_{cr}^3\;\sigma_u^2} + \frac{1}{15}\frac{\sqrt{\mu_c u^2 - u_{cr}^2}\,u^2}{u_{cr}\;\sigma_u^2} - \frac{1}{16}\frac{u_{cr}\sqrt{6}\ln\left(\sqrt{\mu_c}\,\overline{u} - \sqrt{\mu_c}\sqrt{6}\;\sigma_u + A\right)}{\sqrt{\mu_c}\;\sigma_u}$$
$$+\frac{1}{16}\frac{u_{cr}\sqrt{6}\ln\left(\sqrt{\mu_c}u + \sqrt{\mu_c u^2 - u_{cr}^2}\right)}{\sqrt{\mu_c}\;\sigma_u} - \frac{5}{48}\frac{\overline{u}u\sqrt{\mu_c u^2 - u_{cr}^2}}{u_{cr}\;\sigma_u^2} - \frac{1}{5}\frac{\mu_c\sigma_u A\;\overline{u}\sqrt{6}}{u_{cr}^3} - \frac{1}{30}\frac{\mu_c\,\overline{u}^3 A\sqrt{6}}{u_{cr}^3\;\sigma_u}$$
$$+\frac{1}{24}\frac{\mu_c\sqrt{6}\;u^3\sqrt{\mu_c u^2 - u_{cr}^2}}{u_{cr}^3\;\sigma_u} - \frac{1}{30}\frac{u_{cr}\left(A + \sqrt{\mu_c u^2 - u_{cr}^2} - 2\sqrt{\mu_c\overline{u} - u_{cr}^2}\right)}{\mu_c\sigma_u^2}$$
$$+\frac{3}{10}\frac{\mu_c\sigma_u^2 A}{u_{cr}^3} + \frac{1}{120}\frac{\mu_c\,\overline{u}^4 A}{u_{cr}^3\;\sigma_u^2} \qquad \text{(B.13)}$$

For $u \geq \overline{u} + \sqrt{6}\,\sigma_u$

$$B = \sqrt{2\;\mu_c\;\overline{u}\;\sqrt{6}\,\sigma_u + 6\;\mu_c\;\sigma_u^2 - u_{cr}^2 + \mu_c\;\overline{u}^2} \qquad \text{(B.14)}$$

$$f_3 = -\frac{3}{40}\frac{\overline{u}B\sqrt{6}}{u_{cr}\,\sigma_u} + \frac{3}{10}\frac{\mu_c\sigma_u^2 B}{u_{cr}^3} + \frac{1}{120}\frac{\mu_c\,\overline{u}^4 B}{u_{cr}^3\;\sigma_u^2} + \frac{1}{5}\frac{\mu_c\,\overline{u}\sigma_u\sqrt{B}\sqrt{6}}{u_{cr}^3} + \frac{1}{30}\frac{\mu_c\,\overline{u}^3 B\sqrt{6}}{u_{cr}^3\sigma_u} - \frac{1}{60}\frac{\mu_c\,\overline{u}^4\sqrt{\mu_c\overline{u} - u_{cr}^2}}{u_{cr}^3\;\sigma_u^2} +$$
$$+\frac{1}{6}\frac{u_{cr}\sqrt{6}\ln\left(\sqrt{\mu_c}\,\overline{u} + \sqrt{\mu_c}\sqrt{6}\;\sigma_u + B\right)}{\sigma_u\sqrt{\mu_c}} - \frac{3}{80}\frac{\overline{u}^2 B}{u_{cr}\sigma_u^2} + \frac{3}{10}\frac{\mu_c B\overline{u}^2}{u_{cr}^3} - \frac{1}{8}\frac{u_{cr}\,\overline{u}\ln\left(\sqrt{\mu_c}\,\overline{u} + \sqrt{\mu_c\overline{u} - u_{cr}^2}\right)}{\sigma_u^2\sqrt{\mu_c}}$$
$$+\frac{3}{40}\frac{\overline{u}^2\sqrt{\mu_c\overline{u} - u_{cr}^2}}{u_{cr}\sigma^2} + \frac{1}{16}\frac{u_{cr}\,\overline{u}\ln\left(\sqrt{\mu_c}\,\overline{u} + \sqrt{\mu_c}\sqrt{6}\;\sigma_u + B\right)}{\sigma_u^2\sqrt{\mu_c}} + \frac{3}{40}\frac{\overline{u}A\sqrt{6}}{u_{cr}\,\sigma_u} - \frac{1}{5}\frac{\sigma_u\mu_c A\overline{u}\sqrt{6}}{u_{cr}^3} - \frac{1}{30}\frac{\mu_c\,\overline{u}^3 A\sqrt{6}}{u_{cr}^3\sigma_u}$$
$$-\frac{9}{40}\frac{A}{u_{cr}} + \frac{3}{10}\frac{\mu_c\sigma_u^2 A}{u_{cr}^3} - \frac{1}{30}\frac{u_{cr}A}{\mu_c\;\sigma_u^2} - \frac{3}{80}\frac{\overline{u}^2 A}{u_{cr}\,\sigma_u} + \frac{3}{10}\frac{\mu_c A\overline{u}^2}{u_{cr}^3} + \frac{1}{16}\frac{u_{cr}\,\overline{u}\ln\left(\sqrt{\mu_c}\,\overline{u} - \sqrt{\mu_c}\sqrt{6}\;\sigma_u + A\right)}{\sigma_u^2\sqrt{\mu_c}}$$
$$+\frac{1}{120}\frac{\mu_c\,\overline{u}^4 A}{u_{cr}^3\;\sigma_u^2} - \frac{1}{16}\frac{u_{cr}\sqrt{6}\ln\left(\sqrt{\mu_c}\,\overline{u} - \sqrt{\mu_c}\sqrt{6}\;\sigma_u + A\right)}{\sqrt{\mu_c}} - \frac{1}{30}\frac{u_{cr}B}{\mu_c\;\sigma_u^2} + \frac{1}{15}\frac{u_{cr}\sqrt{\mu_c\overline{u} - u_{cr}^2}}{\mu_c\;\sigma_u^2} - \frac{9}{40}\frac{B}{u_{cr}}$$

(B.15)

When one would use the boundaries of the integral, one gets the solution

For case 3 in Figure B.1 equation (B.16) is the solution

$$f_3 - f_1\left(\frac{1}{\sqrt{\mu_c}}u_{cr}\right) \qquad \text{(B.16)}$$

When these are used the solution for the integral of $T(u)^{1.5} \cdot P(u)$ for the domain $-u'_{cr} \le \overline{u} - \sqrt{6}\,\sigma_u$ becomes equation (B.17)

$$\begin{aligned}
&\frac{3}{10}\frac{\mu_c \sigma_u^2 B}{u_{cr}^3} - \frac{1}{30}\frac{u_{cr} B}{\mu_c \sigma_u^2} + \frac{1}{120}\frac{\mu_c B \overline{u}^4}{u_{cr}^3 \sigma_u^2} - \frac{1}{60}\frac{\mu_c \overline{u}^4 \sqrt{-u_{cr}^2 + \mu_c \overline{u}^2}}{u_{cr}^3 \sigma_u^2} + \frac{1}{15}\frac{u_{cr}\sqrt{-u_{cr}^2 + \mu_c \overline{u}^2}}{\mu_c \sigma_u^2} \\
&-\frac{3}{40}\frac{\overline{u} B\sqrt{6}}{u_{cr}\sigma_u} + \frac{1}{16}\frac{u_{cr}\sqrt{6}\ln\left(\sqrt{\mu_c}\overline{u} + \sqrt{\mu_c}\sqrt{6}\sigma_u + B\right)}{\sigma_u\sqrt{\mu_c}} + \frac{1}{30}\frac{\mu_c \overline{u}^3 B\sqrt{6}}{u_{cr}^3\sigma_u} + \frac{1}{5}\frac{\mu_c \overline{u}\sigma_u B\sqrt{6}}{u_{cr}^3} \\
&-\frac{1}{16}\frac{u_{cr}\sqrt{6}\ln\left(u_{cr}\right)}{\sigma\sqrt{\mu_c}} - \frac{1}{8}\frac{u_{cr}\overline{u}\ln\left(\sqrt{\mu_c}\overline{u} + \sqrt{-u_{cr}^2 + \mu_c\overline{u}^2}\right)}{\sigma_u^2\sqrt{\mu_c}} + \frac{3}{40}\frac{\overline{u}^2\sqrt{-u_{cr}^2 + \mu_c\overline{u}^2}}{u_{cr}\,\sigma_u^2} \\
&-\frac{3}{80}\frac{\overline{u}^2 B}{u_{cr}\,\sigma_u^2} - \frac{9}{40}\frac{B}{u_{cr}} + \frac{1}{16}\frac{u_{cr}\overline{u}\ln\left(\sqrt{\mu_c}\overline{u} + \sqrt{\mu_c}\sqrt{6}\,\sigma_u + B\right)}{\sigma_u^2\sqrt{\mu_c}} + \frac{3}{10}\frac{\mu_c B\overline{u}^2}{u_{cr}^3} + \frac{1}{16}\frac{u_{cr}\overline{u}\ln\left(u_{cr}\right)}{\sigma_u^2\sqrt{\mu_c}}
\end{aligned} \tag{B.17}$$

For case 4 in Figure B.1 equation (B.18) is the solution

$$f_3 - f_1\left(\frac{1}{\sqrt{\mu_c}}u_{cr}\right) + f_1\left(-\frac{1}{\sqrt{\mu_c}}u_{cr}\right) \tag{B.18}$$

When these are used the solution for the integral of $T(u)^{1.5} \cdot P(u)$ for the domain $-u'_{cr} > \overline{u} - \sqrt{6}\,\sigma_u$ becomes equation (B.19)

$$\begin{aligned}
&\frac{1}{120}\frac{\mu_c B\overline{u}^4}{u_{cr}^3\sigma_u^2} - \frac{1}{60}\frac{\mu_c\overline{u}^4\sqrt{-u_{cr}^2 + \mu_c\overline{u}^2}}{u_{cr}^3\sigma_u^2} + \frac{1}{16}\frac{u_{cr}\sqrt{6}\ln\left(\sqrt{\mu_c}\overline{u} + \sqrt{\mu_c}\sqrt{6}\sigma_u + B\right)}{\sigma_u\sqrt{\mu_c}} - \frac{1}{16}\frac{u_{cr}\sqrt{6}\ln\left(u_{cr}\right)}{\sigma\sqrt{\mu_c}} - \\
&\frac{1}{8}\frac{u_{cr}\overline{u}\ln\left(\sqrt{\mu_c}\overline{u} + \sqrt{-u_{cr}^2 + \mu_c\overline{u}^2}\right)}{\sigma_u^2\sqrt{\mu_c}} + \frac{3}{40}\frac{\overline{u}^2\sqrt{-u_{cr}^2 + \mu_c\overline{u}^2}}{u_{cr}\,\sigma_u^2} - \frac{3}{80}\frac{\overline{u}^2 B}{u_{cr}\,\sigma_u^2} + \\
&\frac{1}{16}\frac{u_{cr}\overline{u}\ln\left(\sqrt{\mu_c}\overline{u} + \sqrt{\mu_c}\sqrt{6}\,\sigma_u + B\right)}{\sigma_u^2\sqrt{\mu_c}} + \frac{3}{10}\frac{\mu_c B\overline{u}^2}{u_{cr}^3} + \frac{1}{16}\frac{u_{cr}\overline{u}\ln\left(u_{cr}\right)}{\sigma_u^2\sqrt{\mu_c}} - \frac{9}{40}\frac{A}{u_{cr}} - \\
&\frac{1}{30}\frac{u_{cr}A}{\mu_c\sigma_u^2} + \frac{3}{40}\frac{\overline{u}A\sqrt{6}}{u_{cr}\sigma_u} - \frac{1}{5}\frac{\sigma_u\mu_c A\overline{u}\sqrt{6}}{u_{cr}^3} - \frac{1}{30}\frac{muc\mu^3 A\sqrt{6}}{tr^3\sigma} + \frac{3}{10}\frac{\mu_c\sigma_u^2 A}{u_{cr}^3} \\
&-\frac{1}{16}\frac{u_{cr}\sqrt{6}\ln\left(\sqrt{\mu_c}\overline{u} + \sqrt{\mu_c}\sqrt{6}\sigma_u + A\right)}{\sigma_u\sqrt{\mu_c}} + \frac{1}{16}\frac{u_{cr}\overline{u}\ln\left(\sqrt{\mu_c}\overline{u} + \sqrt{\mu_c}\sqrt{6}\,\sigma_u + A\right)}{\sigma_u^2\sqrt{\mu_c}} + \frac{3}{10}\frac{\mu_c A\overline{u}^2}{u_{cr}^3} - \\
&\frac{3}{80}\frac{\overline{u}^2 A}{u_{cr}\,\sigma_u^2} + \frac{1}{120}\frac{\mu_c A\overline{u}^4}{u_{cr}^3\sigma_u^2} + \frac{1}{16}\frac{u_{cr}\sqrt{6}\ln\left(u_{cr}\right)}{\sigma_u\sqrt{\mu_c}} - \frac{1}{16}\frac{u_{cr}\overline{u}\ln\left(u_{cr}\right)}{\sigma_u^2\sqrt{\mu_c}} - \\
&\frac{3}{40}\frac{\overline{u}B\sqrt{6}}{u_{cr}\sigma_u} + \frac{1}{30}\frac{\mu_c\overline{u}^3 B\sqrt{6}}{u_{cr}^3\sigma_u} + \frac{1}{5}\frac{\mu_c\overline{u}\sigma_u B\sqrt{6}}{u_{cr}^3} + \\
&\frac{3}{10}\frac{\mu_c\sigma_u^2 B}{u_{cr}^3} - \frac{1}{30}\frac{u_{cr}B}{\mu_c\sigma_u^2} + \frac{1}{15}\frac{u_{cr}\sqrt{-u_{cr}^2 + \mu_c\overline{u}^2}}{\mu_c\sigma_u^2} - \frac{9}{40}\frac{B}{u_{cr}}
\end{aligned} \tag{B.19}$$

For case 5 in Figure B.1 equation (B.20) is the solution

$$f_3 - f_2\left(\frac{1}{\sqrt{\mu_c}}u_{cr}\right) \tag{B.20}$$

When these values are substituted (B.21) is obtained

$$\begin{aligned}
&-\frac{3}{40}\frac{\overline{u}B\sqrt{6}}{u_{cr}\sigma_u} - \frac{1}{30}\frac{u_{cr}B}{\mu_c\sigma_u^2} + \frac{1}{120}\frac{\mu_c B\overline{u}^4}{u_{cr}^3\sigma_u^2} + \frac{1}{16}\frac{u_{cr}\overline{u}\ln\left(\sqrt{\mu_c}\overline{u} + \sqrt{\mu_c}\sqrt{6}\,\sigma_u + B\right)}{\sigma_u^2\sqrt{\mu_c}} \\
&-\frac{9}{40}\frac{B}{u_{cr}} + \frac{3}{10}\frac{\mu_c B\overline{u}^2}{u_{cr}^3} - \frac{3}{80}\frac{\overline{u}^2 B}{u_{cr}\,\sigma_u^2} - \frac{1}{16}\frac{u_{cr}\overline{u}\ln\left(u_{cr}\right)}{\sigma_u^2\sqrt{\mu_c}} + \frac{3}{10}\frac{\mu_c\sigma_u^2 B}{u_{cr}^3} + \frac{1}{5}\frac{\mu_c\overline{u}\sigma_u B\sqrt{6}}{u_{cr}^3} \\
&+\frac{1}{16}\frac{u_{cr}\sqrt{6}\ln\left(\sqrt{\mu_c}\overline{u} + \sqrt{\mu_c}\sqrt{6}\sigma_u + B\right)}{\sigma_u\sqrt{\mu_c}} + \frac{1}{30}\frac{\mu_c\overline{u}^3 B\sqrt{6}}{u_{cr}^3\sigma_u} - \frac{1}{16}\frac{u_{cr}\sqrt{6}\ln\left(u_{cr}\right)}{\sigma\sqrt{\mu_c}}
\end{aligned} \tag{B.21}$$

For case 6 in Figure B.1 equation (B.22) is the solution

$$f_3 - f_2\left(\frac{1}{\sqrt{\mu_c}}u_{cr}\right) + f_1\left(-\frac{1}{\sqrt{\mu_c}}u_{cr}\right) \tag{B.22}$$

When these values are substituted (B.23) is obtained

$$\begin{aligned}
&\frac{1}{120}\frac{\mu_c B\overline{u}^4}{u_{cr}^3\sigma_u^2} + \frac{1}{16}\frac{u_{cr}\sqrt{6}\ln\left(\sqrt{\mu_c}\overline{u} + \sqrt{\mu_c}\sqrt{6}\sigma_u + B\right)}{\sigma_u\sqrt{\mu_c}} - \frac{1}{16}\frac{u_{cr}\sqrt{6}\ln\left(u_{cr}\right)}{\sigma_u\sqrt{\mu_c}} - \\
&\frac{3}{80}\frac{\mu^2 B}{tr\sigma^2} + \frac{1}{16}\frac{u_{cr}\overline{u}\ln\left(\sqrt{\mu_c}\overline{u} + \sqrt{\mu_c}\sqrt{6}\,\sigma_u + B\right)}{\sigma_u^2\sqrt{\mu_c}} + \frac{3}{10}\frac{\mu_c A\overline{u}^2}{u_{cr}^3} + \\
&\frac{3}{10}\frac{\mu_c B\overline{u}^2}{u_{cr}^3} - \frac{1}{16}\frac{u_{cr}\overline{u}\ln\left(u_{cr}\right)}{\sigma_u^2\sqrt{\mu_c}} - \frac{9}{40}\frac{A}{u_{cr}} - \frac{1}{30}\frac{trA}{\mu_c\sigma_u^2} + \frac{3}{40}\frac{\overline{u}A\sqrt{6}}{u_{cr}\sigma_u} \\
&-\frac{1}{5}\frac{\sigma_u\mu_c A\overline{u}\sqrt{6}}{u_{cr}^3} - \frac{1}{30}\frac{\mu_c\overline{u}^3 A\sqrt{6}}{u_{cr}^3\sigma_u} + \frac{3}{10}\frac{\mu_c\sigma_u^2 A}{u_{cr}^3} - \frac{1}{30}\frac{u_{cr}B}{\mu_c\sigma_u^2} - \frac{9}{40}\frac{B}{u_{cr}} - \\
&\frac{1}{16}\frac{u_{cr}\sqrt{6}\ln\left(\sqrt{\mu_c}\overline{u} - \sqrt{\mu_c}\sqrt{6}\sigma_u + A\right)}{\sigma_u\sqrt{\mu_c}} + \frac{1}{16}\frac{u_{cr}\overline{u}\ln\left(\sqrt{\mu_c}\overline{u} - \sqrt{\mu_c}\sqrt{6}\sigma_u + A\right)}{\sigma_u^2\sqrt{\mu_c}} - \\
&\frac{3}{80}\frac{\overline{u}^2 A}{u_{cr}\sigma_u^2} + \frac{1}{120}\frac{\mu_c\overline{u}^4 A}{u_{cr}^3\sigma_u^2} + \frac{1}{16}\frac{u_{cr}\sqrt{6}\ln\left(u_{cr}\right)}{\sigma_u\sqrt{\mu_c}} - \frac{1}{16}\frac{u_{cr}\overline{u}\ln\left(u_{cr}\right)}{\sigma_u^2\sqrt{\mu_c}} - \\
&\frac{3}{40}\frac{\overline{u}B\sqrt{6}}{u_{cr}\sigma_u} + \frac{1}{30}\frac{\mu_c\overline{u}^3 B\sqrt{6}}{u_{cr}^3\sigma_u} + \frac{1}{5}\frac{\mu_c\overline{u}\sigma_u B\sqrt{6}}{u_{cr}^3} + \frac{3}{10}\frac{\mu_c\sigma_u^2 B}{u_{cr}^3}
\end{aligned} \tag{B.23}$$

B.2.2 Bed-load transport formulation

$$\sqrt{\mu_c}\cdot u\cdot T\left(u_i\right)\cdot P\left(u_i\right)=\begin{cases}0 & u\le \overline{u}-\sqrt{6}\,\sigma_u\\ \sqrt{\mu_c}\;u\left(\dfrac{\mu_c\cdot u^2-u_{cr}^2}{u_{cr}^2}\right)\left(\dfrac{1}{\sqrt{6}\,\sigma_u}-\dfrac{\overline{u}-u}{6\,\sigma_u^2}\right) & \overline{u}-\sqrt{6}\,\sigma_u<u\le\overline{u}\\ \sqrt{\mu_c}\;u\left(\dfrac{\mu_c\cdot u^2-u_{cr}^2}{u_{cr}^2}\right)\left(\dfrac{1}{\sqrt{6}\,\sigma_u}+\dfrac{\overline{u}-u}{6\,\sigma_u^2}\right) & \overline{u}<u\le\overline{u}+\sqrt{6}\,\sigma_u\\ 0 & u>\overline{u}+\sqrt{6}\,\sigma_u\end{cases} \tag{B.24}$$

Derived with maple v15.0

For $\overline{u}-\sqrt{6}\,\sigma_u<u\le\overline{u}$

$$\begin{aligned}f_1\left(u\right)=&\frac{1}{30}\frac{\mu_c^{1.5}\;u^5}{u_{cr}^2\;\sigma_u^2}-\frac{1}{24}\frac{\mu_c^{1.5}\;u^4\left(\overline{u}+\sqrt{6}\;\sigma_u\right)}{u_{cr}^2\sigma_u^2}-\frac{1}{18}\frac{\sqrt{\mu_c}\;u^3}{\sigma_u^2}+\frac{1}{12}\frac{\sqrt{\mu_c}\;u^2\left(\overline{u}-\sqrt{6}\;\sigma_u\right)}{\sigma_u^2}+\\&+\frac{1}{2}\frac{\mu_c^{1.5}\;\overline{u}^3}{u_{cr}^2}-\frac{1}{2}\frac{\mu_c^{1.5}\;\sigma_u\;\overline{u}^2\;\sqrt{6}}{u_{cr}^2}+\frac{1}{120}\frac{\mu_c^{1.5}\;\overline{u}^5}{u_{cr}^2\;\sigma_u^2}-\frac{1}{24}\frac{\mu_c^{1.5}\;\overline{u}^4\;\sqrt{6}}{u_{cr}^2\;\sigma_u}+\frac{1}{12}\frac{\sqrt{\mu_c}\;\overline{u}^2\;\sqrt{6}}{\sigma_u}-\\&-\frac{1}{36}\frac{\sqrt{\mu_c}\;\overline{u}^3}{\sigma_u^2}+\frac{3}{2}\frac{\mu_c^{1.5}\;\sigma_u^2\;\overline{u}}{u_{cr}^2}-\frac{1}{2}\sqrt{\mu_c}\;\overline{u}-\frac{3}{10}\frac{\mu_c^{1.5}\;\sigma_u^3\;\sqrt{6}}{u_{cr}^2}+\frac{1}{\sqrt{6}}\sqrt{\mu_c}\;\sigma_u\end{aligned} \tag{B.25}$$

For $\overline{u}<u\le\overline{u}+\sqrt{6}\,\sigma_u$

$$\begin{aligned}f_2\left(u\right)=&-\frac{1}{30}\frac{\mu_c^{1.5}\;u^5}{u_{cr}^2\;\sigma_u^2}+\frac{1}{24}\frac{\mu_c^{1.5}\;u^4\left(\overline{u}+\sqrt{6}\;\sigma_u\right)}{u_{cr}^2\sigma_u^2}+\frac{1}{18}\frac{\sqrt{\mu_c}\;u^3}{\sigma_u^2}-\frac{1}{12}\frac{\sqrt{\mu_c}\;u^2\left(\overline{u}+\sqrt{6}\;\sigma_u\right)}{\sigma_u^2}+\\&+\frac{1}{2}\frac{\mu_c^{1.5}\;\overline{u}^3}{u_{cr}^2}-\frac{1}{2}\frac{\mu_c^{1.5}\;\sigma_u\;\overline{u}^2\;\sqrt{6}}{u_{cr}^2}-\frac{1}{120}\frac{\mu_c^{1.5}\;\overline{u}^5}{u_{cr}^2\;\sigma_u^2}-\frac{1}{24}\frac{\mu_c^{1.5}\;\overline{u}^4\;\sqrt{6}}{u_{cr}^2\;\sigma_u}+\frac{1}{12}\frac{\sqrt{\mu_c}\;\overline{u}^2\;\sqrt{6}}{\sigma_u}+\\&+\frac{1}{36}\frac{\sqrt{\mu_c}\;\overline{u}^3}{\sigma_u^2}+\frac{3}{2}\frac{\mu_c^{1.5}\;\sigma_u^2\;\overline{u}}{u_{cr}^2}-\frac{1}{2}\sqrt{\mu_c}\;\overline{u}-\frac{3}{10}\frac{\mu_c^{1.5}\;\sigma_u^3\;\sqrt{6}}{u_{cr}^2}+\frac{1}{\sqrt{6}}\sqrt{\mu_c}\;\sigma_u\end{aligned} \tag{B.26}$$

For $u\ge\overline{u}+\sqrt{6}\,\sigma_u$

$$f_3=\frac{\mu_c^{1.5}\;\overline{u}^3}{u_{cr}^2}+3\;\frac{\mu_c^{1.5}\;\overline{u}\;\sigma_u^2}{u_{cr}^2}-\sqrt{\mu_c}\;\overline{u} \tag{B.27}$$

Case 3

For case 3 the there are no contributions of negative velocities

$$f_3 - f_1\left(\frac{1}{\sqrt{\mu_c}}u_{cr}\right) \tag{B.28}$$

$$\sqrt{\mu_c}\cdot u\cdot T = \frac{1}{2}\frac{\mu_c^{1.5}\ \overline{u}^3}{u_{cr}^2} + \frac{3}{2}\frac{\mu_c^{1.5}\ \sigma_u^2\ \overline{u}^3}{u_{cr}^2} - \sqrt{\mu_c}\ \overline{u} + \frac{1}{45}\frac{u_{cr}^3}{\mu_c\ \sigma_u^2} - \frac{1}{24}\frac{u_{cr}^2\left(\overline{u}-\sqrt{6}\ \sigma_u\right)}{\sqrt{\mu_c}\ \sigma_u^2}$$
$$+\frac{1}{2}\frac{\mu_c^{1.5}\ \sigma_u\ \overline{u}^2\sqrt{6}}{u_{cr}^2} - \frac{1}{120}\frac{\mu_c^{1.5}\ \overline{u}^5}{u_{cr}^2\ \sigma_u^2} + \frac{1}{24}\frac{\mu_c^{1.5}\ \overline{u}^4\ \sqrt{6}}{u_{cr}^2\ \sigma_u} - \frac{1}{12}\frac{\sqrt{\mu_c}\ \overline{u}^2\ \sqrt{6}}{\sigma_u} + \tag{B.29}$$
$$+\frac{1}{36}\frac{\sqrt{\mu_c}\ \overline{u}^3}{\sigma_u^2} + \frac{3}{10}\frac{\mu_c^{1.5}\ \sigma_u^3\sqrt{6}}{u_{cr}^2} - \frac{\sqrt{\mu_c}\ \sigma_u}{\sqrt{6}}$$

Case 4

$$f_3 - f_1\left(\frac{1}{\sqrt{\mu_c}}u_{cr}\right) + f_1\left(-\frac{1}{\sqrt{\mu_c}}u_{cr}\right) \tag{B.30}$$

$$\sqrt{\mu_c}\cdot u\cdot T = \frac{2}{45}\frac{u_{cr}^3}{\mu_c\ \sigma_u^2} + \frac{\mu_c^{1.5}\ \overline{u}^3}{u_{cr}^2} + \frac{3\ \mu_c^{1.5}\ \sigma_u^2\ \overline{u}}{u_{cr}^2} - \sqrt{\mu_c}\ \overline{u} \tag{B.31}$$

Case 5

For case 5 the there are no contributions of negative velocities

$$f_3 - f_2\left(\frac{1}{\sqrt{\mu_c}}u_{cr}\right) \tag{B.32}$$

$$\sqrt{\mu_c}\cdot u\cdot T = \frac{1}{2}\frac{\mu_c^{1.5}\ \overline{u}^3}{u_{cr}^2} + \frac{3}{2}\frac{\mu_c^{1.5}\ \sigma_u^2\ \overline{u}^3}{u_{cr}^2} - \sqrt{\mu_c}\ \overline{u} - \frac{1}{45}\frac{u_{cr}^3}{\mu_c\ \sigma_u^2} +$$
$$+\frac{1}{24}\frac{u_{cr}^2\left(\overline{u}+\sqrt{6}\ \sigma_u\right)}{\sqrt{\mu_c}\ \sigma_u^2} + \frac{1}{2}\frac{\mu_c^{1.5}\ \sigma_u\ \overline{u}^2\sqrt{6}}{u_{cr}^2} + \frac{1}{120}\frac{\mu_c^{1.5}\ \overline{u}^5}{u_{cr}^2\ \sigma_u^2} + \frac{1}{24}\frac{\mu_c^{1.5}\ \overline{u}^4\ \sqrt{6}}{u_{cr}^2\ \sigma_u} - \tag{B.33}$$
$$-\frac{1}{12}\frac{\sqrt{\mu_c}\ \overline{u}^2\ \sqrt{6}}{\sigma_u} - \frac{1}{36}\frac{\sqrt{\mu_c}\ \overline{u}^3}{\sigma_u^2} + \frac{3}{10}\frac{\mu_c^{1.5}\ \sigma_u^3\sqrt{6}}{u_{cr}^2} - \frac{\sqrt{\mu_c}\ \sigma_u}{\sqrt{6}}$$

Case 6

$$f_3 - f_2\left(\frac{1}{\sqrt{\mu_c}}u_{cr}\right) + f_1\left(-\frac{1}{\sqrt{\mu_c}}u_{cr}\right) \tag{B.34}$$

$$\sqrt{\mu_c}\cdot u\cdot T = \frac{\mu_c^{1.5}\ \overline{u}^3}{u_{cr}^2} + \frac{3\ \mu_c^{1.5}\ \sigma_u^2\ \overline{u}}{u_{cr}^2} - \sqrt{\mu_c}\ \overline{u} + \frac{1}{12}\frac{u_{cr}^2\ \overline{u}}{\sqrt{\mu_c}\ \sigma_u^2} + \frac{1}{60}\frac{\mu_c^{1.5}\ \overline{u}^5}{u_{cr}^2\ \sigma_u^2} - \frac{1}{18}\frac{\sqrt{\mu_c}\ \overline{u}^3}{\sigma_u^2} \tag{B.35}$$

B.3 Sensitivity

In this appendix the sensitivity of the Van Rijn 1993 formula and of Van Rijn i.t. are overviewed. For this sensitivity analysis a few approximations have to be made. Delft3D computes the velocity at every layer. When a simplified form is used only 1 velocity is known. Also the turbulent kinetic energy near the bed is not known on forehand. A series of hydrodynamic models have been made to see the influence of the depth averaged velocity on the velocity in the lowest computational layer. And to see the influence of the depth averaged velocity on the turbulent kinetic energy. The relation between the both velocities appeared to be linear and the relation between the velocity and the turbulent kinetic energy was a power function.

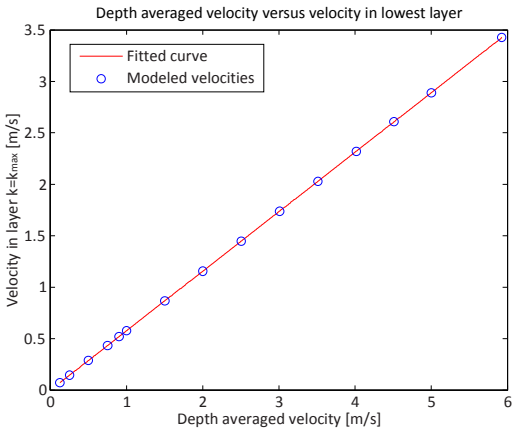

Figure B.2: Depth averaged velocity versus velocity at layer k=k_{max}

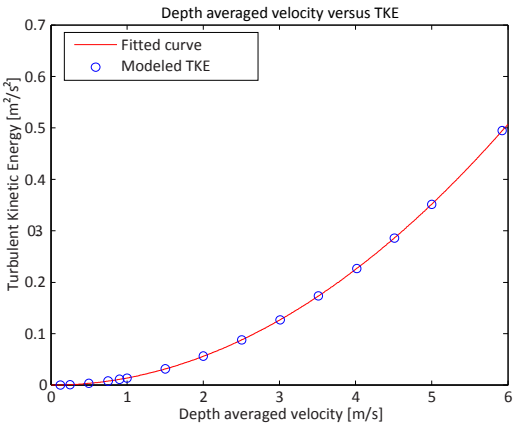

Figure B.3: Depth averaged velocity versus TKE

Variable	Value
D_{50}	140 μm
C	50
Turbulence	$0.01395\ u_{da}^{2.005}$
Near-bed velocity	$u_{bed} = 0.5781\ u_{da}$

The turbulence and near-bed velocity functions are calculated using Delft3D results. Figure B.4 shows the near-bed reference concentration versus the shear stress. Figure B.5 shows the bed load transport versus the shear stress. Van Rijn 1993 computes a higher near-bed reference concentration than Van Rijn i.t.. The bed-load transport gives comparable results for a water level of 5 metres.

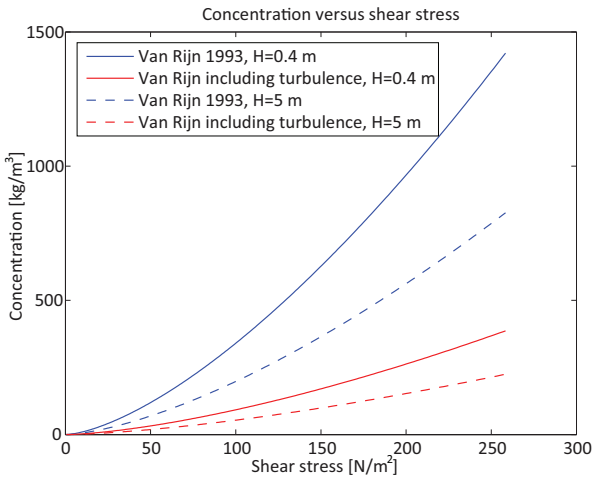

Figure B.4: Near-bed concentration versus shear stress for Van Rijn 1993 and Van Rijn including turbulence

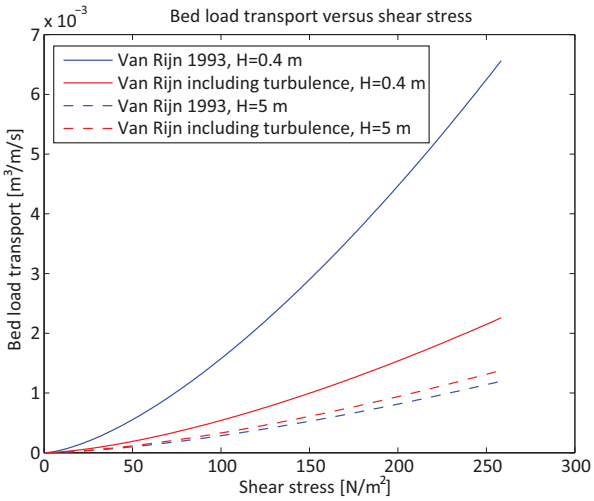

Figure B.5: Bed load transport versus shear stress for Van Rijn 1993 and Van Rijn including turbulence

When the water level increases, the near-bed reference concentration and bed-load transport decreases (see Figure B.6 and Figure B.7), due to the influence of the ripple factor. Van Rijn i.t. shows less dependence on the water height.

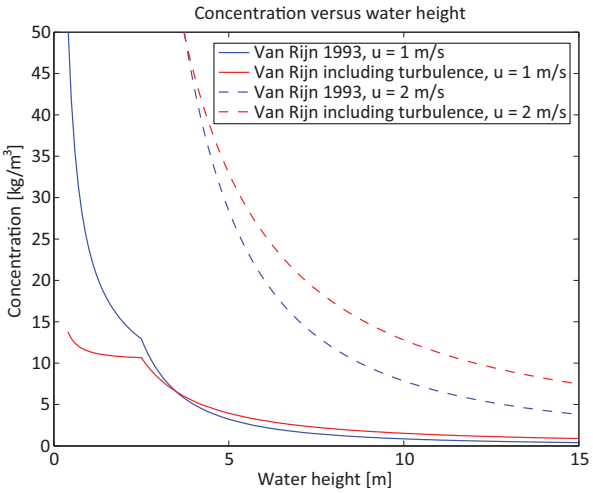

Figure B.6: Near-bed concentration versus water height for Van Rijn 1993 and Van Rijn including turbulence

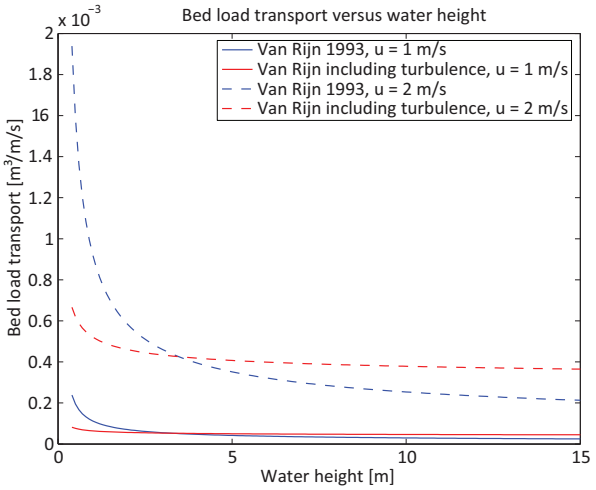

Figure B.7: Bed load transport versus water height for Van Rijn 1993 and Van Rijn including turbulence

Van Rijn i.t. formulation shows less dependence on the roughness level than Van Rijn 1993 (see Figure B.8 and Figure B.9)

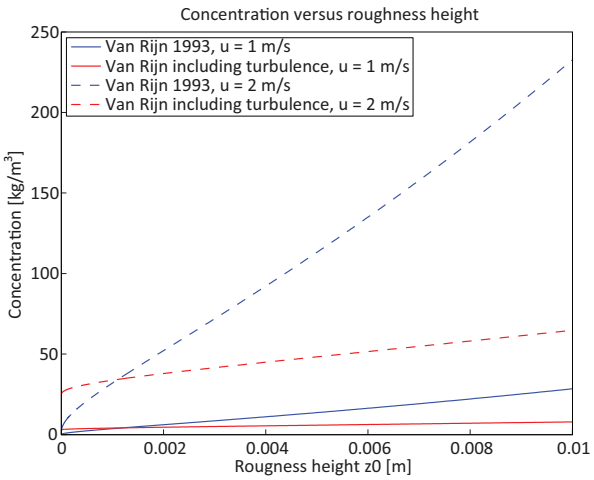

Figure B.8: Near-bed concentration versus roughness height for Van Rijn 1993 and Van Rijn including turbulence

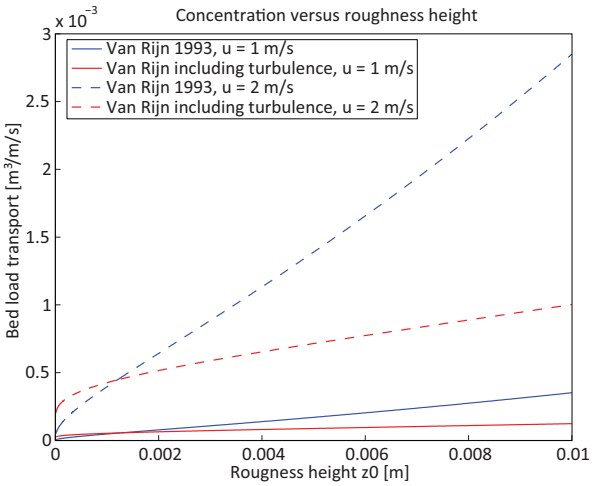

Figure B.9: Bed load transport versus roughness height for Van Rijn 1993 and Van Rijn including turbulence

The general conclusion drawn from this sensitivity analysis is that at small water heights and shear stress the formulations lay close to each other. At higher velocities and water levels Van Rijn 1993 computes a higher concentration and bed-load transport than Van Rijn i.t.. Therefore, for full-scale models another calibration factor is needed. The concentration and transports are then multiplied with a factor of 2.

B.3.1 Difference of triangular distribution and normal distribution

The aim of the triangular distribution was to show similar results as a normal distribution. The both are compared in this section. The relative error between the two is plotted for different velocities and water heights. In most of the situations the relative error is smaller than one tenth, which is a good value. Only at very low shear stresses the relative error for the near-bed reference concentration becomes higher than one tenth. In this situation the standard deviation influences the normal distribution more than the triangular distribution, because the domain of instantaneous velocities described by a triangular distribution is smaller.

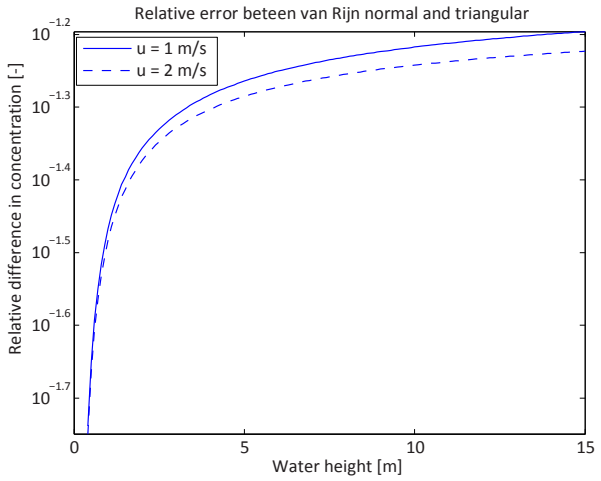

Figure B.10: Relative error between Van Rijn normal and triangular for the near-bed reference concentration at different water heights

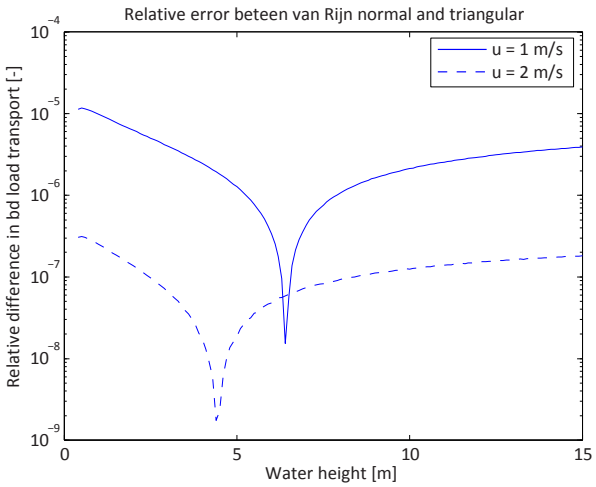

Figure B.11: Relative error between Van Rijn normal and triangular for bed-load transport at different water heights

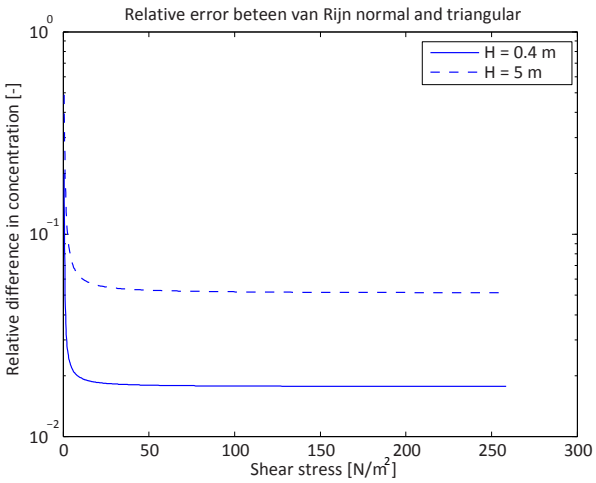

Figure B.12: Relative error between Van Rijn normal and triangular for the near-bed reference concentration at different shear stresses

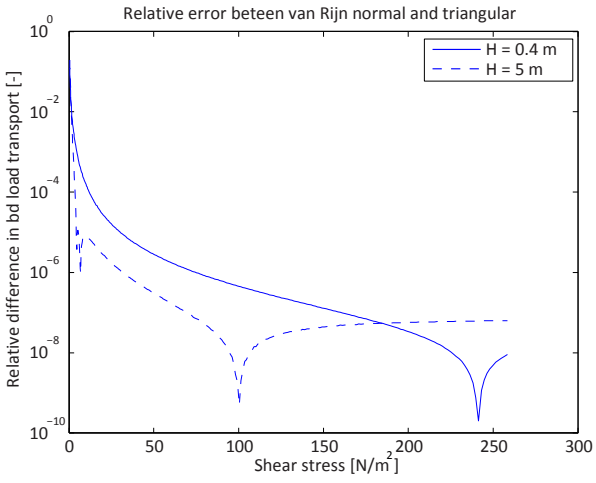

Figure B.13: Relative error between Van Rijn normal and triangular for bed-load transport at different shear stresses

Appendix C Slope slumping

C.1 Plane equation

$$\mathbf{n}_{ab} = \mathbf{a} \times \mathbf{b} = \begin{vmatrix} \mathbf{i} & \mathbf{j} & \mathbf{k} \\ a_1 & a_2 & a_3 \\ b_1 & b_2 & b_3 \end{vmatrix} \tag{C.1}$$

$$\mathbf{n}_{ab} = \left(a_2 b_3 - a_3 b_2\right)\mathbf{i} + \left(a_3 b_1 - a_1 b_3\right)\mathbf{j} + \left(a_1 b_2 - a_2 b_1\right)\mathbf{k} \tag{C.2}$$

The normalize vector is

$$\hat{\mathbf{n}}_{ab} = \frac{\mathbf{n}_{ab}}{\left\|\mathbf{n}_{ab}\right\|} \tag{C.3}$$

The dihedral angle between the plane spanned by $\mathbf{a}$ and $\mathbf{b}$ and a horizontal plane is

$$\cos\varphi = \mathbf{n}_{ab} \cdot \mathbf{n}_0 = \hat{n}_{ab,1} \cdot n_{0,1} + \hat{n}_{ab,2} \cdot n_{0,2} + \hat{n}_{ab,3} \cdot n_{0,3} \tag{C.4}$$

$$\mathbf{n}_0 = \begin{bmatrix} 0 \\ 0 \\ 1 \end{bmatrix} \tag{C.5}$$

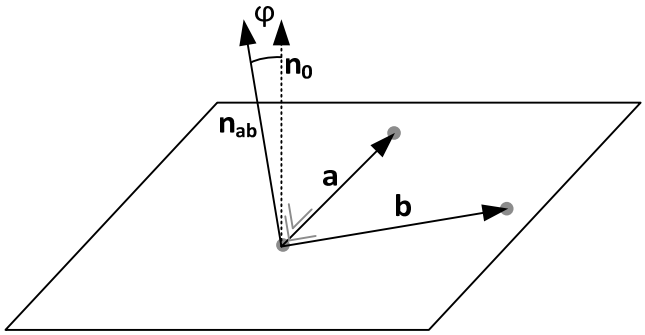

Figure C.1: Angel between a plane and the horizontal

$n_{0,1}$ and $n_{0,2}$ are zero. $n_{0,3}$ is 1 therefore

$$\cos\varphi = \mathbf{n}_{ab} \cdot \mathbf{n}_0 = \hat{n}_{ab,3} = \frac{\left(a_1 b_2 - a_2 b_1\right)}{\sqrt{\left(a_2 b_3 - a_3 b_2\right)^2 + \left(a_3 b_1 - a_1 b_3\right)^2 + \left(a_1 b_2 - a_2 b_1\right)^2}} \tag{C.6}$$

$$\tan(\arccos x) = \frac{\sqrt{1 - x^2}}{x} \tag{C.7}$$

$$h_{1,new} = \frac{-h_2 b_2 a_2 - a_1 h_2 b_1 + h_2 b_2^2 - b_2 h_3 a_2 + h_3 a_1^2 - h_3 a_1 b_1 + h_2 b_1^2 + h_3 a_2^2}{a_2^2 - 2a_2 b_2 + b_2^2 + b_1^2 - 2b_1 a_1 + a_1^2} + \frac{a_1 b_2 - a_2 b_1}{a_2^2 - 2a_2 b_2 + b_2^2 + b_1^2 - 2b_1 a_1 + a_1^2} \cdot \frac{\sqrt{\left(\varphi_{\max}^2 a_1^2 - 2\varphi_{\max}^2 b_1 a_1 + \varphi_{\max}^2 b_2^2 - 2\varphi_{\max}^2 a_2 b_2 + \varphi_{\max}^2 b_1^2 - h_2^2 + 2h_2 h_3 - h_3^2 + \varphi_{\max}^2 a_2^2\right)}}{a_2^2 - 2a_2 b_2 + b_2^2 + b_1^2 - 2b_1 a_1 + a_1^2} \tag{C.8}$$